



**POLITECNICO
DI TORINO**



POLITECNICO DI TORINO

in collaboration with RMIT University, Melbourne

Master's degree course in Aerospace Engineering

Master's degree thesis

Particle swarm-based trajectory
and mission optimisation
for LEO SmartSat applications

Candidate

Enrico Lagona

Supervisors

Roberto Sabatini

Manuela Battipede

Co-Supervisors

Alessandro Gardi

Samuel Hilton

To my family, for everything, forevermore

Alla mia famiglia, per tutto, per sempre

Acknowledgements

First of all, I wish to thank the One who gave me the possibility to conclude this university path and gave me the strength to arrive at this awaited day, even when I thought to give up: my God.

I wish to thank my supervisors, prof. Sabatini and prof. Battipede, because I was given the opportunity to finish my academic journey with an abroad experience, in a study field I'd like it can be at the centre of my future career. I wish to thank Alex Gardi and Sam Hilton for their patience, for their precious suggestions and for helping me during the development of this thesis.

I must thank the shoulders that up to this moment led me here, come with me to the doors of a better future that unfortunately my Sicily rarely gives: my parents. I thank my sister and my brother too because they sustained me in these years of study.

From 12th May 2014, date in which for the first time I took a flight to Turin when I went to try the test to become a student of this university, I knew a lot of people. From south to north I wish to thank my aunties and uncles, my cousins who always believed in me; my lifelong friends in Scordia, with whom I grew up and always will be important to me: Gioele, Ruben, Emanuele and others. I thank Mariapaola, Greta, Ilaria for sustaining me and for being present in these years.

I wish to thank my housemates/friends: Daniel, Dionisio, Salvo, Umberto, Valentina e Adele with whom I shared a lot in these years even if our lives led us to be physically distant.

I thank who had the pleasure to create an emotional bond with me in the first period in Turin, Andrea and Angelo, including me in a bigger reality. I really thank Michela and Angelo again for your friendship and for being a great comfort in the most difficult and worst moments: I wish you can stay among those lifelong friends, whatever the future holds for us.

I thank my university friends, Luca and Chiara, with whom I shared beautiful days but even the post-exam depression moments.

In the end, thanks to all friends of the 9th floor of the Borsellino residence for the beautiful experience to live together and for frying everything had life.

From today the new awaited adventure called “true life” is about to start, in which finally/unfortunately it is needed to grow, roll up the sleeves and put the best foot forward. The future is definitely uncertain and full of unexpected events for everyone, but even if “*Many things about tomorrow I don't seem to understand*” what I can say is that surely “*I know Who holds tomorrow and I know Who holds my hand*” and I believe it is enough.

Ringraziamenti

Voglio prima di tutti ringraziare chi al di sopra di tutti mi ha dato la possibilità di concludere questo percorso universitario, anche quando pensavo di mollare tutto, e che mi ha dato la forza di arrivare a questo tanto atteso giorno: il mio Dio.

Desidero ringraziare il prof. Sabatini e la prof.ssa Battipede per l'opportunità che mi hanno offerto di concludere il mio percorso universitario con un'esperienza all'estero e in un campo di studio che vorrei che un domani fosse al centro del mio percorso lavorativo. Ringrazio anche Alessandro Gardi e Sam Hilton per la loro pazienza, per i preziosi suggerimenti e per avermi assistito durante lo sviluppo di questa tesi.

Ringrazio le spalle che fino a questo momento mi hanno portato qui, accompagnato alle porte di un futuro migliore che purtroppo difficilmente la mia Sicilia riesce a concedere: i miei genitori. Ringrazio anche mia sorella e mio fratello che mi hanno anche loro sostenuto in questi anni di studio.

Dal 12 maggio 2014, data in cui per la prima volta prendevo un volo per Torino, in cui andavo a sostenere il test d'ingresso per diventare uno studente del Politecnico di Torino, ho conosciuto tante persone. Da sud a nord voglio ringraziare zii cugini che hanno creduto in me; gli amici di sempre che sono a Scordia, con i quali sono cresciuto e che sempre avranno un'importanza particolare per me: Gioele, Ruben, Emanuele e altri. Grazie anche a Mariapaola, Greta, Ilaria per avermi sostenuto ed essere state presenti in questi anni.

Ringrazio i coinquilini/amici: Daniel, Dionisio, Salvo e Umberto, Valentina, Adele con i quali abbiamo condiviso tanto in questi anni anche se la vita ci ha portato ad essere fisicamente distanti.

Ringrazio anche chi ha avuto il piacere di creare un legame affettivo e un'amicizia con me nel primo periodo qui a Torino, Andrea e Angelo, includendomi in una più grande realtà alla quale non ero mai stato abituato. Ringrazio in particolar modo Michela e nuovamente Angelo per la vostra amicizia e per essere stati di conforto nei momenti peggiori e difficili: che anche voi possiate rimanere tra quegli amici di sempre, qualsiasi cosa ci riservi il futuro.

Grazie anche agli amici di università, Luca e Chiara, con cui ho condiviso giorni belli ma anche i momenti di depressione post-esame.

Infine, grazie agli amici del 9° piano del Borsellino per la bella esperienza di vivere insieme in residenza e di friggere qualsiasi cosa avesse vita.

Da oggi parte quella nuova avventura attesa da tanto tempo chiamata vera vita, in cui finalmente/purtroppo bisogna crescere, rimboccarsi le maniche e dare il meglio di sé stessi. Il futuro è sicuramente incerto e pieno di imprevisti per tutti, ma anche se *“Nulla so del mio domani”* quello che so e che per certo *“mi terrà per man Gesù”* e credo che ciò sia abbastanza.

Table of contents

List of figures.....	iv
List of tables	vii
List of abbreviations.....	viii
Abstract	1
Introduction.....	3
1 Past and future of space telescopes	9
1.1 Hubble Space Telescope	11
1.2 James Webb Space Telescope	19
1.2.1 Attitude Control System	20
1.2.2 Fine Guidance Control System	21
1.2.3 Science goals of JWST.....	24
2 Artificial Intelligence for space applications	27
2.1 The problem of mission autonomy	28
2.2 Automation, Autonomy, Autonomicity	28
2.3 The necessity of autonomy	29
2.3.1 Distributed spacecraft mission vs. single spacecraft mission	29
2.3.2 Distance, data rate and communication delay	30
2.3.3 Ground support	30
2.4 Artificial Intelligence applied to satellites	30
2.5 Evolutionary algorithms	34
3 Preliminary mission and satellite design	37
3.1 Purpose of the mission	39
3.2 Preliminary mission analysis	40
3.2.1 Space mission elements	41
3.3 V-model and project phasing	42
3.4 Requirements definition.....	43
3.5 Functional architectures.....	45

3.5.1	GNC functional architecture.....	45
3.5.2	ADCS functional architecture.....	47
3.6	Functional architecture of other subsystems	49
3.7	The role of the Ground Control Station.....	52
3.8	Satellite CAD model.....	54
4	Principles of non-linear programming.....	59
4.1	Newton's method.....	60
4.1.1	One variable	60
4.1.2	Multiple variables	61
4.2	Optimal control problem formulation.....	62
4.3	Introduction to pseudo-spectral methods	63
4.4	Mathematical principles of pseudo-spectral methods	64
4.4.1	Discretization	67
4.5	Features of pseudo-spectral methods	69
4.6	Results of Pseudo-spectral methods applied to orbital and attitude problems.....	70
5	Particle Swarm Optimisation	73
5.1	Particle Swarm Optimisation algorithm	73
5.1.1	Basics of PSO	74
5.1.2	PSO algorithm.....	74
6	Mathematical models for optimisation	77
6.1	Orbital manoeuvre optimisation model.....	77
6.1.1	Gravitational disturbing acceleration	83
6.1.2	Aerodynamic drag	84
6.1.3	Thrust acceleration	84
6.1.4	Cost function definition for the orbital manoeuvre	87
6.2	Attitude reorientation optimisation model.....	89
6.2.1	Attitude path based on Bézier curves.....	90
6.2.2	Modified Rodrigues Parameters	90
6.2.3	The time mapping function.....	94
6.2.4	Inverse dynamics	95

6.2.5	Disturbing torques	95
6.2.6	Attitude reorientation geometrical constraints.....	100
6.2.7	Cost function definition for attitude reorientation manoeuvre.....	102
6.3	Collision avoidance analysis	104
6.3.1	Methods and models adopted for collision avoidance.....	104
7	Optimisation results.....	117
7.1	Probability of collision analysis	117
7.2	Trajectory optimisation.....	120
7.2.1	Case 1 analysis.....	121
7.2.2	Case 2 analysis.....	124
7.3	Attitude reorientation optimisation.....	126
8	Conclusion	131
	References.....	135

List of figures

Figure 1. Cluster M44.....	4
Figure 2. Apollo 11 landing on the Moon.....	6
Figure 3. Atmosphere ray absorption	7
Figure 4. Hubble Space Telescope.....	8
Figure 5. Gamma ray bursts captured by NASA's Fermi satellite in green dots. Credits: NASA/DOE/Fermi LAT Collaboration.....	9
Figure 6. Hubble's light path	12
Figure 7. Hubble's instruments observation wavelengths.....	12
Figure 8. Elements of Hubble's Pointing Control System.....	13
Figure 9. Hubble's field of view. In the figure: FGS Fine Guidance Sensor, WFPC Wide Field Planetary Camera, HRS High Resolution Spectrograph, FOS Faint Object Spectrograph, FOC Faint Object Camera, HSP High Speed Photometer	14
Figure 10. Search Mode and Coarse Track Guide Star Acquisition.....	15
Figure 11. Coarse track Nutation Trajectory	16
Figure 12. Fine Lock Acquisition	17
Figure 13. On axis open loop transfer function (left) and close loop transient response (right)	18
Figure 14. Deployed view of James Webb Space Telescope	19
Figure 15. Fine guidance control loop.....	23
Figure 16. Non-exhaustive of EAs and their variants	35
Figure 17. Sequence from CoolSat observations to JWST reorientation	40

Figure 18. V-model.....	42
Figure 19. ESA project phasing.....	43
Figure 20. GNC functional tree.....	46
Figure 21. GNC functional architecture	47
Figure 22. ADCS functional architecture	48
Figure 23. ADCS functional architecture	49
Figure 24. Propulsion system functional architecture	50
Figure 25. COMMSYS functional architecture	50
Figure 26. EPS functional architecture	51
Figure 27. TCS functional architecture	51
Figure 28. OBC functional architecture	52
Figure 29. Payload functional architecture	52
Figure 30. CAD model. Front (a) and back (b) view	55
Figure 31. CAD model. Internal views.....	55
Figure 32. Schematic linkage for multiple-phase optimal control problem .	66
Figure 33. PSO particle position updating scheme	76
Figure 34. Thrust pointing angles.....	84
Figure 35. Umbra and penumbra region	96
Figure 36. Atmospheric density model	99
Figure 37. Velocity vector and flight path angle	100
Figure 38. RSW frame	101
Figure 39. Attitude forbidden zone	101

Figure 40. SEZ and ECI reference frame	108
Figure 41. Frame for spherical coordinates.....	109
Figure 42. Encounter frame at the time of closest approach.....	113
Figure 43. Encounter plane rotation (a) and Frame for the probability of collision calculation (b)	114
Figure 44. Hard Body definition	115
Figure 57. Covariance matrixes. The outer ellipsoid is the cumulative covariance matrix. Scaled graph.....	119
Figure 58. Probability of collision in the conjunction plane.....	120
Figure 45. Control time history for case 1	122
Figure 46. Transfer orbit radius during the manoeuvre for final case	123
Figure 47. Case 1 transfer orbit (scale graph).....	123
Figure 48. Control time history for case 2	124
Figure 49. Case 2 transfer orbit (scale graph).....	125
Figure 50. Transfer orbit radius during the manoeuvre for case 2	125
Figure 51. Quaternion time history	126
Figure 52. Manoeuvre in RSW	127
Figure 53. Angular velocity time history	127
Figure 54. Angular accelerations time histories	128
Figure 55. Torque time history	128
Figure 56. Keep-out functions	129

List of tables

Table 1. Categories of Small Satellites	37
Table 2. Mission requirements	43
Table 3. Functional requirements	44
Table 4. Environmental requirements.....	44
Table 5. Operational requirements	44
Table 6. Interface, physical and design requirements	45
Table 7. Differences between a Ground-dependent satellite and an autonomous satellite.....	53
Table 8. Tank volume determination.....	56
Table 9. Component weights	57
Table 10. Initial and final parameters for optimisation using a PS method	71
Table 11. Control points determination for constraints on angular velocity and acceleration	93
Table 12. Simulation orbital data	117
Table 16. Spacecraft initial data and navigation error	118
Table 17. Radar data	118
Table 13. Trajectory optimisation simulation data	121
Table 14. Case 1. Polynomial coefficients for the control law.....	122
Table 15. Case 2. Polynomial coefficients for the control law.....	124

List of abbreviations

ACS	Advanced Camera for Surveys / Attitude Control System
ADCS	Attitude Determination Control System
AI	Artificial Intelligence
AS	Autonomous Satellite
BCR	Battery Charge Regulator
CAD	Computer Aided Design
CD&H	Command and Data Handling
COMMSYS	COMMunication SYStem
COS	Cosmic Origin Spectrograph
COTS	Commercial-Off-The-Shelf
EA	Evolutionary Algorithm
EM	ElectroMagnetic
EPS	Electrical Power System
ESA	European Space Agency
FGE	Flight Guidance Electronics
FGS	Fine Guidance Sensors
FOV	Field Of View
GA	Genetic Algorithm
GDS	Ground-Dependent Satellite
GNC	Guidance and Navigation Control
GNSS	Global Navigation Satellite System

GPS	Global Positioning System
HST	Hubble Space Telescope
IMU	Inertial Measurement Unit
IR	InfraRed
JWST	James Webb Space Telescope
LEO	Low Earth Orbit
LOS	Line Of Sight
MCC	Mission Control Centre
ML	Machine Learning
MRP	Modified Rodriguez Parameters
NICMOS	Near Camera and Multi-Objective Spectrometer
NIR	Near InfraRed
OBC	On-Board Computer
PCM	Power Conditioning Modules
PCS	Pointing Control System
PL	PayLoad
PS	Pseudo-Spectral
PSO	Particle Swarm Optimisation
RAAN	Right Ascension of the Ascending Node
RW	Reaction Wheel
S/C	SpaceCraft
SRP	Solar Radiation Pressure

STIS	Space Telescope Imaging Spectrograph
TBD	To Be Defined
TCS	Thermal Control System
WFC3	Wide Field Camera 3

Abstract

This thesis is the result of a collaboration between Politecnico di Torino and the Royal Melbourne Institute of Technology. This work aims to develop an automated algorithm to reorient small satellites and change their orbit to avoid debris collisions. In a context where it is essential to reduce costs this concept of a space telescope is presented. This thesis outlines an optimal strategy for trajectory and attitude reorientation for autonomous SmartSats. On-board autonomy allows to reduce the workload on ground-stations and will be mandatory in the next future where satellites will need to accomplish their mission autonomously. This satellite shall be able to optimise its attitude and its trajectory on-board and in real-time. A basic design of the satellite is firstly developed while an optimisation algorithm is used to obtain optimal control solutions for trajectory and attitude. Particle Swarm Optimisation, an evolutionary algorithm reproducing the natural behaviour of swarms, is used to generate a possible solution to control the satellite in the case of continuous low thrust where a polynomial parametrisation is used to model the control time history. For attitude optimisation an inverse dynamic approach is adopted; using polynomial Bézier curves to achieve a possible solution, PSO is used to meet the constraints and then to find the time history for control and angular velocities. Disturbance torques due to solar radiation pressure and atmospheric drag are considered in reorientation optimisation. Lastly, the calculation of a probability of collision is presented to move the satellite avoiding the collision with orbital debris in LEO orbits.

Introduction

“We find them smaller and fainter, in constantly increasing numbers, and we know that we are reaching into space, farther and farther, until, with the faintest nebulae that can be detected with the greatest telescopes, we arrive at the frontier of the known universe.”

Edwin Powell Hubble

Since ancient time, the human being has been interested in looking at the sky. Most of the ancient people thousands of years ago were capable to find answers observing the universe: suffice to think about Egyptians that around 1000 BC recorded the position of the Sun using a large astrolabe, or the position of pyramids carefully aligned to the Polar star. Of course, astronomy played a fundamental religious role in Egyptian culture, but it demonstrates the interest of mankind in space observation. Aristotle in the 4th century BC made the first hypothesis about the movement of planets in space as a perfect circle or Ptolemy coming up with the geocentric theory. Several centuries later these ideas were recognised to be wrong, but their contributions helped to the development of astronomy. In the 15th and 16th century Copernicus revolutionised how people looked at the universe with the Heliocentric theory, which considers no longer the Earth at the centre of the planetary motion but the Sun; furthermore, the apparent annual motion of the Sun is caused by the Earth motion and the diurnal rotation of the stellar sky is explained by the Earth rotation on its axis. The German astronomer Johannes Kepler used Brahe’s observations to establish the motion of planets along elliptical orbits around the Sun, deriving the first three laws of planetary motion [1]:

1. The orbit of each planet is an ellipse, with the Sun at the focus.
2. The line joining the planet to the Sun sweeps out equal areas in equal times.
3. The square of the period of a planet is proportional to the cube of its mean distance from the Sun.

These theories were confirmed by Galileo thanks to his observations with the telescope of Jupiter's moons and the phases of Venus. It was in 1700 when the first rigorous proof of the Earth's motion around the Sun came over with James Bradley who discovered the aberration of light from stars, a small displacement due to the Earth motion and the finite velocity of light [2].



Figure 1. Cluster M44

First telescopes were invented in 1600. As mentioned before, the Italian Galileo Galilei was one of the first astronomers to use a telescope: he saw four bright moons of Jupiter, the phases of Venus, mountains on the Moon and the rings of Saturn. He found the Milky Way composed of faint stars and he found the “nebula” *Praesepe*, today known as M44, to be a cluster of stars.

The first reflecting telescope was constructed by Isaac Newton in 1668 to overcome the chromatic aberration.

It was evident from Kepler's laws of planetary motion that some forces are generated from the Sun and act on the other planets. The English Isaac

Newton provided a theoretical framework to understand this force in the form of universally valid mechanical principle:

Two massive bodies attract each other with a force F proportional to the product of their masses divided by the square of their distance r

$$F = G \frac{m_1 m_2}{r^2}$$

This has been recognised as Newton's law of gravitation, which stays at the basis of the two-body problem. From this theoretical background several famous mathematicians developed celestial mechanics.

Ancients had assumed that stars were fixed at a unique distance on a sphere. The heliocentric system brought up doubts in this belief until Newton's mechanics led to fix the stars in a celestial sphere. It is now assumed that stars are distributed throughout the space in a vast range of distances. A proof of this was given by new and variable stars and of proper motion of stars by Edmond Halley in 1718. Besides stars, star clusters and "nebulae" are found in the sky and are summarized under the name of Deep Sky Objects. In the second half of the 19th century new technological developments led to significant changes in astronomy and in the new upcoming astrophysics.

- **Stellar photometry** introduced by Karl Friedrich Zöllner with the visual photometer. Improvements had been achieved with photoelectric cells and by the measure of photographic plates.
- **Spectroscopy.** Joseph Fraunhofer was the first to record a good spectrum of the Sun and discovered black lines in it. David Brewster showed that cold gases produce dark absorption lines in continuous spectra. Gustav Robert Kirchhoff and Robert Bunsen discovered that

each chemical element has a characteristic spectrum of lines: thus, the chemical composition of a light source can be determined from spectral analyses

- **Astronomical photography**
- **Improvements in the larger telescopes**

All this brief story of astronomy demonstrates the interest of the human being in space. In the latter 20th century rockets were developed, powerful enough to overcome the force of gravity to reach orbital velocities opening the way to space. WW2 pushed the research in this field developing new rockets for military purposes. After the war, USA and Soviet Union created their own missile programs.

In October 1957 the Soviets launched the first artificial satellite in space [3], Sputnik 1, while 4 years later Juri Gagarin became the first human being to reach the space, orbiting Earth in Vostok 1. In 1958 US launched the first satellite, Explorer 1, and Alan Shepard was the first American to fly into space in 1961.

“That's one small step for a man, one giant leap for mankind.”

These were the words of Neil Armstrong when he put his feet on the Moon soil for the first time in the story of humanity. Several missions came in quick



Figure 2. Apollo 11 landing on the Moon

succession to space, including science missions but improvements of services too. From the first launch to space it was immediately clear the immense potential that space possesses.

But human curiosity never ends. This has led to discover more and more about the universe in which we have been living.

All the information we acquire from the cosmos arrives to us in the shape of a wave, visible or not [4]. The faint rays from the most distant galaxies take thousands, million or billion years to reach us. The basic concepts of radiation are at the basis of the modern astronomy.

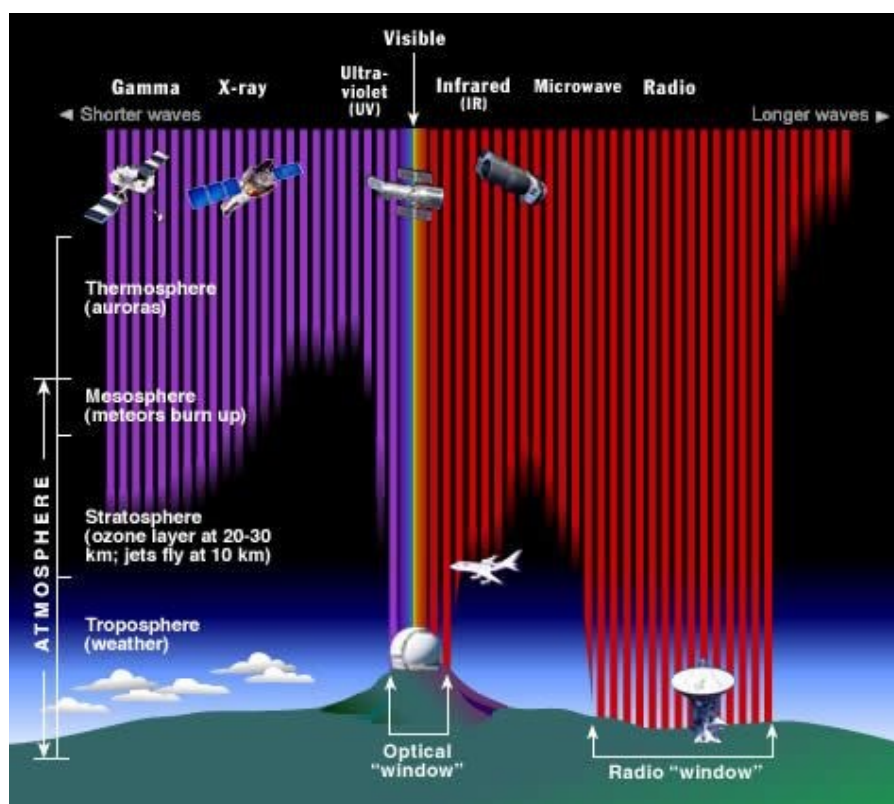


Figure 3. Atmosphere ray absorption

Radiation is how energy is transmitted through space from a point to another one. All the rays contain information about the source which they come from. Modern telescopes capture those rays to extrapolates data to better understand the universe. Of course, Earth is the easiest place where a space observatory can be built but disadvantages are present from this point of

view. Earth is a planet that has an atmosphere permitting the development of life on its surface, shielding dangerous rays through its gaseous layers. This represents a limit in what can be observed from the Earth's surface and what the reality is.

From 1965 space telescopes have been launched to collect radiations deriving from space objects or universe, capturing the radiations from microwaves to gamma rays.



Figure 4. Hubble Space Telescope

Of course, worth to be mentioned is Hubble which has given us the most spectacular images of the universe today we have got. It is a definite that space explorations are high-priced and they do not return any direct income. For this reason, every science mission is directly commissioned by governments and rarely by private companies.

But what if we used a SmallSat as a space telescope? This is the question at the basis of this thesis. Along the work, a preliminary concept of a SmallSat space telescope is developed. A small satellite in a low orbit could help other bigger telescopes to reorient their attitude and to point towards the most interesting point in the universe allowing to save precious resources. Moreover, they could help ground telescope to look at specific portions of sky determined from the space.

1

Past and future of space telescopes

Space telescopes, or astronomical space observatories, are usually grouped by frequency range they can record gamma rays, x-rays, ultraviolet, visible, infrared, microwaves, radio waves. An astronomical observatory does usually work in multiple frequencies and could be able to collect particles, such as nuclei and/or electrons.

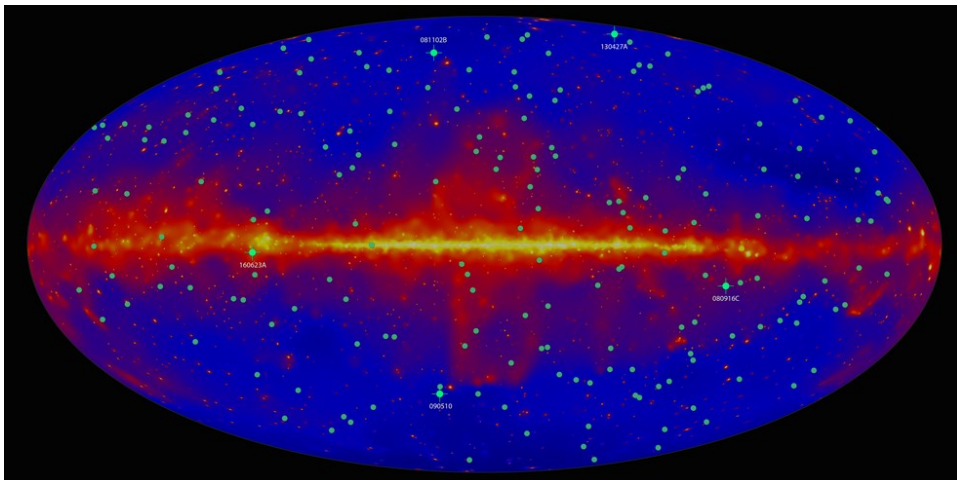


Figure 5. Gamma ray bursts captured by NASA's Fermi satellite in green dots. Credits: NASA/DOE/Fermi LAT Collaboration

Because of the atmosphere absorption not every wave can be captured from the ground, so it is mandatory having a telescope outside the terrestrial atmosphere to collect data from gamma or x rays. Gamma rays are usually the product of supernovae, neutron stars, pulsars, black holes. Gamma-ray bursts release

more energy in 10 s than the Sun will emit in its lifetime; they have been detected but their source is not still identified. Solving the mystery of their origin scientists hope to gain further knowledge about the universe itself and its expansion rate [5]. Gamma-ray space telescope still operating are INTEGRAL (International Gamma-Ray Astrophysics Laboratory) of ESA launched in 2002, Swift Gamma-ray Burst Explorer or Fermi Gamma-ray Space Telescope from NASA, in addition to other telescopes from JAXA or other space agencies.

X-rays telescopes measure high-energy photons. Astrophysical objects emitting this radiation are galaxies, clusters, stars, white dwarfs, neutron stars or black holes. Ultraviolet radiation is emitted from the Sun galaxies and stars in general.

The visible-light astronomy represents the oldest form of astronomy. The advantage of positioning a telescope in space instead on the ground is to delete distortion caused by the atmosphere, providing higher resolution images. One of the most famous telescopes used in visible light is the Hubble Space Telescope which has given us magnificent images of our universe.

Infrared light is energy lower than visible light, emitted by sources cooler or moving away from the observer. The main objects that can be seen in the infrared are cool stars, nebulae, and redshifted galaxies.

The last kind of telescopes is represented by those capable to reveal gravitational waves, which are disturbances in the curvatures of the spacetime and are generated by accelerated masses. The first gravitational waves were recorded by LISA pathfinder.

In the last decade, Hubble played a pivotal role in space exploration. Thanks to its images today we know more than we could have without it. Its successor is designed to be the James Webb Space Telescope, scheduled to be launched in March 2021. Above will be presented their characteristics.

1.1 Hubble Space Telescope

As mentioned before, astronomical observation from the ground are affected by atmospheric turbulence and distortion with the outcome of degraded images [6]. From the beginning of the space programmes great advantages were found in exploring the universe outside the atmosphere. The first missions operated in different bands obtaining productive results that pushed NASA and ESA to launch a new space telescope. In 1990 Hubble Space Telescope was launched. Orbiting at 540 km above the surface of the Earth, HST has a clear field of view free from detrimental effects caused by the atmosphere. The telescope can detect not only the visible light, but also ultraviolet bands absorbed by the atmosphere. Hubble is a Cassegrain reflector: the light travels into a tube collected by a bowl-like and inwardly curved by a primary mirror and reflected toward a smaller secondary mirror where the light is focused on the focal plane and analysed by various instruments [7].

Hubble is currently equipped with the Wide Field Camera 3 (WFC3), Cosmic Origin Spectrograph (COS), Advanced Camera for Surveys (ACS), Space Telescope Imaging Spectrograph (STIS) and Fine Guidance Sensors (FGS).

WFC3 gives the access to ultraviolet, visible, and infrared wavelength of light.

COS is used to analyse the UV radiation in detail.

ACS helps to map the distribution of the dark matter and detects the most distant objects in the universe.

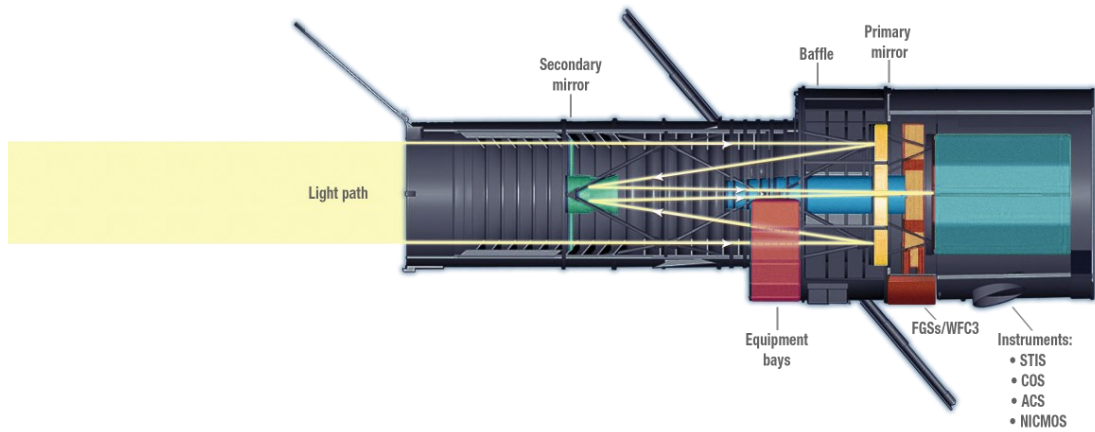


Figure 6. Hubble's light path

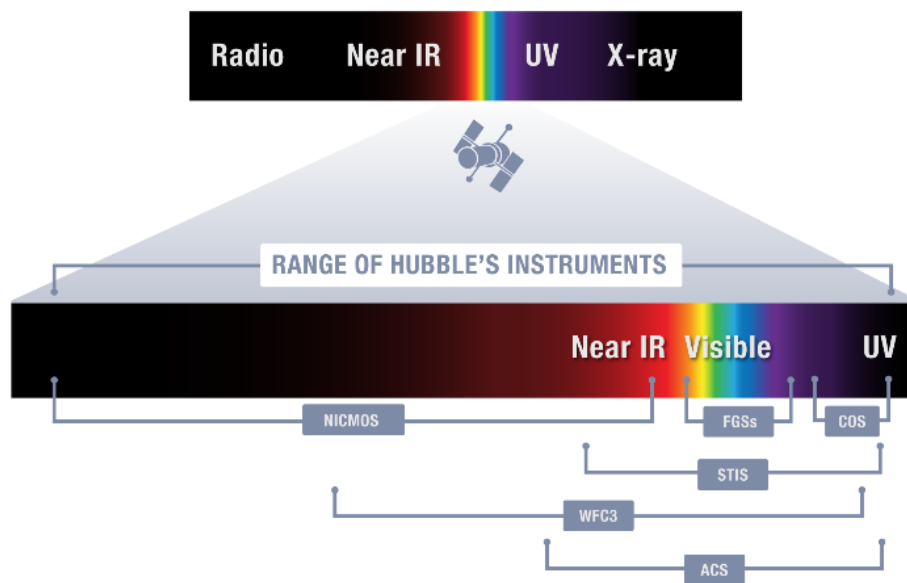


Figure 7. Hubble's instruments observation wavelengths

NIR Camera and Multi-Objective Spectrometer (NICMOS) detected infrared light to reveal objects in the interstellar dust. No longer operating.

FGS are devices that lock onto the guide stars keeping Hubble pointed in the area of interest. Two out of three sensors point at an astronomical target and then hold that target in the instrument's field of view while the third sensor is used to measure the distance between stars and their relative motions.

Hubble's Pointing Control System is the fundamental equipment that allows to obtain clear images devoid of jitter [8]. Both sensors and Actuators are used to gather information about the attitude from the Sun, the stars and Earth's magnetic field, rotating the telescope to point in a specific direction.

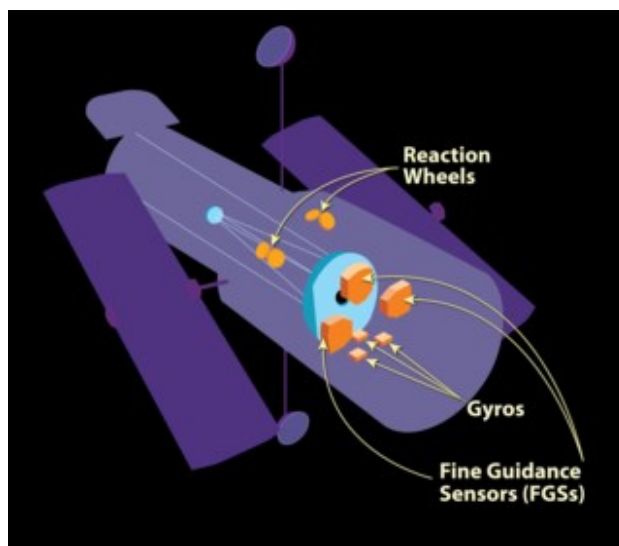


Figure 8. Elements of Hubble's Pointing Control System

There are five sensors which compose the PCS: Coarse Sun Sensors, the Magnetic Sensing System, the gyroscopes, the Fixed Head Star Trackers, and the Fine Guidance Sensors.

The Coarse Sun Sensors determine the Hubble's attitude with respect to the Sun. Silicon diode detectors determine if the Sun is present in their field of view and in that case the angle of the Sun relative to the sensor; the magnetic

sensing system measures the telescope's orientation in relation to the magnetic field of the Earth; the gyroscopes the direction and the rate of the rotation; the Fixed Star Trackers determine Hubble's attitude measuring the location and the intensity brightness of stars in the field of view, matching them with the map present on the on-board computer, increasing the accuracy of the attitude. The Fine Guidance System comprises three Fine Guidance Sensors (FGSs) that use starlight to lock the attitude.

Two actuators systems are basically used: Reaction Wheels and magnetic torquers.

Guidance Control is achieved looking into a dominant guide star with one FGS and then looking on the non- dominant guide star with a second FGS [9].

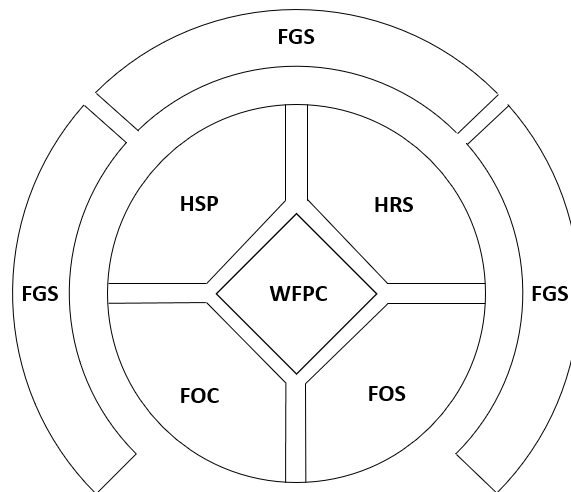


Figure 9. Hubble's field of view. In the figure: FGS Fine Guidance Sensor, WFPC Wide Field Planetary Camera, HRS High Resolution Spectrograph, FOS Faint Object Spectrograph, FOC Faint Object Camera, HSP High Speed Photometer

During the Search Mode of a guide star the IFOV of the FGS is moved in an outward spiral with the centre of the spiral at the best estimate of guide star

location, monitoring the intensity at each clock interval; if the value stays between low and high thresholds (which are set by uplinks), the star is in the IFOV and after that the system enters the coarse track mode. The thresholds help distinguish other stars near the guide star: each guide star in the catalogue has its own thresholds, so this helps to discriminate a specific guide star in the search mode.

Two of three FGS look at a dominant guide to control pitch and yaw while one of them looks at a non- dominant guide star to control roll in the telescope. The Pointing Control System (PCS) orients the telescope such that the line of sight is coincident with the desired SI aperture. A periodic feedback to the PSC maintains a continuous locking of the telescope. The *Coarse Track Mode* provides guidance in about 70% of all science observations, especially under adverse dynamic conditions that occur during day-to-night and night-to-day orbital transitions.

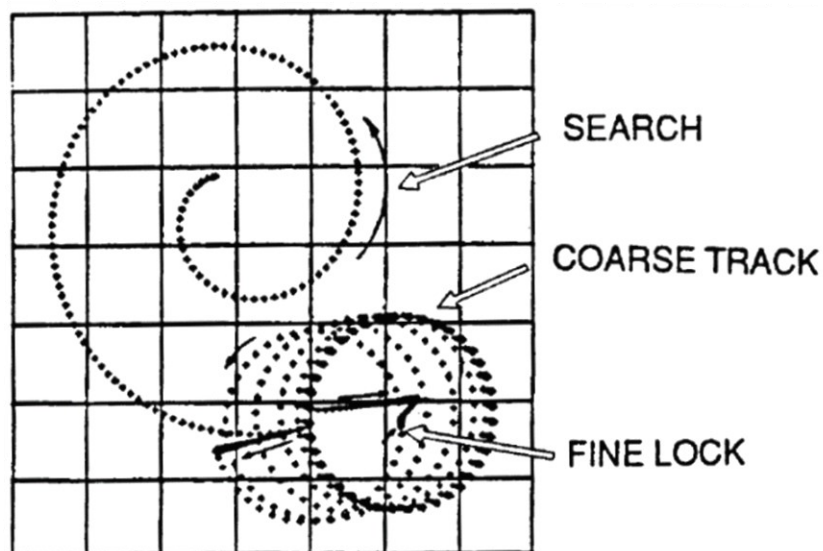


Figure 10. Search Mode and Coarse Track Guide Star Acquisition

The Flight Guidance Electronics (FGE) controls the initial guide-star acquisition following the coarse positioning of the telescope by the PCS hardware. The acquisition is accomplished during a Spiral Search Mode which creates a spiral search pattern in the proximity of the guide star, then the FGE accomplishes guide star detection. At this point, a control mode transition occurs which establishes the Coarse Track Mode. The Search Mode to Coarse Track Mode transition is illustrated in the figure.

The Coarse Track Algorithm measures the photon energy in four quadrants as the star image is nutated in a circular pattern in and out of the square field stops of FGS PMT sensors. The servos move the IFOV in a circle around the spot where the guide star has been detected. At every 40 Hz sample following the end of the first revolution, these 40 intensity values are used to calculate the errors along X and Y. In general, they are not null and are used for feedback corrections to the centre of the nutation circle: it shall shift until the centre of the nutation correspond to the guide star.

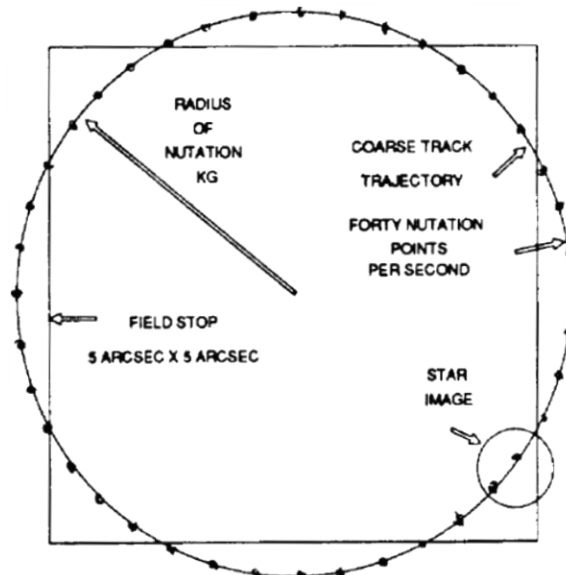


Figure 11. Coarse track Nutation Trajectory

The nutation pattern consists of 40 discrete points on the nutation circle. The pattern is created once per second by commanding the two FGS star Selector Servos to slew the image from point to point. Photon energy is integrated during each 25 milliseconds servo slew resulting in a PMT count “I” which is the sum of the four individual PMT values.

These measurements are used in the signal control equations to adjust the FGS pointing angle toward the line of sight of the star.

The basis for generating the Coarse Track error is the prediction of the displacement of the nutation centre from ideal and the adaptation of the centre position to attempt to null the pointing error.

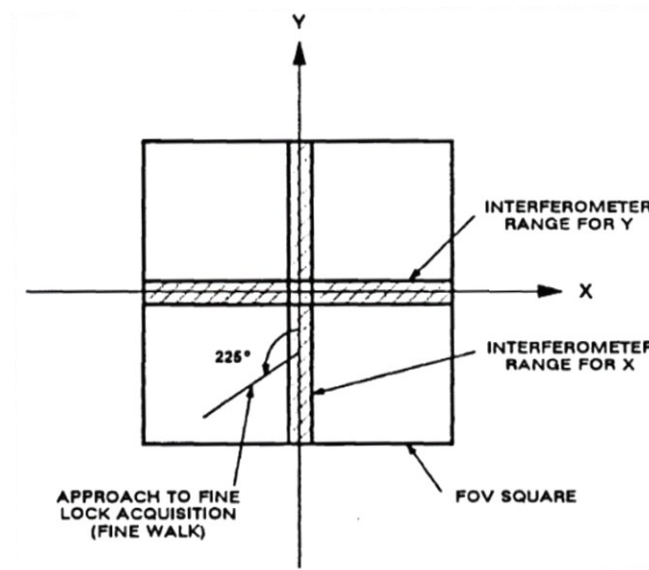


Figure 12. Fine Lock Acquisition

At the end of the coarse tracks the centre of the FGS IFOV diagonally to cross the expected position of the X and Y interferometric null axes.

When the interferometric error signal exceeds a threshold value the fine lock feedback loop is closed nulling the error signal.

Two uplink parameters are programmable. KG is radius of nutation and KJ is closed-loop gain.

In the figure on the right, it can be seen that high values of KG maintain an error saturated closer to the null region and offer higher gain in the null transition region. Choosing large values of KG large disturbances are corrected faster. KJ controls the closed-loop servo gain and transient response. In the following figure, KJ effect is monitored for a selected value of KG. Increasing the value of KJ more than 0.05 arcseconds there are instabilities that must be avoided. The value of KJ must be chosen to provide a damped response.

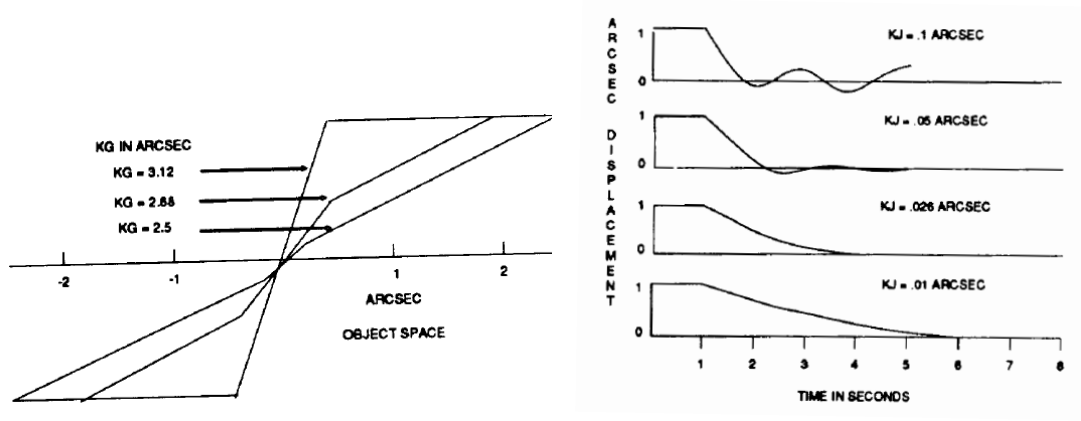


Figure 13. On axis open loop transfer function (left) and close loop transient response (right)

1.2 James Webb Space Telescope

The James Webb Space Telescope has been ideated as the scientific successor of Hubble Space Telescope and Spitzer Space Telescope. Its science goals are motivated by Hubble's results, with the purpose to go beyond what Hubble has already seen [10]. To do so an infrared camera is required, and it is in band that JWST will work. Because of its

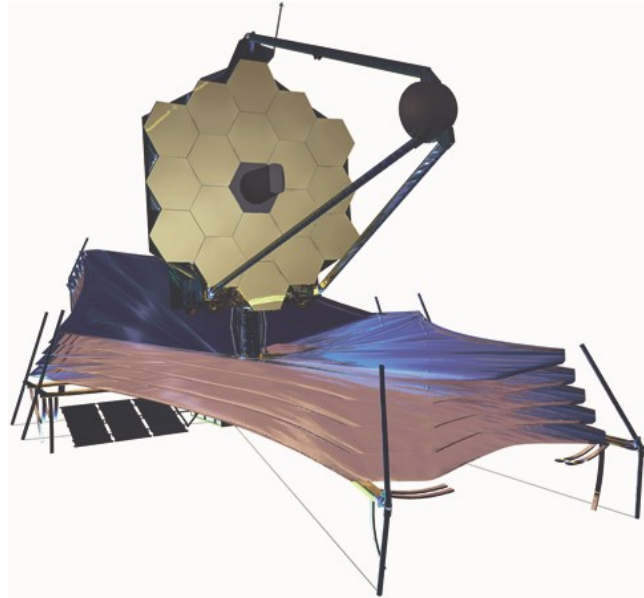


Figure 14. Deployed view of James Webb Space Telescope

mirror, bigger than the Hubble and Spitzer ones to probe beyond their limits, it cannot be launched with the available launch vehicles unless the mirror is folded, which has led to an innovative primary mirror that shall be aligned on-orbit. JWST must operate at 35 K : this temperature requires an orbit far from Earth and a large sun shield. It will be positioned in L2 point of the Earth-Sun system.

The JWST will look back in time to the first galaxies and stars formed billion years ago thanks to the IR instruments of which it is equipped. Two of the instruments, NIRCам and FGS/TF have facility roles.

NIRSpec provides a choice of two spectral resolution in multi-object mode to study the assembly of galaxies, but also a mode to measure galaxy masses.

MIRI, which requires a temperature lower than 7K, will require more cooling than that achieved with the passive radiator system. MIRI shall detect planets thanks to a focal plane mask and a phase mask.

FGS/TF shall track objects of interest imaging a guide star. A centroid is measured, and an error signal is generated and fed to the fine steering mirror. The spacecraft's body pointing is updated as needed to keep the mirror within its range of travel.

To control and checking the spacecraft's attitude gyros and star trackers are used as sensors and reaction wheels as actuators. The roll performance will be provided by the spacecraft Attitude Control system. This kind of scientific observations requires a milliarcsecond pointing accuracy achieved by the Fine Guidance Controller which includes the Fine Guidance Sensor instrument (FGS), the ACS, and the Fine Steering Mirror (FSM). The JWST Pointing Control System (PCS) includes three integrated control systems:

- a three-axis, low bandwidth (0.02Hz) inertial referenced spacecraft attitude control system (ACS) for coarse attitude control
- a two-axis, high-bandwidth (2Hz) telescope line-of-sight (LOS) stabilization control system using a Fast Steering Mirror (FSM)
- a two-axis, very low bandwidth (0.004Hz) FSM off-loading control system.

1.2.1 Attitude Control System

The JWST ACS is based on star trackers and IRUs for attitude determination and RWAs for control with a compensator with a PID logic for ACS, filtering a second-order bending trying to reduce flexible modes, a momentum control loop for reaction wheel control and an IRU (4Hz bandwidth) for body rate

information. Information about attitude and rates are maintained on-board as quaternions integrating IRU's data at every minor cycle (0.064 s). In addition, a Kalman filter corrects the IRU drifts and the SBC attitude quaternion by using star trackers which refer to a star catalogue.

Six RWs in a pyramid configuration provides balanced momentum storage capability in each of the three spacecraft axes. The compensator is implemented with a PI logic, a first-order low-pass filter, a tachometer, and a tachometer-averaging filter for each wheel. The reaction wheels are speed biased to 2700rpm by using an additional bias control loop that regulates reaction wheel speed operation near a fixed speed in the null space of the RW cluster. This RW speed bias set point is needed to maintain RW speeds within an acceptable speed range of 15 Hz to 75 Hz to avoid structural excitations that may contribute to LOS jitter. The momentum and bias control loop bandwidths are set to 0.2 Hz and 0.008 Hz, respectively.

1.2.2 Fine Guidance Control System

The Fine Guidance Control system (FGCS) bandwidth removes ACS jitter with a 2Hz bandwidth and utilizes guide star information processed to track the desired targets in the FOV using the FSM. The Fine Guidance Loop is implemented with a PID logic, a second-order bending filter to improve sensor noise rejection, and FSM provides corrections to the LOS, and a dedicated FGS. The FGS acquires and locks to the desired guide star (GS) stabilizing the FOV for science observations. Because of one guide star used for control by FGS, the FGSC cannot control the roll axis but only pitch and yaw.

The FGS has two separate detector channels, for redundancy and great accuracy, to provide pointing error signals on selected guide star to the ACS for the fine pointing. FGS provides source positions of the guide stars along

with quality indicators (centroids) every 64 ms, to an accuracy of 4 milliarcseconds.

The FGS returns an error signal to the ACS during the guide star tracking. Through a recognition algorithm, the guider reads the detector in stripes to identify the guide star comparing the information in the catalogue with information deriving from the detector.

After the identification, the FGS uses a 128x128 pixel window to acquire the guide star, which is centred on the position provided by the identification. After that, the guide star is acquired in a smaller window with dimensions 32x32 pixels. For each phase, a centroid position of the guide star is given, including the position in x and y, the intensity in counts/s on a 3x3 pixels window and quality indicators which marks centroids if the criteria are not met.

The FGS guider in the guiding mode tracks the guide star in a 32x32 pixel window and provides a centroid every 64 ms to the ACS with the accurate position of the guide star in x, y, its intensity, and quality indicators. When the first valid centroid is identified the Fine Guidance loop is engaged in a closed loop where the Guider provided centroids will be reacted upon by the ACS moving the FSM, which in turn will be reflected in a position change on the guide star centroid provided by the guider. During this tracking mode, the FGS guider keeps track of each centroid and determines if the 32x32 pixel detector window needs to be moved to keep the guide star in the centre of the tracking window. These are configurable parameters, but the default will move the detector track window if 16 centroids in a row indicate that the guide star has moved more than 2 pixels from the centre of the track window. The ACS in parallel is using the centroids provided by the guider 16 times

every second to determine if a command to move the Fine Steering Mirror is needed and if so by how much. Eventually, the ACS movement of the FSM will be such that the guider does not need to move the track window anymore as any movement is compensated by the ACS command to the FSM. At this point in normal operations, the guider will be commanded to its fine guidance mode where an 8x8 detector window is read that provides the higher signal to noise needed for accurate pointing for science observations. When the guider is in this fine guide mode it does not move the detector window anymore but relies solely on the ACS closed-loop commanding of the FSM based on the guide star centroids provided every 64 ms to keep the guide star in the centre of that 8x8 fine guidance window.

The Fine Guidance system remains in track mode for special operations: for science observations of objects in the solar system where the target moves across the guider field of view in an established pattern and the guider moves the tracking window accordingly; the other is in the early stages of the Observatory commissioning where the mirrors are not yet aligned and the image of the guide stars are aberrated and a 32x32 detector window size is needed to capture it.

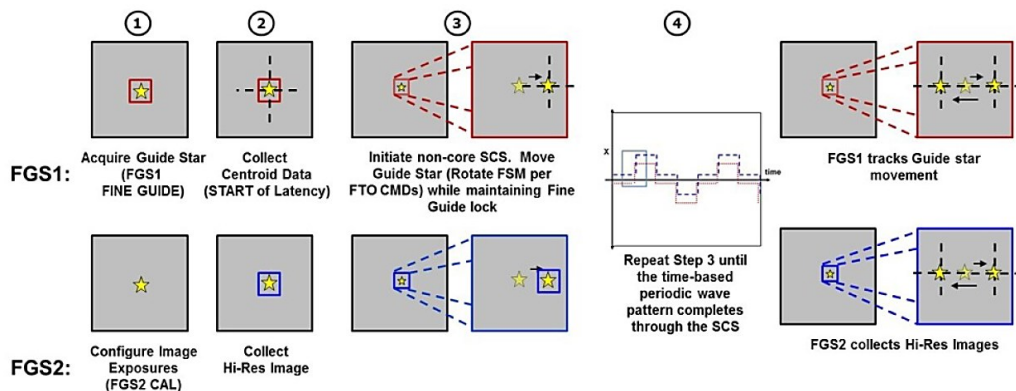


Figure 15. Fine guidance control loop

1.2.3 Science goals of JWST

The main aim of JWST is to examine every phase of the story of the universe, in search of understanding the formation of galaxies, stars, planets and our solar system [11].

First light and reionization

When the universe started cooling protons and neutrons began to combine forming ionized hydrogen and helium. Once formed these atoms attracted electrons becoming neutral. From this point, they travelled freely making the universe no longer opaque this is the end of the dark age. Webb will try to give answers about the formation of the first stars.

From the moment in which the first light left its source, its wavelength shifted towards the red. This phenomenon has been explained by Einstein's General Relativity: the expansion of the universe extends the distances among objects; not only the space but also any light in that space stretches, shifting to longer wavelengths. The expansion of the universe makes us receive infrared light.

JWST will make a near-infrared survey measuring with low-resolution spectroscopy and mid-infrared photometry the universe.

Assembly of galaxies

Galaxies show the matter of the universe and how it is organised in a large scale. Scientists study how this order has changed during the cosmic time to understand the story of the universe. One open question is how the first galaxies formed.

JWST will observe the galaxies back in time trying to answer to this question. Comparing data to the galaxies of these days could be possible to understand their evolution.

Birth of stars and protoplanetary systems

Most of the images captured by Hubble hide a lot of information. Hubble is capable to catch over the visible wavelength but capturing few stars more. JWST is optimised to work in IR wavelength, capturing much more information than Hubble did.

Planets

One of the main studies of JWST is the atmospheres of exoplanets. Being an IR telescope, it will analyse looking at the light passing from the atmosphere. Collaborating with a ground-based telescope will be possible to do spectroscopy of the planet's atmosphere, finding out the chemical composition.

2

Artificial Intelligence for space applications

The influence of Artificial Intelligence (AI) has been becoming more and more essential in new technologies. If before it was a specialised sector of computer science, nowadays it matured in industrial products. Machine Learning (ML) techniques produced new vigorous techniques capable to reach the attention of scientists, inducing new transformation in the whole economics. The space sector has met these new advancements incorporating the concepts related to AI, automated reasoning, robotics in published works. The interests in those applications have been found in preliminary spacecraft design, guidance, and control algorithms to predict the dynamics of perturbed motion or to classify astronomical objects. Many times AI technology was capable to produce impressive results for a determined task; however, their outcome is poor if transmitted to different tasks and when the performance in terms of strength and weakness is not well understood. Autonomous satellites allow reducing the burden on ground station operations. Nowadays, orbit determination strongly depends on ground stations and navigation constellations. Autonomous orbit determination reduces the maintenance cost of those systems and strengthens the possibility to continue the mission in case of emergency.

2.1 The problem of mission autonomy

The development of technology and experience in the space sector has shown the will, desire, and need for more elaborated missions. New scientific targets often require coordinated satellites for multiple observations or for monitoring events without a ground station participation. This increasing demand for spacecraft has led to enhance the software development for space missions on ground and on-board to integrate into the flight control software. During the last years, security standards for human exploration mission have increased [12], becoming a new key driver for improving the spacecraft capabilities for remote or more complex missions. If for a certain kind of missions the human intervention is mandatory (e.g. ISS maintenance), on the other hand, human missions are not advised or prohibited for riskier missions (e.g. mission to asteroids); additionally, astronauts would face numerous problems like long timelines, long distances, the harmful radiation environment. This highlights the necessity of unmanned missions.

2.2 Automation, Autonomy, Autonomicity

The title of this sub-paragraph expresses three important concepts used in space engineering, referring to actions where there are no human interventions in the whole process.

- *Automated* process is a step-by-step routine that replaces the human manual work; it may still require human intervention. An example of this is the extraction and analysis of telemetry data, outputting proper alerts and anomalies. Automatic processes do not execute decision-making operations on real-time events, but human intervention is needed for the analysis results.

- *Autonomy* is an operation aimed to imitate human thought [13]. Examples are coverage calculation or orbit determination on the ground or on-board software monitoring images to decide if more time is needed in a determined area.
- *Autonomic* process concern the sector of self-awareness and self-management. Four characteristics concerning self-management are self-configuring, self-healing, self-optimising, self-protecting; these are related to the self-aware property (capability and state of managed components), self-situated property (knowledge of the system of the surrounding environment), self-monitor property (capability to monitor sensors, actuators and control loops).

2.3 The necessity of autonomy

The wide potentialities of small satellites could enable the diffusion of this category of satellite for several innovative missions. However, mission and system level issues are disrupting the efficiency of small satellites for complex missions.

2.3.1 Distributed spacecraft mission vs. single spacecraft mission

The implementation of a constellation for certain kinds of targets apport several advantages: the chances of fulfilling the mission are preserved in case of system failures, multiple observation can be performed, the payload can be distributed reducing the complexity, replacement is possible by launching new satellites extending the swarm or the constellation. Currently planned missions require several assets in the space segment: this could provoke high costs if superfluous operators-to-satellite relationships are not avoided. Increasing the autonomy level the system sizes can be reduced because the target is reached through the synergy of the satellite in the constellation.

2.3.2 Distance, data rate and communication delay

In some missions, the communication between the GS and the spacecraft could require minutes. If the mission goal is to catch appearing events, the human decision could be too long, increasing the communication delay. In this situation, autonomy enables the possibility of real-time decision-making to observe the targeted phenomena. In addition, large communication latencies would introduce long delays, producing high uncertainties in position and augmenting the probability of mission failure; moreover, the ground operator would take decisions with data not in real-time.

2.3.3 Ground support

Some missions could not have constant support from ground stations (e.g. educational satellites or low-budget projects), producing poor performances. Autonomy would allow the mission to continue, determining the best approach to acquire and downlink data. However not every mission is suitable for a high level of autonomy: in this case, depending on the conditions, adjustable autonomy can be implemented, even if the ground segment should be well-designed to manage the satellite.

2.4 Artificial Intelligence applied to satellites

AI is a branch of computer science that gained popularity in the last decade. Its definitions were evolved quickly and nowadays this field is open to different points of view. Its evolution has been always present in algorithms considered related to this field and it has been used in several applications like autonomous scheduling and planning for space missions, fault detection, isolation and recovery, game playing, logistic planning, machine translation, medical research, robotic vehicles, robotics, spam fighting and speech recognition [14]. Since AI is used to manage different situations, several

approaches could be used to deal with different problems. The usage of certain algorithms is related to the computational power available: for instance, power-intensive algorithms on the ground must be modified to be operational for the space segment.

Regarding the space segment, different works focusing on different methods for autonomous orbit determination are available in the literature. White et al. [15] use a line-of-sight (LOS) measurements of stars to estimate satellite attitude and orbit. Straub and Christian [16] determined orbits through Earth observations of coastlines. Other works focus on ground objects or regular shaped ground landmarks.

The approach proposed in the last years is to provide more intelligent computing on space platforms to augment spacecraft reliability and to coordinate and manage single or multiple satellites autonomously. CubeSats or more in general small satellites have seen growing their importance in autonomous operations. If in the past there were seen as a manner to propose new teaching tools and early technology demonstration, nowadays they have been used even for defence and science applications. A survey [17] published in 2016 described CubeSats excelling at simple tasks or in short missions but, however, they cannot completely substitute more complex platforms. Anyway, CubeSats are capable to maintain a low-cost approach to develop swarms or constellations for multi-point measurements and spatial and temporal coverage: with their strict constraints, these space platforms can achieve challenging defence and science targets. Future semi-autonomous constellations would be able to detect hazards, mapping hazards or forecasting them. However, it is essential to make technological developments to actuate those distributed spacecraft missions. In this scenario, AI has a

significant interest in space computing. The idea to apply AI in the space sector is not novel, but it has been proposed for several years. Giromonte of the European Space Agency (ESA) [18] examines the areas of applications of AI in the space sector. Since AI is a vast theme, we consider those relevant categories for space applications: autonomy, communications, analysis.

Autonomy in the space sector is extensively studied and focuses on navigation, coordination, planning, scheduling, and reliability. Autonomy is what mission designers wish for their mission plans for different reasons. One of them is the delay time between the ground station operators and satellites. In deep-space scenarios where the delay time is not negligible, the spacecraft is aimed to be capable to autonomously make decisions. Other than that, autonomous systems enhance spacecraft reliability for their capacity to autonomously face unexpected situations driving the space platform to safety through autonomous decision-making. Notorious examples of this are the Mars rovers: *Spirit* was provided with software for terrain assessment to recognise hazards based on imagery, *Opportunity* and *Curiosity* could autonomously collect data to select the most high-value science goals. As said before, deep-space explorations need autonomy because of the possible lack of communication for long periods and the consequent possibility to promptly react to the unknown. Moreover, intelligence can help to coordinate large swarms of satellites or constellations with a reduced burden on ground operations. Intelligence embedded in satellites can support data analysis through on-board selection data. This could be particularly useful for observation tasks that include hazard detection such as floods or to monitor confined areas or for weather forecasting.

AI applied to the space sector has to face the computing challenge of small spacecraft computers. Moreover, because of the space environment and hazards related to it like radiation, small space platforms cannot afford radiation-hardened (rad-hard) computers because they are expensive and outdated in performance. Commercial devices can be chosen even if sensitive to radiation effects. These limitations are arduous to ML development.

In the 1980s the idea that intelligence could emerge from interactions between the environment and systems parts came up giving birth to the concept of distributed AI, discipline studying systems composed by multiple agents that can achieve a target operating like a community rather than as an individual. In the aerospace field, it developed as swarm intelligence and distributed computing. Swarm intelligence can be defined as a property of systems made by multiple agents characterised by limited sensing capabilities. The attractive features of swarming intelligence have been used in the space sector where stringent constraints are usually imposed. Space agents' mobility is limited due to limited power and propellant, but also communication and size; however, the great level of adaptability and autonomy is required to have more chances to succeed. The first commercial realised application for satellite systems was a satellite constellation in geosynchronous orbit providing communication services, provided by Arthur C. Clarke. Swarm intelligence methods would represent a valid option for autonomous design operations. Swarm intelligence would provide the possibility to improve the relative satellite motion control. The information exchanged amongst the satellite in the constellation can influence the satellite action selection. The second example of distributed AI is the distributing computing, used in specific applications of the space sector, in particular, to design trajectories. Distributed AI allows us to share the

memory and computing resources. The main limitation is that the problem must be divisible into packages to be solved to allow the division. The main purpose of DAI is the possibility to analyse a large amount of data, specifically for commercial satellites orbiting in LEO orbits. Those satellites continuously orbit the Earth exchanging unprocessed data with the ground stations. Analysis of these data on orbit allows minor data storage. Another example is the solution to global optimisation problems in a distributed way. This approach is surely more elaborate because it introduces the dependency between the computations.

2.5 Evolutionary algorithms

Evolutionary algorithms (EAs) are a class of metaheuristic algorithms suited to solve global optimisation problems inspired by natural phenomena. Metaheuristic can be defined as *“a common but unfortunate name for any stochastic optimization algorithm intended to be the last resort before giving up and using random or brute-force search. Such algorithms are used for problems where you don’t know how to find a good solution, but if shown a candidate solution, you can give it a grade”* [19]. The inspiration of these algorithms due to biological phenomena like insect swarming, ant behaviour has led the application of these techniques to the aerospace field with a high degree of success. At least four categories belong to EA:

- Genetic Algorithms (GA) use a population for searching the optimal solution (or near-optimal) meeting with mutation, cross-over and selection of population. GAs have been proven to be capable to solve interplanetary trajectory optimisation problems.
- Evolutionary Strategies (ES) are algorithms that reach the optimal solution by mutation and selection of operators [20]. The operator

selection is made only on fitness ranking and not on the actual fitness values.

- Evolutionary programming (EP) is a common EA [21] in which some numerical parameters are defined and subjected to evolution.
- Genetic Programming (GP) copes with the solution as a computer program, represented in memory with a tree structure. At each node of the tree, a mathematical expression is executed.

Another popular method is constituted by the Particle Swarm Optimisation (PSO) that inspired by natural swarms found in nature is capable to find near-optimal solutions with good accuracy. It is easy to implement and generally fast to converge. The number of algorithms in the EA field is enormous, including several algorithms and even more variations.

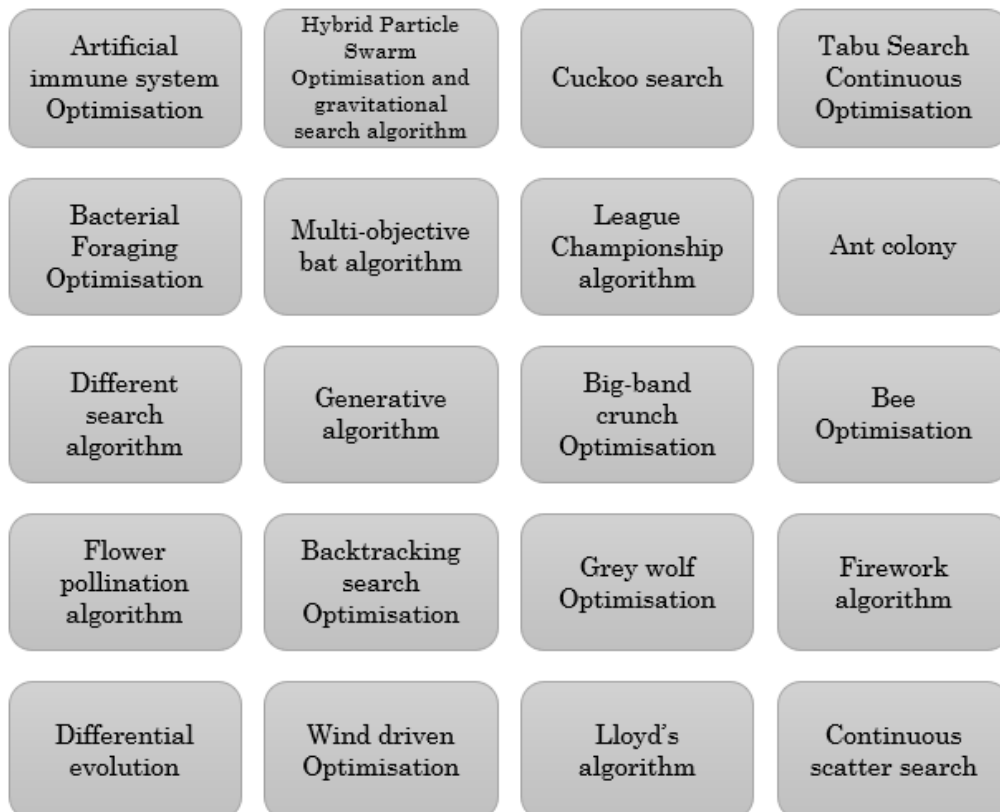


Figure 16. Non-exhaustive of EAs and their variants

3

Preliminary mission and satellite design

“Small satellites” is a not standardised term to define a category of space systems. It is related to those satellites having a limited dimension and weight less than 100 kilograms.

Space agency	Classification	Mass [kg]
European Space Agency (ESA) [22]	Small	350-700
	Mini	80-350
	Micro	50-80
Airbus Defence and Space [22]	miniXL	1000-1300
	Mini	400-700
	Micro	100-200
National Aeronautics and Space Administration (NASA) [23]	Minisatellite	100-180
	Microsatellite	100-100
	Nanosatellite (CubeSat)	1-10
	Femto and Picosatellite	<1
Widely accepted [24]	SmallSat	500-1000
	MiniSat	100-500
	MicroSat	10-100
	NanoSat	1-10
	PicoSat	0.1-1
	FemtoSat	<0.1

Table 1. Categories of Small Satellites

The designed satellite aims to open the door to new frontiers of space exploration. Technological progress has been making new reliable and light-weight components that have led to new concepts and ideas for space applications. A dramatic reduction in weight and volume allowed to compact satellites launching in orbit smaller satellites with a low production and management cost. In this field CubeSats have been becoming a new must thank their standardised concept and commercial-off-the-shelf (COTS) components that can be easily found and included in every project. These new small satellites can provide opportunities to explore space for small countries, educational institutions, and commercial organizations with a relatively modest budget. An individual failure of a small satellite has a much lower impact on the mission itself compared to huger sophisticated satellites, representing, for this reason, a plus for their choice [25].

Based on the experience of the previous space telescopes (e.g. Hubble, JWST), CoolSat, the name given to this satellite, shall be able to look at the sky and taking images with its 4M pixels infrared actively cooled camera with a lower cost compared to other larger space telescopes. CoolSat shall be an autonomous satellite and it will not require, if not in a small part, any ground-based operation but autonomously it shall control its attitude, its trajectory maximizing the field-of-view (FOV). A constellation will be placed in a sun-synchronous LEO orbit at 600 km of altitude: this to reduce the atmospheric drag and the orbit decay and to maintain a correct attitude during the operational phase.

This research will be articulated as follow. A CAD model of the satellite is conceived including the main sensors which will help in attitude and orbit determination and a representative thermal control system (TCS). The CAD

model is not the actual satellite, because approximations in position and shape and components dimensions have been done, however, its main purpose is to provide a model to work on and data that could not be obtained in other ways. The Matlab optimisation code is the core of this work, used to model the attitude and the trajectory optimising the given objectives. In the end, a case for collision avoidance is analysed.

3.1 Purpose of the mission

A space mission conceived for scientific goals usually adopts satellites equipped with multi-purpose instruments capable to manage more tasks with the same payload. This phenomenon is due to limited funds and, like in every satellite brought to space, the mass and volume that inevitably affects the launch cost. CoolSat would not be able to conduct autonomously the mission as a single satellite but it would require to be part of a swarm or a constellation: its characteristic would not allow reaching the requested accurate results because of its payload; even if it is equipped with cutting-edge IR camera for space observations, it may be required to inspect the same phenomenon in other bands of the EM spectrum, not possible with the current payload. The envisioned solution is about a collaboration between larger space telescopes and/or with ground telescopes. An example of this collaboration can be between a constellation and the future JWST or HST to help them in reorientation and in identifying new areas of study. Thanks to its dimensions, CoolSat can perform quicker responses in attitude reorientations, allowing the opportunity to observe more targets in a reduced time. CoolSat would identify or track a portion of the sky in which a phenomenon is thought to be; after some observations, the MCC could command an action to point to a new target.

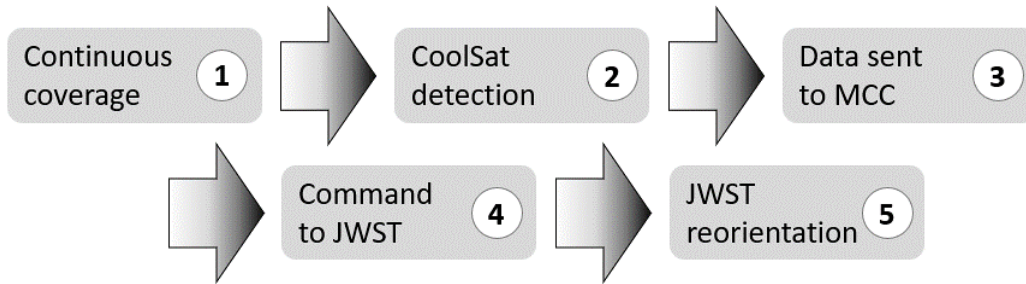


Figure 17. Sequence from CoolSat observations to JWST reorientation

In the previous figure, it is illustrated how JWST could be reoriented using multiple satellites, to give an example of how the mission shall work. A constellation of satellites would provide a continuous coverage (1) of the sky or some pre-identified targets; after some observations, CoolSat detects the required information (2) sending communication and data to the GS (3); the MCC will decide if the acquired observation is useful or not and, in a positive case it will command a further action to JWST (4); JWST will acquire the information performing a reorientation to the new target.

Similarly, this mechanism can be applied to a ground telescope. Because of the atmosphere absorption, not always images captured from the ground are clear; even for the most modern telescope can be difficult to clearly identify areas needed to be looked at. CoolSat could support ground observations providing exact information about the position of the desired phenomenon to improve ground observations.

3.2 Preliminary mission analysis

The following analysis focuses on a set of objectives that need to be fulfilled. The goal of this thesis is to provide an optimisation code to change the current trajectory to avoid a collision and an optimisation code for attitude reorientation. These two main targets are part of a mission that would be able

to provide a service (information on position, intensity, and importance of space phenomena) to other space telescopes or ground telescopes.

3.2.1 Space mission elements

A space mission is composed of distinct phases and elements. Among the elements, it is possible to individuate a space segment, which is the satellite in orbit, a launch segment, the vehicle transporting the spacecraft to the orbit, a ground segment, including the ground control stations and the mission control centre. The previous elements interact as a whole to provide a mission. To have an interaction they need to be designed according to the mission requirements. The totality of the previous elements forms the mission architecture based on which each element is analysed and sized.

The *launch segment* combines the launch facility, the launch vehicle and the stage hosting the spacecraft.

The *orbit* is the spacecraft path. It is usually the assembly of different paths comprising the ascending trajectory, the mission trajectory and the re-entry or disposal trajectory.

The *communication architecture* allows the communication, command and control of the spacecraft.

The *ground system* is the composition of stable and mobile ground station that ensure the service.

Mission operations are the instructions that operators elaborate between space and ground segments.

3.3 V-model and project phasing

Mission development is shown by the graphical illustration that the V-model represents.

From the left side to the right side, the V-model shows the initialisation and decomposition of requirements and formulation of system design with a top-down direction. The basis represents the actual production and the right side with a bottom-up direction shows the integration of different parts, their integration and validation.

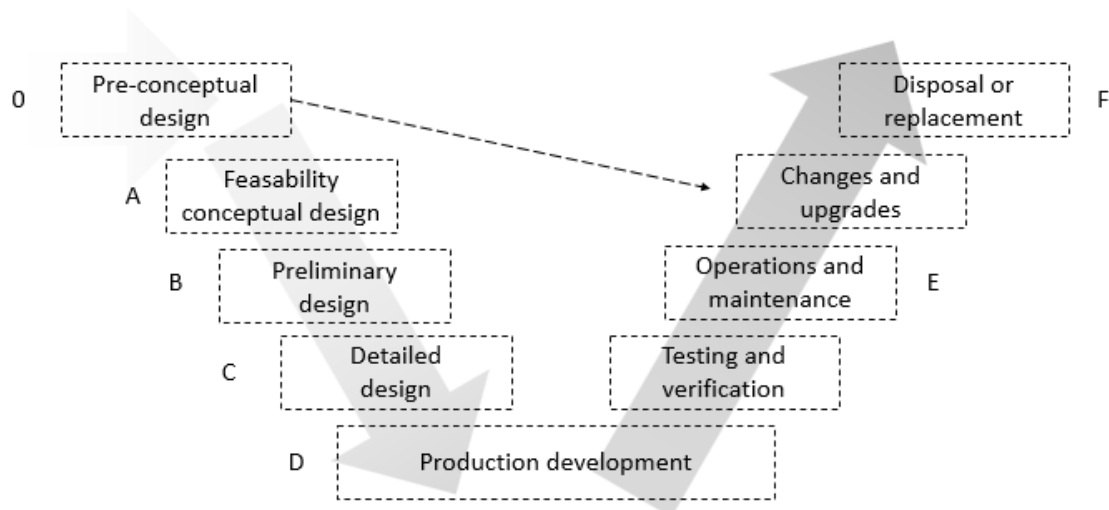


Figure 18. V-model

The project phasing represents the development of a mission based on the V-model. Different organisations use different project phasing. A phase can be depicted as a series of activities advancing the project amongst its milestones, usually ended by a formal review attesting the end of the work according to the requirements.

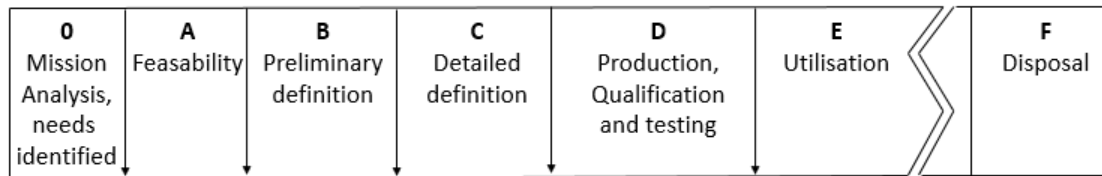


Figure 19. ESA project phasing

3.4 Requirements definition

Mission objectives define the mission requirements and constraints answering to the questions *Why? When? Where? What? How? For how long?* These requirements usually focus on orbit requirements, mission duration, utilisation time, scientific targets defining the success criteria.

	REQUIREMENT
MIS-01	The mission lifetime shall be at least 24 months.
MIS-02	The mission shall have (TBD) S/Cs in TBD orbital planes
MIS-03	Satellites shall be deployed in LEO orbit
MIS-04	Satellites shall be plane in a sun-synchronous orbit
MIS-05	The constellation shall provide coverage of defined targets
MIS-06	S/Cs shall be replaceable
MIS-07	S/Cs shall be compliant with the space debris mitigation guideline
MIS-08	A disposal strategy shall be formulated
MIS-09	Deorbiting shall be accomplished by 25 years after the end of the mission

Table 2. Mission requirements

From the functional analysis a class of requirements, called *functional requirements*, institutes the function the product shall produce and the goodness to perform the mission.

	REQUIREMENT
FUN-01	The constellation shall point all the identified targets
FUN-02	The constellation shall provide inter-satellite communication
FUN-03	The constellation shall provide a downlink communication
FUN-04	The constellation shall provide an uplink communication
FUN-05	MCC shall operate the constellation
FUN-06	The constellation shall perform an automated collision avoidance
FUN-07	The constellation shall perform an automated attitude reorientation

Table 3. Functional requirements

Environmental requirements are determined by environmental conditions, including vibrations during the launch, thermal and radiation environment.

	REQUIREMENT
ENV-01	The constellation shall deal with LEO radiation environment
ENV-02	The S/C shall maintain the camera at the operational temperature

Table 4. Environmental requirements

Operational requirements define the system operability. They involve operative mode implementation from the ground, operations accomplished on-orbit and communications.

	REQUIREMENT
OPS-01	The satellite shall be deployed in sunlight or eclipse
OPS-02	The space segment shall ensure complete coverage of the identified areas
OPS-03	The GS shall ensure the coverage with at least one satellite in the constellation

Table 5. Operational requirements

Other requirements are the *Interface requirements* that define the satellite interfaces with the mission elements; *Physical requirements* determine physical compatibility, applying to the geometry, mass, materials; *Design requirements* are connected to standards, components, safety margins.

	REQUIREMENT
INT-01	The satellite shall tolerate thermal loads at launch
INT-02	The satellite shall share telemetry data with the GS
INT-03	The satellite and launcher shall have different vibrational responses
PHY-01	The satellite shall be between 8U and 16U category
DES-01	The S/C shall incorporate COTS components

Table 6. Interface, physical and design requirements

3.5 Functional architectures

The *functional architecture* can be defined as logical architecture defining what the system is required to do, providing a decomposition of the systems' top-level functions. The decomposition can usually be achieved through a functional tree to identify different levels of decompositions. The functional tree for GNC and ACDS will be presented. The functional hierarchy can be read from top to down where the lower level responds to the question *How?* asked from the higher level, or in a bottom-up direction where the higher level responds to the question *Why?* asked by the lower level.

3.5.1 GNC functional architecture

Standing on the purpose of the mission and the design of this kind of satellite, the main aim GNC system is to provide autonomous guidance and control to the satellite to avoid collision with the debris orbiting in LEO orbits. The

following scheme in the next figure represents the functional tree for the GNC system to avoid the collision.

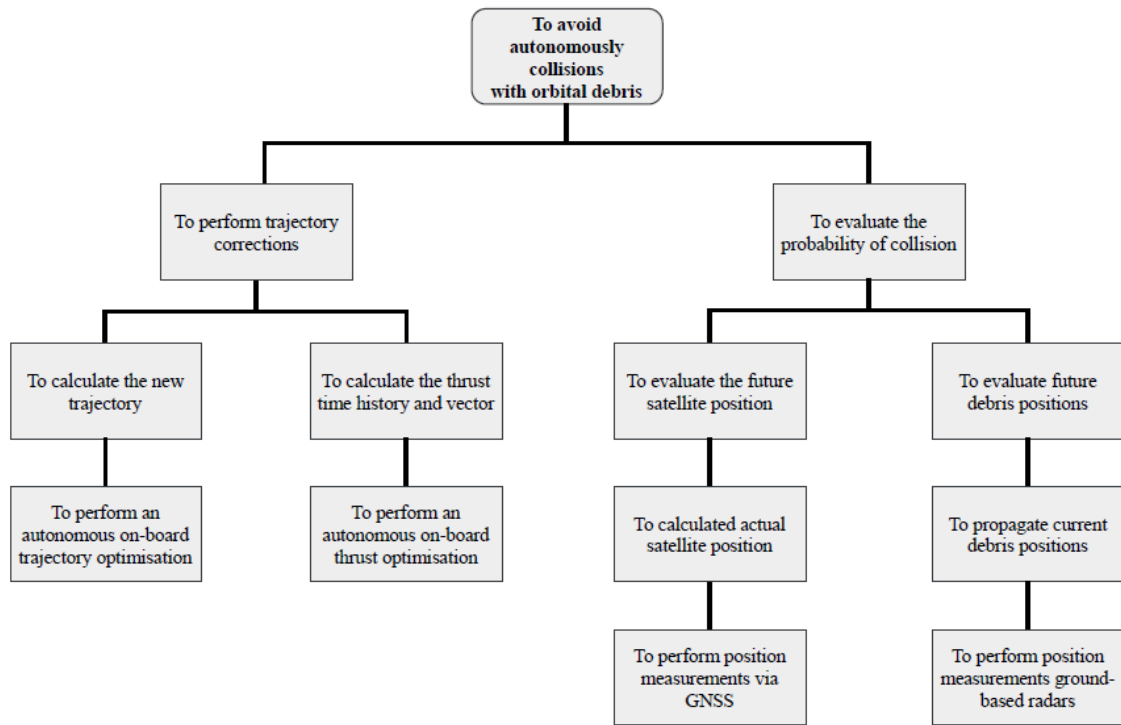


Figure 20. GNC functional tree

Following a top-down direction, in the first level we find the two blocks defining how to avoid a collision: modify the actual trajectory and the evaluation of the probability of collision. The new trajectory will be calculated through an optimised thrust law, while the current and propagated positions of satellite and debris allow computing the probability of collision.

In the following figure, the functional architecture for the GNC system is illustrated. The guidance block manages all the operations to decide the path of travel that in any case is determined by the OBC. The guidance block communicates the commanded trajectory to the control block receiving the estimated position of the satellite. The control block enables the thruster to

activate the manoeuvre. The navigation block receives data about the estimated trajectory and state vector, giving in output information about the state and the estimated thrust vector.

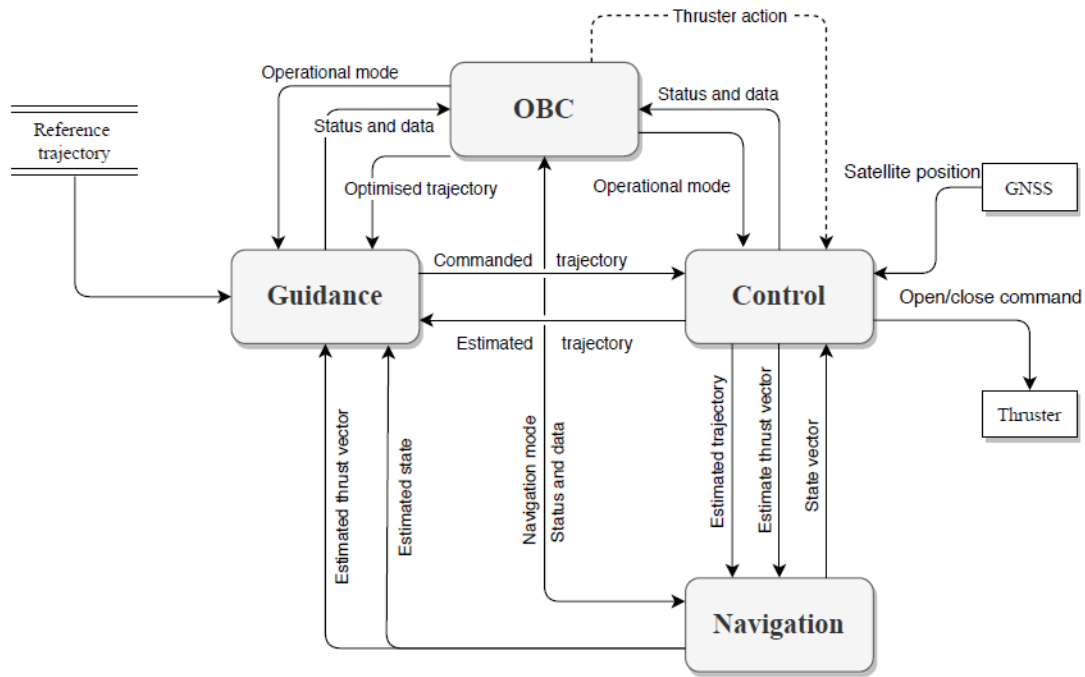


Figure 21. GNC functional architecture

3.5.2 ADCS functional architecture

Following the same path of the GNC functional architecture, the main purpose of this satellite is an autonomous reorientation to cover all the defined targets. To accomplish this task a constellation is generally required because a single satellite could not provide an efficient outcome. Considering a single satellite, the functional tree for ADCS is presented below. The first level outlines how to observe the targets: performing an attitude reorientation and knowing the targets. The autonomous reorientation requires the calculation of the attitude path and meeting the constraints; the knowledge of the targets requires an exchange of data amongst the satellite in the

constellation or directly with the ground station that is the only capable element to update the targets.

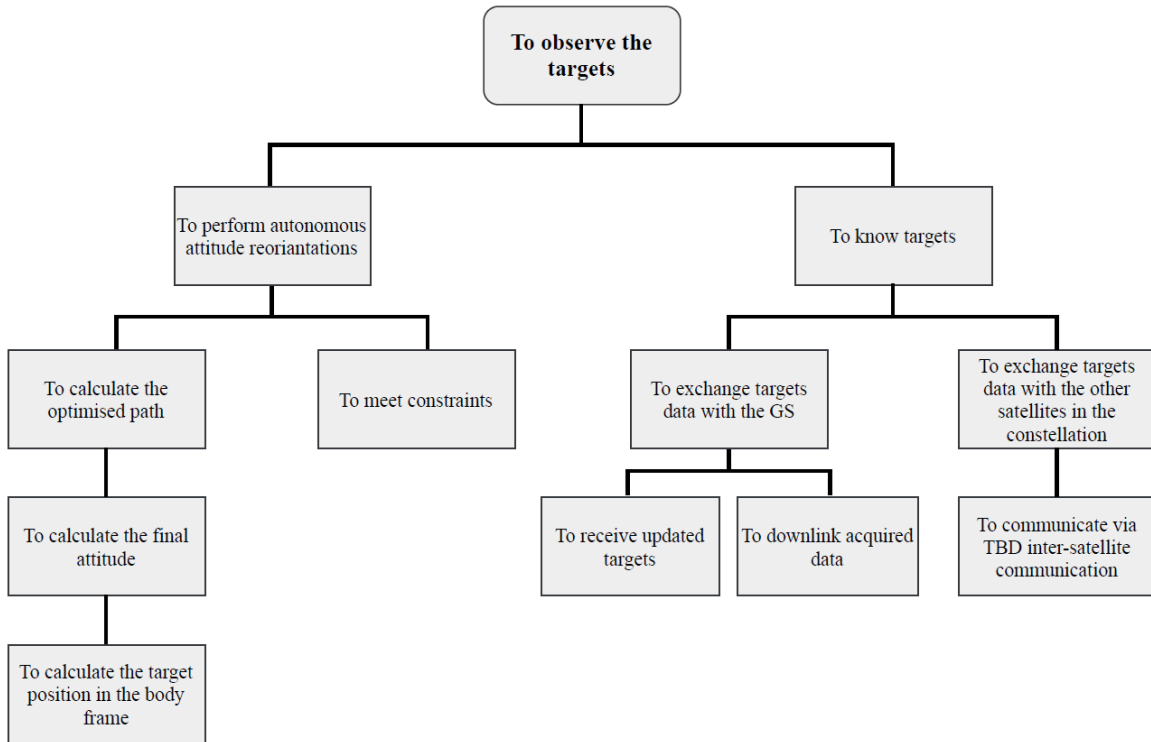


Figure 22. ADCS functional architecture

In the next figure, the functional architecture for ADCS is shown. As it is shown, there exists a synergy between the ADCS and the GNC system. The mounted sensors record data about the attitude while the IMU measures the angular velocities, accelerations, and the current attitude. ADCS's OBC elaborates this information to calculate the current attitude. The targeted pointing is the input for the reorientation given the point the attitude path optimisation is made to reach the desired position. At this stage, a collaboration with the GNC system allows calculating the final attitude considering that the satellite moves along the orbit. At this end, a control

signal is generated, sent to the reaction wheels modifying the satellite attitude.

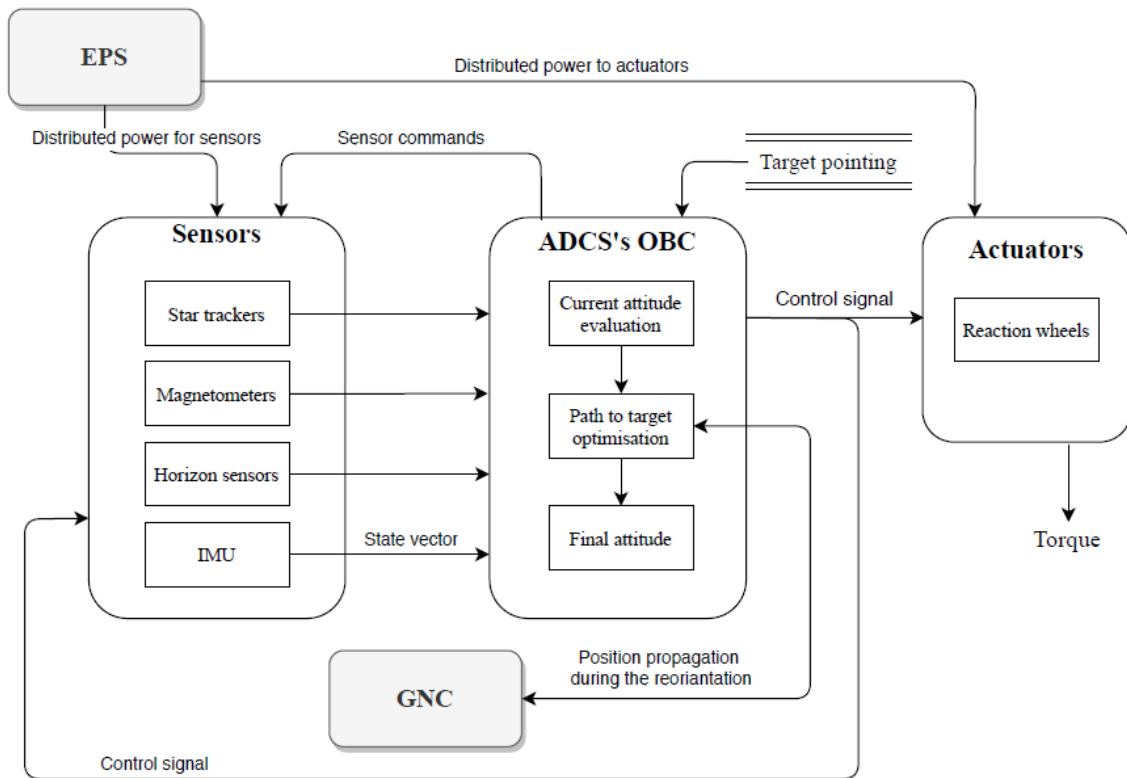


Figure 23. ADCS functional architecture

3.6 Functional architecture of other subsystems

The functional architectures of the other subsystems are here presented. Specifically, OBC, TCS, COMMSYS, Propulsion system, EPS, and payload will be shown.

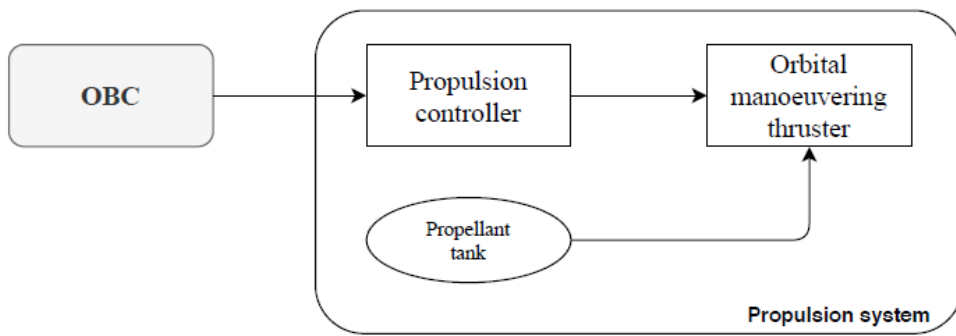


Figure 24. Propulsion system functional architecture

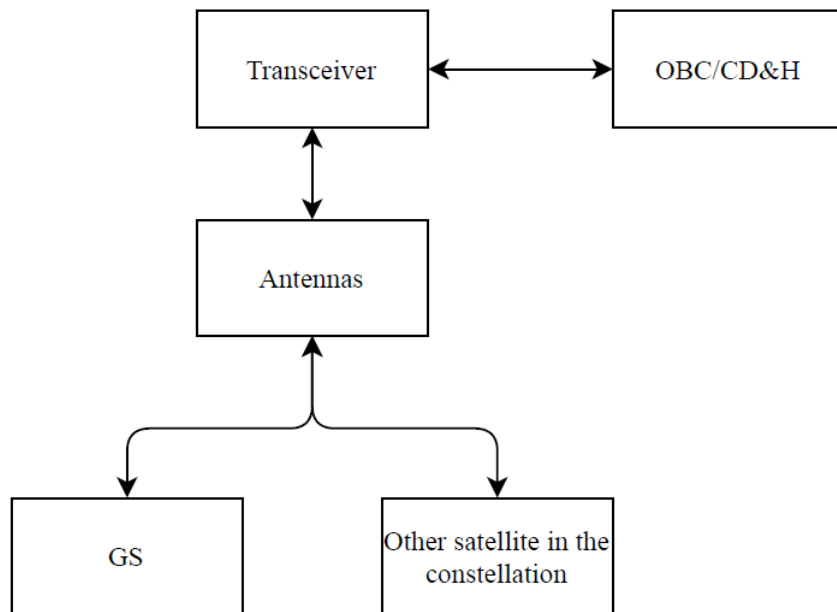


Figure 25. COMMSYS functional architecture

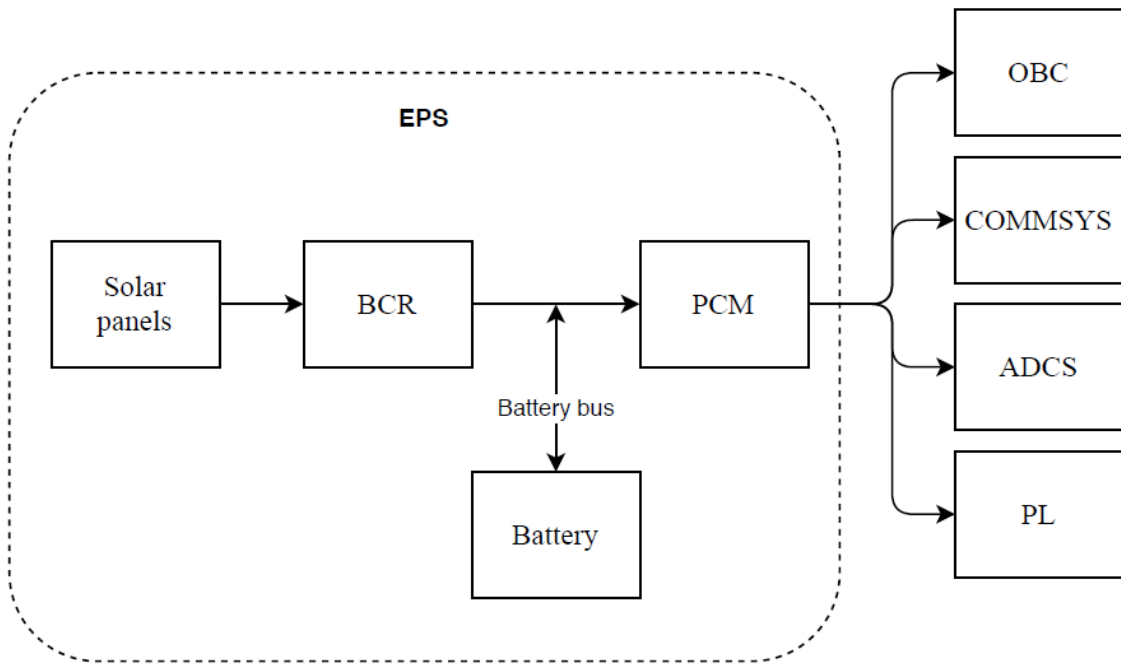


Figure 26. EPS functional architecture

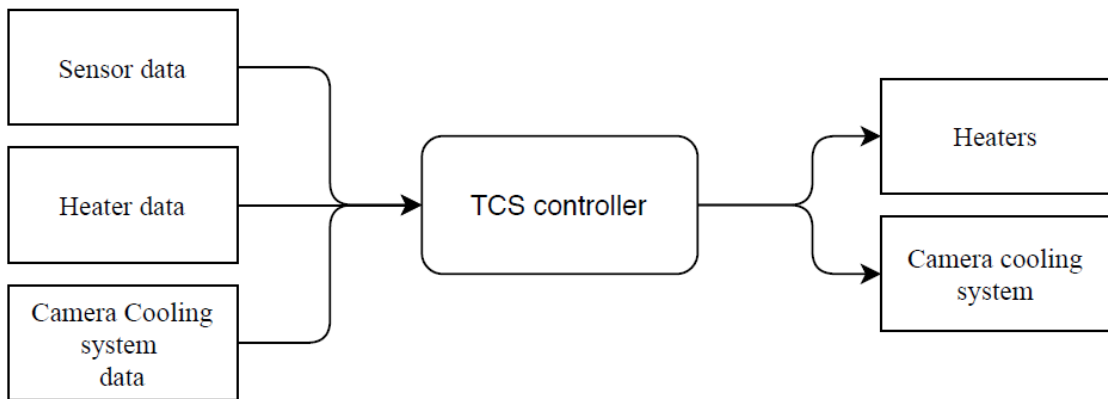


Figure 27. TCS functional architecture

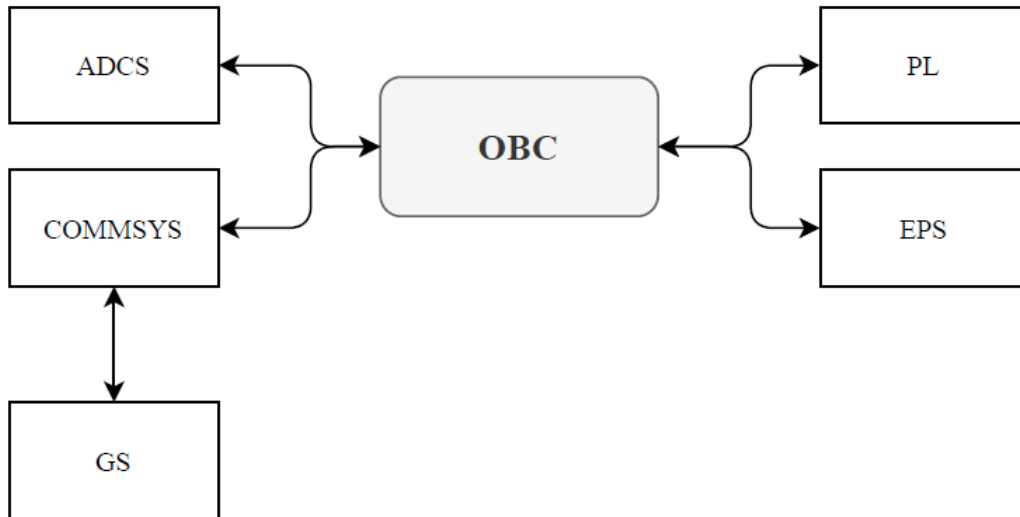


Figure 28. OBC functional architecture

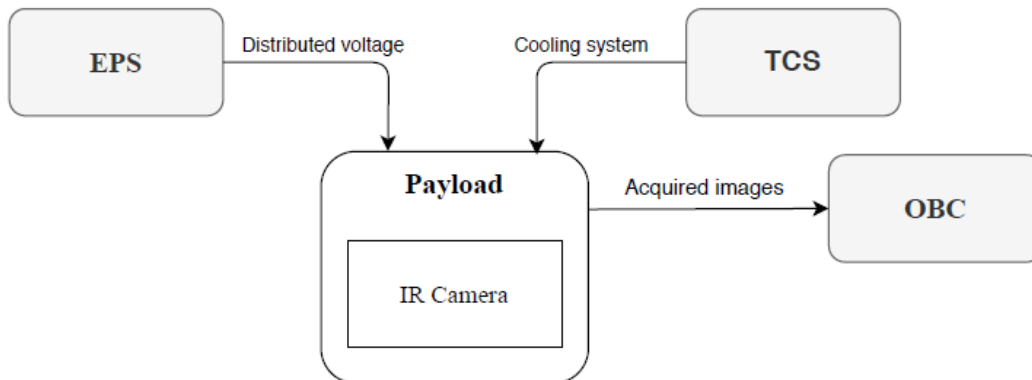


Figure 29. Payload functional architecture

It is possible to notice the interconnections amongst the subsystems, in particular with the OBC that is the system regulating all the processes on the satellite.

3.7 The role of the Ground Control Station

Ground Stations provide services in terms of telemetry, tracking, control during all the satellite arc life, from the launch segment to the navigation,

position maintenance, and deorbiting phase. Dealing with autonomous satellites, the classical role of the ground station changes. The production and development of autonomous satellites aspire to reduce the workload on ground operators, trying to maintain only the necessary operations that cannot be substituted by autonomous processes or that could apport a not acceptable level of risk. An illustrative comparison between a ground-dependent satellite (GDS) and an autonomous satellite (AS) is here reported, according to the current mission.

	GDS	AS
Position propagation of the satellite	GS operator	On-board
Position propagation of the debris	GS operator	On-board
Time of closest approach	GS operator	On-board
Probability of collision	GS operator	On-board
Information about the current position	On-board	On-board
Control law for orbit maintenance	GS operator	On-board
Trajectory change	GS operator	On-board
Reorientation path	GS operator	On-board
Sequence of targets	GS operator	On-board
Updating of targets	GS operator	GS operator

Table 7. Differences between a Ground-dependent satellite and an autonomous satellite

Thanks to the innovations brought to the satellite the GS will not have to provide a constant control on the satellite but only for those operations believed risky, not possible to implement on-board or in given situations like a constellation rephasing in case of failure of one of the satellites in the constellation, actions requiring a high computational cost.

The new role of the control segment will consist of satellite maintenance, analysis of housekeeping data (if required) and mission data analysis. The

idea would be to create a new abstract entity of ground station in which the level of autonomy itself is increased, reducing the software for remote operations [26]. Doing so, not only the space segment would have a high level of autonomy but also the ground station, reducing in this way the operational cost.

3.8 Satellite CAD model

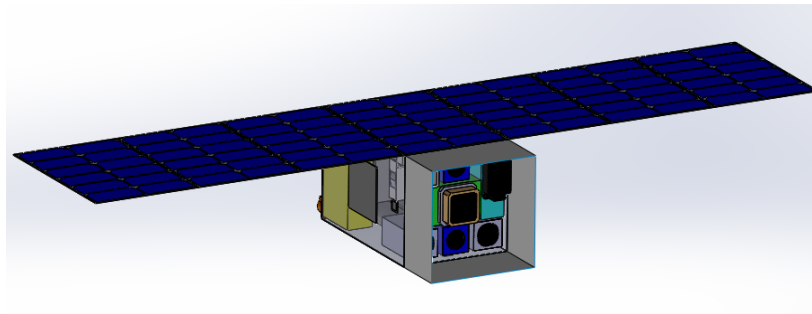
The main purpose of the CAD model is to derive the inertia matrix of the satellite and its shape. The inertia matrix is fundamental in attitude control, while the shape is useful to obtain information about disturbance torques caused by atmospheric drag, solar radiation pressure and Earth magnetic field and, in advanced phases of the study to calculate the exact drag due to the atmosphere.

Since the camera will work in the IR band it is mandatory having the face of the satellite as cold as possible to obtain better images and faster manner. To accomplish this scope a sunshield could be useful for this purpose. A little sunshield is mounted to avoid sunlight coming into the camera for certain attitudes.

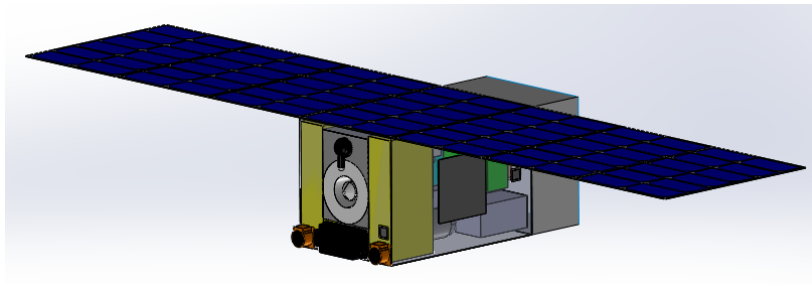
Main components singularly considered are:

- IR camera
- Cooling system
- Magnetorquers
- Magnetometers
- Reaction wheels
- Sun and horizon sensors
- IMU
- Hall-effect thruster
- Tanks
- Patch antennas for communication and GPS
- Solar panels

For these components, their weight has been calculated from datasheets. Other components have been represented with a box, like avionics, batteries.



(a)



(b)

Figure 30. CAD model. Front (a) and back (b) view

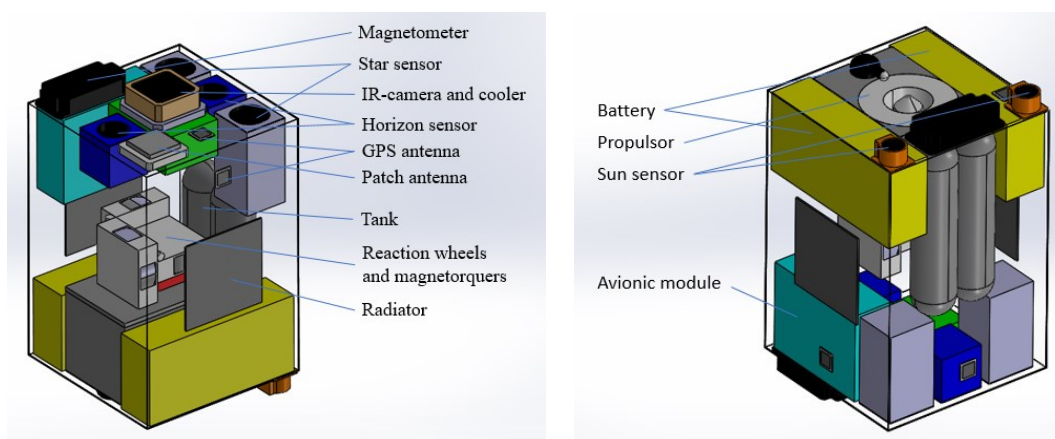


Figure 31. CAD model. Internal views

Referring to [24], ΔV budget has been computed taking into account an orbit maintenance at 600 km and an orbit lowering up to 400 km for decay. The necessary ΔV estimated for the mission is 80 m/s considering a margin of 20%. It is possible to calculate the fuel needed for a first approximation of the tank volume using the Tsiolkovsky equation

$$\frac{m_F}{m_0} = 1 - e^{-\frac{\Delta V}{v_e}} \quad 3.1$$

The total weight of the CAD model is about 15 kg. The mass fuel needed to accomplish the mission is 0.092 kg.

Parameter	Unit measure	Value
ΔV	m/s	80
v_e	km/s	13
m_0	Kg	15
m_P	Kg	0.092
V	cm ³	1469.19

Table 8. Tank volume determination

The fuel used for hall-effect thruster is xenon. At standard conditions (101325 Pa, 298.15K) its density is 5.761 kg/m³: the volume needed at standard conditions is 1469.19 cm³. To optimise the volume and the components collocation inside the satellite, xenon should be compressed to reduce the tank volume. However, high pressure will increase the tank thickness, so a compromise between tank weight and volume should be met.

Component	Weight [kg]
Structure	0.62
Solar panel	2.5
RWs	0.33
Batteries	2.5
Cooler and radiator	0.65
IMU	0.2
IR-Camera	0.1
Magnetometers	0.08
Sun and horizon sensors	0.32
Magnetorquers	0.09
Hall-effect propulsor	1.08
Tanks and fuel	1.2
Star trackers	0.6

Table 9. Component weights

The satellite is equipped with 7 foldable solar panels that provide a total area of 4200 cm². The power produced is

$$P_{out} = \eta \sigma_{sun} A_{sp} = 218.65W \quad 3.2$$

where η is the solar panel efficiency (0.38), σ_{sun} is the solar radiation power (1370 W/m²). This is the maximum power that can be provided. However, the angle between the solar array and the solar rays θ which contributes to decrease the power in output needs to be considered for the power budget.

Each side of the satellite is equipped with a GNSS strip patch antenna that allows communication in terms of position with other satellites in the constellation or with GNSS services for positioning. A bigger patch antenna is mounted on the bottom face for data transfer.

Onboard Attitude sensors are magnetometers, horizon sensors, sun sensors, star trackers, while reaction wheels and magnetorquers shall be used to control the attitude. The attitude control system (ACS) provides a pointing accuracy of ± 0.002 deg.

The resultant inertia matrix is

$$J = \begin{bmatrix} 0.847 & 0.01 & -0.005 \\ 0.01 & 0.905 & 0.01 \\ -0.005 & 0.01 & 0.173 \end{bmatrix}$$

Computed in the centre of mass of the satellite.

4

Principles of non-linear programming

Because of the increasing complexity in every field of engineering applications the theory of optimal control has been becoming to be applied through computation. Computational optimal control has developed in several methods that made as a result the number of implementation software to grow [27].

The concept at the basis of every computational problem is solving a difficult problem dividing it in sequence of simpler subproblems [28]; the solution of an optimal control problem requires the solution of subproblems defined in one or more finite dimension. To reach this purpose the non-linear programming (NLP) tries to find a finite number of variables so that an objective function is optimised observing some imposed constraints.

In this work two methods of computational calculus have been adopted: pseudo-spectral methods and a heuristic method. The choice of these has been done because their results found in the literature. Pseudo-spectral methods are gradient-based methods, meaning that the convergence is strictly related to the initial guesses. However, it has a fast convergence, how it has been demonstrated for certain problems. Heuristic methods have a different approach to find a solution. They find a solution to the information gathered during the iterations. Evolutionary algorithms like genetic algorithms,

particle swarm optimisation, differential evolution algorithms are heuristic methods which find the solution through an exchange of information gathered by their population. Particle swarm optimisation is the heuristic method that will be used.

Pseudo-spectral methods

- Gradient-based method
- Strongly dependent on initial conditions
- Low computational time
- Solution found near initial conditions
- Many fields of application

Particle swarm optimisation

- Heuristic method
- population-based
- Optimality found exchanging information among individuals
- Not needing initial conditions
- Relatively low computational time
- Looking for solution in all domain

4.1 Newton's method

More than 300 years ago Newton proposed an iterative scheme today is at the basis of the most computational programs. This method can be used in one or multiple variables, including some differences for each case.

4.1.1 One variable

Let us suppose we want to find the value of the variable x constrained by the function

$$c(x) = 0 \tag{4.1}$$

We denote x^* the solution and x its approximation. Newton approximate the non-linear function $c(x)$ keeping only the first two terms in a Taylor's expansion This makes a linear approximation at a new point \bar{x}

$$c(\bar{x}) = c(x) + c'(x)(\bar{x} - x) \quad 4.2$$

with $c'(x)$ first derivative of $c(x)$. It is now reasonable to compute \bar{x} , which is a new estimation of the root, as

$$\bar{x} = x - [c'(x)]^{-1}c(x) \quad 4.3$$

If the new point gives a better result it makes sense to repeat the process as

$$x^{(k+1)} = x^{(k)} - [c'(x^{(k)})]^{-1}c(x^{(k)}) \quad 4.4$$

This sequence converges to exact value x^* if

$$\lim_{k \rightarrow \infty} |x^{(k)} - x^*| = 0 \quad 4.5$$

This definition could lead to have infinite iterations; but we are interested in terminating the sequence when the approximated solution is near to the answer. It is important to define the rate of convergence which measure the efficiency of an algorithm. For Newton's method, the rate of convergence is said to be quadratic.

4.1.2 Multiple variables

We now consider a generic function of many variables. Let us consider the n -vector composed as $\mathbf{x}^T = (x_1, \dots, x_n)$ so that

$$\mathbf{c}(\mathbf{x}) = \begin{bmatrix} c_1(\mathbf{x}) \\ \vdots \\ c_m(\mathbf{x}) \end{bmatrix} = \mathbf{0} \quad 4.6$$

where n is the number of variables and m the number of constraints. We assume that $n = m$. As in the case of Newton's method in one variable, the constraint function can be linearized

$$\mathbf{c}(\bar{\mathbf{x}}) = \mathbf{c}(\mathbf{x}) + \mathbf{G}(\bar{\mathbf{x}} - \mathbf{x}) \quad 4.7$$

with \mathbf{G} Jacobian matrix defined by

$$\mathbf{G} \equiv \frac{\partial \mathbf{c}}{\partial \mathbf{x}} = \begin{bmatrix} \frac{\partial c_1}{\partial x_1} & \frac{\partial c_1}{\partial x_2} & \cdots & \frac{\partial c_1}{\partial x_n} \\ \frac{\partial c_2}{\partial x_1} & \frac{\partial c_2}{\partial x_2} & \cdots & \frac{\partial c_2}{\partial x_n} \\ \vdots & \vdots & \ddots & \vdots \\ \frac{\partial c_m}{\partial x_1} & \frac{\partial c_m}{\partial x_2} & \cdots & \frac{\partial c_m}{\partial x_n} \end{bmatrix} \quad 4.8$$

In a similar way to the case in one variable we solve the linear system

$$\mathbf{G}(\bar{\mathbf{x}} - \mathbf{x}) = -\mathbf{c}(\mathbf{x}) \quad 4.9$$

Newton's method in several variables has the same properties of its counterpart: it has quadratic convergence and it may diverge if global strategies are not used. Furthermore, it is necessary the calculation of the Jacobian \mathbf{G} for each iteration, which can be computationally costly.

4.2 Optimal control problem formulation

A Single-Objective Optimal Control Problem is generally solved by finding the state trajectories, the control trajectories, and initial and final, which minimize the cost function [29]. The problem is formulated as

$$J = \Phi[x(t_f), t_f] + \int_{t_0}^{t_f} L[x(t), u(t), t] dt \quad 4.10$$

where $x(t)$, $u(t)$ are respectively the state and control trajectories. ϕ is the endpoint cost and L is the integrand cost. These two terms take the name of Mayer and Lagrange cost, respectively. A single-objective control problem is constrained as follow and the solution must satisfy them

$$\dot{x} = f[x(t), u(t), t] \text{ with } t \in [t_0, t_f] \quad 4.11$$

$$h_l \leq h[x(t), u(t), t] \leq h_u \text{ with } t \in [t_0, t_f] \quad 4.12$$

$$e_l \leq e[x(t_0), x(t_f), u(t_0), u(t_f), t_0, t_f] \leq e_u \quad 4.13$$

with \dot{x} system dynamics in the form of differential constraints, h and e path and event constraints. States, controls and time are also bounded

$$u_l \leq u(t) \leq u_u \text{ with } t \in [t_0, t_f] \quad 4.14$$

$$x_l \leq x(t) \leq x_u \text{ with } t \in [t_0, t_f] \quad 4.15$$

$$t_{0l} \leq t_0 \leq t_{0u} \quad 4.16$$

$$t_{fl} \leq t_f \leq t_{fu} \quad 4.17$$

$$t_f - t_0 \geq 0 \quad 4.18$$

4.3 Introduction to pseudo-spectral methods

Pseudo-spectral methods are a specific class of direct collocation methods [27]. What characterize this approach is approximation of the state and control using global polynomials and the collocation of the differential-algebraic equations is made at orthogonal collocation points. These kinds of collocation points are the roots of an orthogonal polynomial and/or a linear combination of an orthogonal polynomial and its derivatives. An orthogonal polynomial is a class of polynomial which obey to an orthogonality relation. These methods are related to spectral methods, but integrate the basis adding a pseudo-spectral basis, allowing the representation of functions on a quadrature grid.

Pseudo-spectral methods are known for their characteristic to converge spectrally, that means their convergence to the solution is faster than any power N^{-m} where N is the number of collocation points and m any finite value.

Three most commonly sets of orthogonal collocation points used in a pseudo-spectral method are:

- Legendre-Gauss (LG)
- Legendre-Gauss-Radau (LGR)
- Legendre-Gauss-Lobatto (LGL)

All of them are obtained from the roots of a Legendre polynomial and/or linear combinations of a polynomial and its derivatives. These three sets are defined in the interval $[-1,1]$. What differs amongst them is that LG collocation points do not consider none of the endpoints, LGR collocation points consider one of them, LGL collocation points consider both endpoints. Moreover, LGR points are asymmetric with respect to the origin and can be defined using the initial or the terminal endpoint. These collocation points have culminated in three pseudo-spectral methods: the *Legendre pseudospectral method* (LPM), *Radau pseudo-spectral method* (RPM), *Gauss pseudospectral method* (GPM).

4.4 Mathematical principles of pseudo-spectral methods

PS methods are used to develop optimal control software to solve nonlinear control problems [30]. In this subchapter, it is shown a Gauss pseudo-spectral method to solve multi-phase optimal control problems.

In general, a PS algorithm is based on minimizing the cost functional

$$J = \sum_{p=1}^P \left[\Phi^{(p)}(\mathbf{x}^{(p)}(t_0), t_0^{(p)}, \mathbf{x}^{(p)}(t_f), t_f^{(p)}; \mathbf{q}^{(p)}) + \int_{t_0^{(p)}}^{t_f^{(p)}} \mathcal{L}^{(p)}(\mathbf{x}^{(p)}(t), \mathbf{u}^{(p)}(t), t; \mathbf{q}^{(p)}) dt \right] \quad 4.19$$

where $p = 1, \dots, P$, with the influence of the dynamic constraints

$$\dot{\mathbf{x}}^{(p)} = \mathbf{f}^{(p)}(\mathbf{x}^{(p)}, \mathbf{u}^{(p)}, t; \mathbf{q}^{(p)}) \quad 4.20$$

inequality path constraints

$$\mathbf{C}_{min}^{(p)} \leq \mathbf{C}^{(p)}(\mathbf{x}^{(p)}, \mathbf{u}^{(p)}, t; \mathbf{q}^{(p)}) \leq \mathbf{C}_{max}^{(p)} \quad 4.21$$

and the boundary conditions

$$\Phi_{min}^{(p)} \leq \Phi^{(p)}(\mathbf{x}^{(p)}, \mathbf{u}^{(p)}, t; \mathbf{q}^{(p)}) \leq \Phi_{max}^{(p)} \quad 4.22$$

And the linkage constraints

$$\mathbf{L}_{min}^{(s)} \leq \mathbf{L}^{(s)}(\mathbf{x}^{(p_l)}(t_f), t_f^{(p_l)}; \mathbf{q}^{(p_l)}, \mathbf{x}^{(p_s)}(t_0), t_0^{(p_s)}; \mathbf{q}^{(p_s)}) \leq \mathbf{L}_{max}^{(s)} \quad 4.23$$

with $p_l, p_s \in [1, \dots, P]$ and $s = 1, \dots, L$. The symbols used are (in the phase (p)):

- $\mathbf{x}^{(p)}(t) \in R^{n_x^{(p)}}$ the state
- $\mathbf{u}^{(p)}(t) \in R^{n_u^{(p)}}$ the control
- $\mathbf{q}^{(p)}(t) \in R^{n_q^{(p)}}$ static parameters
- $t \in R$ time
- L is the number of pairs to be linked and $p_l, p_s \in [1, \dots, P]$ and $s = 1, \dots, L$ are the left and the right phase numbers

n identifies the dimensions of the state, control, static parameter vector, path constraint vector and boundary conditions vector following their subscript.

It is important to note that the phases do not need to be sequential. The concept of the linkage is explained by the following figure.

The functions $\Phi^{(p)}$, $\mathcal{L}^{(p)}$, $f^{(p)}$, $C^{(p)}$ and $L^{(s)}$ are defined as below

$$\begin{aligned}
 \Phi^{(p)}: & \quad \mathbb{R}^{n_x^{(p)}} \times \mathbb{R} \times \mathbb{R}^{n_x^{(p)}} \times \mathbb{R} \times \mathbb{R}^{n_q^{(p)}} & \rightarrow & \quad \mathbb{R} \\
 \mathcal{L}^{(p)}: & \quad \mathbb{R}^{n_x^{(p)}} \times \mathbb{R}^{n_u^{(p)}} \times \mathbb{R} \times \mathbb{R}^{n_q^{(p)}} & \rightarrow & \quad \mathbb{R} \\
 f^{(p)}: & \quad \mathbb{R}^{n_x^{(p)}} \times \mathbb{R}^{n_u^{(p)}} \times \mathbb{R} \times \mathbb{R}^{n_q^{(p)}} & \rightarrow & \quad \mathbb{R}^{n_x^{(p)}} \\
 C^{(p)}: & \quad \mathbb{R}^{n_x^{(p)}} \times \mathbb{R}^{n_u^{(p)}} \times \mathbb{R} \times \mathbb{R}^{n_q^{(p)}} & \rightarrow & \quad \mathbb{R}^{n_c^{(p)}} \\
 \phi^{(p)}: & \quad \mathbb{R}^{n_x^{(p)}} \times \mathbb{R} \times \mathbb{R}^{n_x^{(p)}} \times \mathbb{R} \times \mathbb{R}^{n_q^{(p)}} & \rightarrow & \quad \mathbb{R}^{n_\phi^{(p)}} \\
 L^{(s)}: & \quad \mathbb{R}^{n_x^{(p_l^s)}} \times \mathbb{R} \times \mathbb{R}^{n_x^{(p_l^s)}} \times \mathbb{R}^{n_x^{(p_r^s)}} \times \mathbb{R}^{n_q^{(p_r^s)}} & \rightarrow & \quad \mathbb{R}^{n_L^{(p)}}
 \end{aligned}$$

$n_x^{(p)}$, $n_c^{(p)}$, $n_\phi^{(p)}$, $n_L^{(p)}$ are the dimensions of state, control, static parameter vector, path constraint vector and boundary condition vector in phase p while $n_L^{(p)}$ is the dimension of the vector formed by the s^{th} linkage constraint.

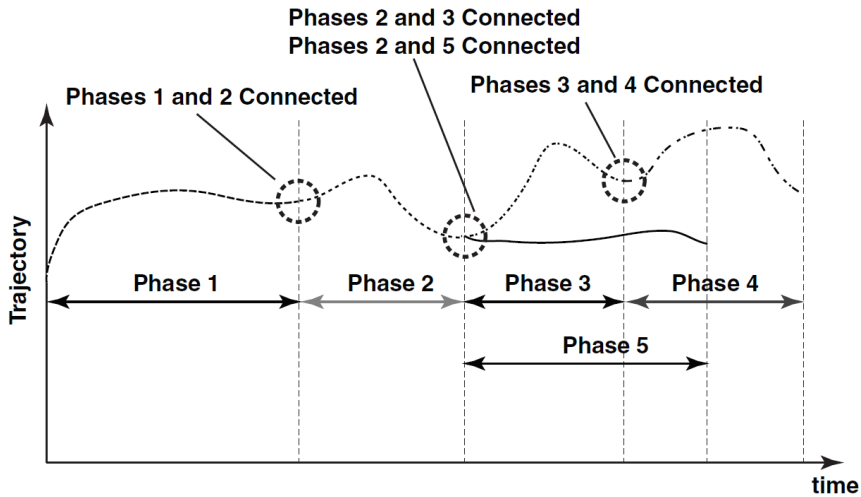


Figure 32. Schematic linkage for multiple-phase optimal control problem

4.4.1 Discretization

Let us consider p being a specific phase of an optimal control problem. For every phase of the problem, the independent variable t is transformed in the variable $\tau \in [-1,1]$

$$t^{(p)} = \frac{t_f^{(p)} - t_0^{(p)}}{2} \tau^{(p)} + \frac{t_f^{(p)} + t_0^{(p)}}{2} \quad 4.24$$

We suppose that the chosen collocation points are LG points, roots of the N^{th} degree Legendre polynomial given as

$$P_N = \frac{1}{2^N N!} \frac{d^N}{d\tau^N} [(\tau^2 - 1)^N] \quad 4.25$$

To the LG points, there are corresponding weights (for $i = 1, \dots, N$)

$$w_i = \frac{2}{(1 - \tau_i^2)[P_N']^2} \quad 4.26$$

The point used in the Gauss pseudo-spectral method are LG points, including the points $\tau_0 = -1$ and $\tau_{N+1} = 1$.

The state is approximated with Lagrange polynomials with basis $N + 1$, indicated as $L_i(\tau)$ ($i = 0, \dots, N$)

$$\mathbf{x}(\boldsymbol{\tau}) \approx \mathbf{X}(\boldsymbol{\tau}) = \sum_{i=0}^N \mathbf{X}(\boldsymbol{\tau}_i) L_i(\tau) \quad 4.27$$

Where the Lagrange polynomials $L_i(\tau)$ are defined as

$$L_i(\tau) = \prod_{j=0, j \neq i}^N \frac{\tau - \tau_j}{\tau_i - \tau_j} \quad 4.28$$

The cost functional is approximated using the Gauss quadrature at the values of the state, control and time at the LG points.

$$J = \sum_{p=1}^P \Phi^{(p)}(\mathbf{X}_0^{(p)}, t_0^{(p)}, \mathbf{X}_f^{(p)}, t_f^{(p)}) + \sum_{p=1}^P \frac{t_f^{(p)} - t_0^{(p)}}{2} \sum_{k=1}^{N^{(p)}} w_k^{(p)} \mathcal{L}^{(p)}(\mathbf{X}_k^{(p)}(t), \mathbf{U}_k^{(p)}(t), \tau_k^{(p)}; \mathbf{q}^{(p)}, t_0^{(p)}, t_f^{(p)}) \quad 4.29$$

Differentiate the equation (4.27) with respect to τ we have

$$\frac{d\mathbf{X}}{d\tau} \approx \sum_{i=0}^N \mathbf{X}(\tau_i) \frac{dL_i(\tau)}{d\tau} \quad 4.30$$

Each derived Lagrange polynomial can be represented in the form of differentiation matrix $\mathbf{D} \in \mathbb{R}^{N \times N+1}$

$$\mathbf{D}_{ki} = \dot{L}_i(\tau_k) = \sum_{l=0}^N \frac{\prod_{j=0, j \neq i, l}^N (\tau_k - \tau_j)}{\prod_{j=0, j \neq i}^N (\tau_i - \tau_j)} \quad 4.31$$

The dynamic constraint is

$$\sum_{i=0}^N \mathbf{D}_{ki} \mathbf{X}_i - \frac{t_f - t_0}{2} \mathbf{f}(\mathbf{X}_k, \mathbf{U}_k, \tau_k; \mathbf{q}, t_0, t_f) = \mathbf{0} \quad (k = 1, \dots, N) \quad 4.32$$

Let us define an additional variable $\mathbf{X}_f \equiv \mathbf{X}_{N+1} \equiv \mathbf{X}(\tau_f)$

$$\mathbf{X}_0 = \mathbf{X}(\tau_0) \quad 4.33$$

$$\mathbf{X}_{N+1} = \mathbf{X}_0 + \frac{t_f - t_0}{2} \sum_{k=1}^N w_k \mathbf{f}(\mathbf{X}_k, \mathbf{U}_k, \tau_k; \mathbf{q}, t_0, t_f) \quad 4.34$$

Adding this variable, the previous equation (4.35) becomes an additional constraint. Equation (4.32) is used to solve \mathbf{f} , then the result is substituted in equation (4.35)

$$\mathbf{X}_{N+1} - \mathbf{X}_0 - \sum_{i=0}^N \sum_{k=1}^N w_k \mathbf{D}_{ki} \mathbf{X}_i = \mathbf{0} \quad 4.35$$

In the same way the path constraints are discretised as

$$\mathbf{C}_{min} \leq \mathbf{C}(\mathbf{X}_k, \mathbf{U}_k, \boldsymbol{\tau}_k, \mathbf{q}, t_f) \leq \mathbf{C}_{max} \quad (\mathbf{k} = \mathbf{1}, \dots, N) \quad 4.36$$

and the boundary conditions as

$$\Phi_{min} \leq \Phi(\mathbf{X}_0, t_0, \mathbf{X}_{N+1}, t_f) \leq \Phi_{max} \quad 4.37$$

The linkage constraints are defined using the initial and final values of a pairs of phases

$$\begin{aligned} \mathbf{L}_{min}^{(s)} &\leq \mathbf{L}^{(s)} \left(\mathbf{X}_{N+1}^{(p_l^s)}, t_f^{(p_l^s)}; \mathbf{q}^{(p_l^s)}, \mathbf{X}_0^{(p_u^s)}, t_0^{(p_u^s)}; \mathbf{q}^{(p_u^s)} \right) \\ &\leq \mathbf{L}_{max}^{(s)}, \quad p_l, p_u \in [1, \dots, P] \\ &\quad s = 1, \dots, L \end{aligned} \quad 4.38$$

4.5 Features of pseudo-spectral methods

PS methods have been having a large use in literature to solve various problem of different nature, not only engineering issues: one of their use is in medicine for nonlinear ultrasound propagation in biological tissue. It is a promising method with high capabilities. The main advantages of PS methods are the computational cost: it is possible to obtain the required accuracy with a small number of space grid points [31]. Another feature of the PS method is that they are gradient-based methods: the optimal solution is found using extensive information of the objective function during iterations to minimize

the cost function. This can be an advantage or a drawback. PS methods are sensible to initial guesses. The time of convergence is related to the proximity of initial guesses to the expected results. Initial conditions are essential in solving a problem using PS methods because it makes the difference in solving the problem in an acceptable time or not. Moreover, initial guesses are essential to locate the global minimum of the problem: if initial conditions are near a local minimum, the convergence could be to local minimum rather than a global one. Lastly, the time of convergence is directly related to the “slope” of the gradient: if the minimum of the cost function is located in a “smooth” gradient, the method will require more time to converge to an optimal solution.

4.6 Results of Pseudo-spectral methods applied to orbital and attitude problems

It has been shown in literature the use of PS methods to solve orbital problem related to orbit transfer and space-based attitude regulations. In particular in ref. [32, 33] is shown the possibility of orbit transfer using low thrust optimizing time considering or not the eclipsing phase of the satellite. In these works, LEO-GEO orbit transfers are presented, receiving as output from the optimiser the optimal control law to reach the desired results. However, computational time and the used hardware platform are not mentioned. In this thesis it has been tried to adopt a PS method for a simple orbit transfer, neglecting every kind of perturbation. What has been obtained is a non-convergence in an acceptable time: convergence time is estimated to be greater than 1 hour. The adopted platform is Intel(R) Core(TM) i7-3537U CPU @ 2.00-2.50 GHz, 64 bit, 10GB RAM. In the table below initial and final conditions are shown, using a constant thrust of $13 \cdot 10^{-3}$ N.

		Initial conditions	Final conditions
m	kg	15	Free
h	km	600	600.5
e		10^{-5}	10^{-5}
i	deg	30	30
ω	deg	0	0
Ω	deg	0	0
v	deg	0	Free

Table 10. Initial and final parameters for optimisation using a PS method

Other works in literature show the capability of PS methods in attitude regulations [34, 35]. The work in ref. [35] is interesting because it shows the difference in using a pure PS method or the difference in adopting Bézier curves for initial guesses. It has been shown that a pure PS method, using low tolerances, has long time for convergence, about 300 s; instead using Bézier curves to find a possible solution as initial guess for PS method, it is possible to reduce the total calculation time (for possible solution + PS method) up to 80%.

For this work of thesis, the application of a pseudo-spectral method for optimal control has been tried and set aside due to unacceptable computational time for orbit transfer.

5

Particle Swarm Optimisation

Particle swarm optimisation is part of those algorithms called evolutionary because of their ability to emulate biological behaviour. An evolutionary algorithm can be defined as a generic population-based metaheuristic optimisation algorithm. The advantage of EAs is that it is not required to provide any initial guess and, compared to other methods, they find the best solution for the global minimum in the search space. Candidate solutions have the behaviour of individuals in a population and the fitness function determine the solution quality. Particle Swarm Optimisation is an algorithm modelled on natural swarm behaviour and it can be used to generate initial guesses for designing fuel-optimal trajectories [36]. This optimisation method was introduced by Kennedy and Eberhart [37] in 1995 as an algorithm derived from behaviour found in nature.

5.1 Particle Swarm Optimisation algorithm

The PSO is a population-based optimiser. Its mechanism is started by randomly initializing a set of possible solutions, then the optimum is repetitively searched. The optimal solution is found following the best particles.

5.1.1 Basics of PSO

To better understand the algorithm, we can imagine a swarm of bees. The swarm naturally tends to move towards a higher concentration of flowers although it has no previous knowledge of the field. The insects start their research spreading in random locations and every bee can remember the visited location and which one had most flowers. This information is shared with the rest of the swarm. Each particle evaluates its consistency based on the system's function and keeps its best evaluation after each iteration. Based on social information, bees decide in which direction to move. In this way, the field is explored, and the best location is individuated.

5.1.2 PSO algorithm

A swarm is composed of p particles. Every particle represents a possible solution in the problem search space. The position for each particle i evolve as

$$x_{k+1}^i = x_k^i + v_{k+1}^i \quad 5.1$$

and the velocity v_i is calculated by

$$v_{k+1}^i = v_k^i + c_1 \cdot r_1 \cdot (p_k^i - x_k^i) + c_2 \cdot r_2 \cdot (p_k^g - x_k^i) \quad 5.2$$

where k represents the increment of time, p_k^i is the best position of the particle i at the time k and p_k^g is the global best position amongst all the particles at the time k . Both r_1 and r_2 are random numbers between 0 and 1, while c_1 and c_2 represent the cognitive and social scaling parameters respectively; these are equal to 2 to give a mean of 1 when multiplied by r_1 and r_2 . The equation of velocity is used to determine a new velocity for the particles while the position equation updates the particle position. Let us

denote the best fitness value as f_{best}^i and f_{best}^g for the i^{th} particle and globally respectively. A general pseudocode is shown.

STEP 1. Initialization

- (a) Set constant k_{max} , c_1 and c_2
- (b) Initialization of particle positions in the problem space x_0^i for p particles
- (c) Initialization of particle velocities in the problem space v_0^i for p particles
- (d) Set $k = 1$

STEP 2. Optimisation

- (a) Evaluate the function value f_k^i
- (b) If $f_k^i \leq f_{best}^i$ then $f_{best}^i = f_k^i$, $p_k^i = x_k^i$
- (c) If $f_k^i \leq f_{best}^g$ then $f_{best}^g = f_k^i$, $p_k^g = x_k^i$
- (d) If the stopping criterion is satisfied go to step 3
- (e) Particle velocities are updated
- (f) Particle positions are updated
- (g) Time is updated $k = k + 1$
- (h) Go to step 2(a)

STEP 3. Termination

An initial number of particles in the swarm is defined at the beginning. Those particles are then randomly allocated in the search space domain and a fitness function is evaluated for each particle, determining the best solution among all of them. The position of each particle is then updated calculating

its velocity, position, making sure to be located within the parameter bounds. The personal and global best solution are then updated.

Particle Swarm Optimisation could be useful for those problems which are unconstrained, although some constraints usually need to be satisfied to obtain a feasible and then optimal solution. In this thesis, the method employed consists of a penalty function approach depending on the type of constraint.

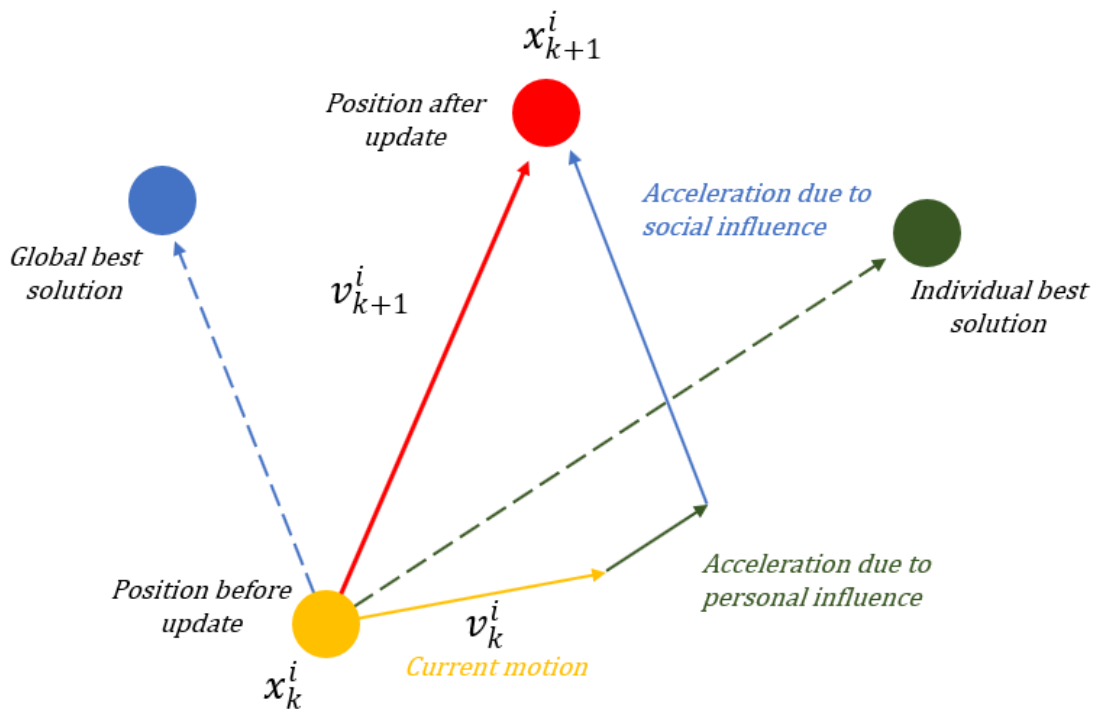


Figure 33. PSO particle position updating scheme

6

Mathematical models for optimisation

In this chapter models adopted for trajectory optimisation and attitude reorientation will be shown. In paragraph 6.1 trajectory optimisation is described presenting its mathematical model, while attitude reorientation is illustrated in paragraph 6.2.

6.1 Orbital manoeuvre optimisation model

In the first phase the orbit model has been developed including effects of spherical harmonics. These perturbations are used to model the Earth's gravitational field and the RAAN and argument of perigee regression. Along the motion on its orbit the spacecraft is typically considered to be a point-mass. To describe a three-dimensional motion six parameters are required, each of them representing a spacecraft state. The spacecraft state can be represented in various ways having positive or negative features [38]. The most notorious are here presented:

- **Cartesian State Vector (CSV):** This model refers to the spacecraft position and velocity vectors. The state vector representing the coordinates on an inertial frame is $\mathbf{x}_{CSV} = [r_x \ r_y \ r_z \ v_x \ v_y \ v_z]$ where $r = [r_x \ r_y \ r_z]$ is position vector and $v = [v_x \ v_y \ v_z]$ the velocity vector.

- **Polar State Vector (PSV):** They are usually referred to a two-dimensional problem. The state vector is $\mathbf{x}_{PSV} = [r \ \vartheta \ v \ \psi]$ where r represents the distance from the central body, ϑ the polar angle, v the velocity in modulus and ψ the flight path angle.
- **Classical Orbital Elements (COE):** This is another form to represent the dynamics $\mathbf{x}_{COE} = [a \ e \ i \ \omega \ \Omega \ v]$ where their names are respectively semi-major axis, eccentricity, inclination, argument of perigee, right ascension of the ascending node, true anomaly.
- **Modified Equinoctial Elements (MEE):** This model utilises the modified equinoctial orbital elements $\mathbf{x}_{MEE} = [p \ f \ g \ h \ k \ L]$. p is the semi-latus rectum, f and g are related to the orbit eccentricity, h and k to the orbit inclination and L is the true longitude.

The easiest way to determine the orbit along a certain period of time could be the integration of the gaussian variational equations of the classical orbital elements $(a, e, i, \omega, \Omega, v)$ [28]; however using the classical orbital elements some singularities may appear for null eccentricities, null inclinations or close to 90 deg. To avoid these singularities a set of equinoctial orbital elements was developed by Kechichian [39] to solve a low thrust earth orbit transfer. The relationship between classical orbital elements and modified equinoctial elements can be described by these equations:

$$p = a(1 - e^2) \tag{6.1}$$

$$f = e \cos(\omega + \Omega) \tag{6.2}$$

$$g = e \sin(\omega + \Omega) \tag{6.3}$$

$$k = \tan\left(\frac{i}{2}\right) \sin(\Omega) \tag{6.4}$$

$$h = \tan\left(\frac{i}{2}\right) \cos(\Omega) \tag{6.5}$$

$$L = \Omega + \omega + \nu \quad 6.6$$

where

p = semi-parameter

a = semi-major axis

e = orbital eccentricity

i = orbital inclination

ω = argument of perigee

Ω = right ascension of the ascending node (RAAN)

L = true longitude

The relationship amongst classical and modified equinoctial orbital elements is described by the following equations:

- Semi-major axis

$$a = \frac{p}{1 - f^2 - g^2} \quad 6.7$$

- Orbital eccentricity

$$e = \sqrt{(f^2 + g^2)} \quad 6.8$$

- Orbital inclination

$$i = 2 \arctan 2 \left(\sqrt{(h^2 + k^2)}, 1 - h^2 - k^2 \right) \quad 6.9$$

- Argument of perigee

$$\omega = \arctan 2 (gh - fk, fh + gk) \quad 6.10$$

- RAAN

$$\Omega = \arctan 2 (k, h) \quad 6.11$$

- True anomaly

$$\mathbf{v} = L - \Omega - \omega \quad 6.12$$

In these equations, the expression “arctan2” indicates the four-quadrant inverse tangent calculation. The relationship between the ECI state vector and modified equinoctial elements is

$$\mathbf{r} = \begin{bmatrix} \frac{r}{s^2} (\cos(L) + \alpha^2 \cos(L) + 2hk \sin(L)) \\ \frac{r}{s^2} (\sin(L) - \alpha^2 \sin(L) + 2hk \cos(L)) \\ \frac{2r}{s^2} (h \sin(L) - k \cos(L)) \end{bmatrix} \quad 6.13$$

$$\mathbf{v} = \begin{bmatrix} -\frac{1}{s^2} \sqrt{\left(\frac{\mu}{p}\right)} (\sin(L) + \alpha^2 \sin(L) - 2hk \cos(L) + g - 2f hk + \alpha^2 g) \\ -\frac{1}{s^2} \sqrt{\left(\frac{\mu}{p}\right)} (-\cos(L) + \alpha^2 \sin(L) + 2hk \sin(L) - f + 2ghk + \alpha^2 f) \\ \frac{2}{s^2} \sqrt{\left(\frac{\mu}{p}\right)} (h \cos(L) + k \sin(L) + fh + gk) \end{bmatrix} \quad 6.14$$

where

$$\alpha^2 = h^2 - k^2 \quad 6.15$$

$$s^2 = 1 + h^2 + k^2 \quad 6.16$$

$$r = \frac{p}{q} \quad 6.17$$

$$q = 1 + f \cos(L) + g \sin(L) \quad 6.18$$

Then the dynamic system can be described in terms of the new state variables

$$[\mathbf{y}^T, w] = [p, f, g, h, k, L, w] \quad 6.19$$

And the control variables

$$\mathbf{u}^T = [u_r, u_s, u_w] \quad 6.20$$

Using the modified equinoctial parameters, the equations of motion are defined by the following equations:

$$\dot{\mathbf{y}} = A(\mathbf{y})\Delta + \mathbf{b} \quad 6.21$$

$$\dot{w} = -T/I_{sp} \quad 6.22$$

The equinoctial dynamics is defined by matrix A, the perturbations Δ and the vector b.

$$A = \begin{bmatrix} 0 & \frac{2p}{q} \sqrt{\frac{p}{\mu}} & 0 \\ \sqrt{\frac{p}{\mu}} \sin(L) & \sqrt{\frac{p}{\mu}} \frac{1}{q} [(q+1) \cos(L) + f] & \sqrt{\frac{p}{\mu}} \frac{g}{q} [h \sin(L) - k \cos(L)] \\ -\sqrt{\frac{p}{\mu}} \cos(L) & \sqrt{\frac{p}{\mu}} \frac{1}{q} [(q+1) \sin(L) + g] & \sqrt{\frac{p}{\mu}} \frac{f}{q} [h \sin(L) - k \cos(L)] \\ 0 & 0 & \sqrt{\frac{p}{\mu}} \frac{s^2 \cos(L)}{2q} \\ 0 & 0 & \sqrt{\frac{p}{\mu}} \frac{s^2 \cos(L)}{2q} \\ 0 & 0 & \sqrt{\frac{p}{\mu}} \frac{1}{q} [h \sin(L) - k \cos(L)] \end{bmatrix} \quad 6.23$$

The vector

$$\mathbf{b}^T = \left[0 \quad 0 \quad 0 \quad 0 \quad 0 \quad \sqrt{\mu p} \left(\frac{q}{p} \right)^2 \right] \quad 6.24$$

The perturbation vector

$$\Delta^T = [\Delta_r \quad \Delta_s \quad \Delta_w] \quad 6.25$$

which is in general

$$\mathbf{\Delta} = \mathbf{\Delta}_{pert} + \mathbf{\Delta}_T \quad 6.26$$

sum of the perturbations due to spherical harmonics and low thrust.

In general, the motion of the spacecraft can be described by a system of a second-order ODEs

$$\ddot{\mathbf{r}} + \mu \frac{\mathbf{r}}{r^3} = \mathbf{a}_d \quad 6.27$$

Where r is the magnitude of the inertial position and \mathbf{a}_d is the disturbing acceleration. This equation is referred to as the Gauss form of the variational equation. What can be expected is that the disturbing acceleration is small and consequently we can expect that the solution can be described in terms of quasi constant orbital elements. Because of the small thrust applied to the spacecraft in the case of electric propulsor, this equation can be used when the spacecraft is equipped with electric propulsors.

The disturbing acceleration is replaced by $\mathbf{\Delta}$ if modifies equinoctial elements are used. The contribution to the perturbation vector are given by the Earth gravitational effects (harmonics) and the low thrust (when applied). The disturbing acceleration is expressed in a rotating radial frame whose principal axes are defined by

$$Q_r = [\mathbf{i}_r \quad \mathbf{i}_s \quad \mathbf{i}_w] = \left[\frac{\mathbf{r}}{|\mathbf{r}|} \quad \frac{(\mathbf{r} \times \mathbf{v}) \times \mathbf{r}}{|(\mathbf{r} \times \mathbf{v}) \times \mathbf{r}|} \quad \frac{(\mathbf{r} \times \mathbf{v})}{|(\mathbf{r} \times \mathbf{v})|} \right] \quad 6.28$$

Notice that when the disturbing acceleration is zero, the problem becomes a two-body problem.

6.1.1 Gravitational disturbing acceleration

Oblate gravity model is usually defined in a local horizontal reference frame, which is

$$\delta \mathbf{g} = \delta g_n \mathbf{i}_N - \delta g_r \mathbf{i}_r \quad 6.29$$

where

$$\mathbf{i}_N = \frac{\mathbf{e}_N - (\mathbf{e}_N^T \mathbf{i}_r) \mathbf{i}_r}{\|\mathbf{e}_N - (\mathbf{e}_N^T \mathbf{i}_r) \mathbf{i}_r\|} \quad 6.30$$

defines the local north direction with $\mathbf{e}_N^T = [0 \ 0 \ 1]$. The gravitational acceleration are given by

$$\delta g_N = -\frac{\mu \cos(\phi_{gc})}{r^2} \sum_{k=2}^4 \left(\frac{R_e}{r}\right)^k P'_k J_k \quad 6.31$$

$$\delta g_r = -\frac{\mu}{r^2} \sum_{k=2}^4 (k+1) \left(\frac{R_e}{r}\right)^k P_k J_k \quad 6.32$$

where ϕ_{gc} is the geocentric latitude, R_e is the equatorial radius of the Earth, r is the geocentric radius, $P_k(\sin \phi_{gc})$ is the k^{th} order Legendre polynomial and J_k are the zonal harmonic coefficients. To obtain the gravitational perturbation in the rotating radial frame, it follows that

$$\Delta_g = Q_r^T \delta \mathbf{g} \quad 6.33$$

Legendre polynomials are defined with the Rodrigue's formulation as

$$P_n(x) = \frac{1}{2^n n!} \frac{d^n}{dx^n} (x^2 - 1)^n \quad 6.34$$

while the geocentric latitude can be obtained knowing the geodetic latitude ϕ_{gd}

$$\phi_{gc} = \arctan[(1 - e^2) \tan \phi_{gd}] \quad 6.35$$

6.1.2 Aerodynamic drag

Components of perturbations due to aerodynamic drag are given by

$$[\Delta_{D_r} \quad \Delta_{D_s} \quad \Delta_{D_w}]^T = \frac{1}{2} \rho S C_D v [v_r \quad v_s \quad 0]^T \quad 6.36$$

where

ρ = atmospheric density

S = aerodynamic reference area

C_D = drag coefficient

v = velocity magnitude

$$v_r = \sqrt{\frac{\mu}{p}} (f \sin(L) - g \cos(L))$$

$$v_s = \sqrt{\frac{\mu}{p}} (1 + f \cos(L) - g \sin(L))$$

6.1.3 Thrust acceleration

The second major perturbation is the thrust acceleration defined by

$$\mathbf{a}_T = \frac{T}{m} \mathbf{u}$$

where T is the thrust, m is the spacecraft mass and $\mathbf{u} = [u_r \quad u_s \quad u_w]^T$ is unit pointing thrust vector expressed in RSW frame. The components of the unit thrust vector can be also defined in spherical coordinates as follow:

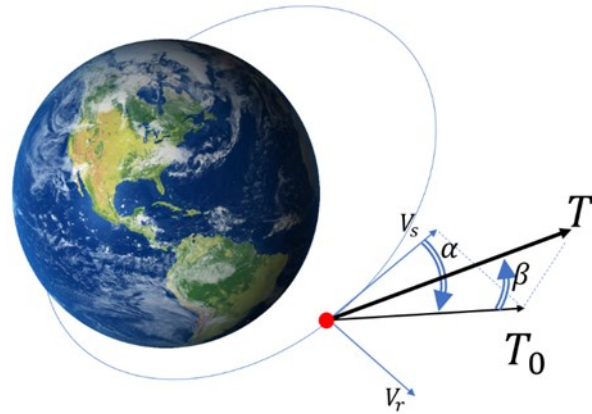


Figure 34. Thrust pointing angles

$$u_r = \cos \alpha \sin \beta \quad 6.37$$

$$u_s = \cos \alpha \cos \beta \quad 6.38$$

$$u_w = \sin \beta \quad 6.39$$

Finally, the transformation to the modified equinoctial elements system from ECI system is given by

$$\mathbf{u}_{T_{RSW}} = Q_r^T \mathbf{u}_{T_{ECI}} \quad 6.40$$

For this optimisation, a polynomial approach is utilized to create a parametrization of the control time history. To optimise a minimum fuel continuous thrust trajectory, the ignition time is correlated to the amount of fuel spent during the manoeuvre. Thereby, the optimality of the trajectory depends on the ignition time and on the thrust pointing angle. The thrust vector may vary during the flight to provide more flexibility in the optimisation process. In our case of continuous thrust, the parameters to be optimised are the manoeuvring time and the thrust vector. The thrust vector is defined by two angles α and β . The angle α is defined between the direction of the velocity vector and the projection of the thrust vector on the orbital plane; β is the angle defining the out-of-plane component.

The angle α is measured clockwise from the local horizon and β is measured from T to T_0 where T_0 is the projection of T on the orbit plane (see figure Figure 34). Following the dynamics of the two-body problem the equation of motion can be described as

$$\ddot{\mathbf{r}} + \frac{\mu}{r^3} \mathbf{r} = \mathbf{a}_d$$

where \mathbf{a}_d are the disturbing accelerations. This term is the sum of orbital perturbations (due to the oblateness of the Earth) if included and the propulsive thrust: as a matter of fact, it is little and can be considered as a perturbation. If the spacecraft is assumed to provide a constant thrust, like in our case, but not constant acceleration, the thrust to mass ratio can be written as follow

$$\frac{T}{m} = \frac{cn_0}{c - n_0 t} \quad 6.41$$

where c is the exhaust gas velocity, n_0 is the thrust to mass ratio at the initial time. The relation for c is the following

$$c = I_{sp} * g_0 \quad 6.42$$

with g_0 gravity acceleration of the Earth.

Because of the variable mass due to the fuel consumption, constant acceleration cannot be assumed, although for electric propulsor it is so little that can be neglected.

To include out-of-plane motion different state-space representations are adopted. We will use the modified equinoctial elements that, compared to Gaussian variational equations, avoid singularities for null parameters.

The acceleration components point to the radial and out-of-plane direction. The acceleration due to the thrust is given by

$$\mathbf{a}_{thrust} = \frac{T}{m} \begin{Bmatrix} \sin(\alpha) \cos(\beta) \\ \cos(\alpha) \cos(\beta) \\ \sin(\beta) \end{Bmatrix} \quad 6.43$$

Adopting these angles both in-plane and out-of-plane contributions are included.

Considering only the J_2 spherical harmonic [39], disturbing acceleration can be expressed as follow:

$$\mathbf{a}_{J_2} = \begin{Bmatrix} f_r \\ f_s \\ f_w \end{Bmatrix} = \begin{Bmatrix} -\frac{3\mu J_2 R_\oplus^2}{2r^4} \left(1 - 12 \frac{[h \sin(L) - k \cos(L)]^2}{s^4} \right) \\ -\frac{12\mu J_2 R_\oplus^2}{r^4} \frac{[h \sin(L) - k \cos(L)][h \cos(L) + k \sin(L)]}{s^4} \\ -\frac{6\mu J_2 R_\oplus^2}{r^4} \frac{[h \sin(L) - k \cos(L)][1 - k^2 - h^2]}{s^4} \end{Bmatrix} \quad 6.44$$

The control time history is parametrized with shape functions. For this application polynomial shape functions have been chosen. It is possible to express the control angles as

$$\alpha = a_0 + \sum_{i=1}^6 a_i \left(\frac{t}{t_f} \right)^i \quad 6.45$$

$$\beta = b_0 + \sum_{i=1}^6 b_i \left(\frac{t}{t_f} \right)^i \quad 6.46$$

where a_i and b_i are the control parameters which modify the control time history. Choosing these shape function there are 15 control variables, the time t , a_i and b_i .

6.1.4 Cost function definition for the orbital manoeuvre

Many different classifications can be generally made to divide optimisation methods. Two fundamental categories could be highlighted in parameter optimisation and functional optimisation. The first, better known as optimal design, has parameters not depending on time and the problem is solved in a finite dimension; the functional optimisation, known as optimal control theory, some parameters are time-dependent and the problem is not defined in a finite dimension: in this case the function to be minimised is called

functional. A further categorisation can be made between *direct* and *indirect* methods. Indirect methods capitalise on the optimality criteria (Karush-Kuhn-Tucker conditions) to find optimal solutions, while direct methods start with some initial guesses, searching iteratively for the solution in the space domain. In our case, a direct method generates an optimal solution. The purpose of the optimisation is to reach the optimal solution in the shortest time. In this section, the definition of the cost function for trajectory and attitude manoeuvre will be discussed independently.

In the case of the trajectory optimisation the satellite has to reach the final orbit in the shortest time. Since time of propulsion is strictly correlated to available fuel, a minor time of propulsion translates in less exhaust fuel and so more time to extend the entire mission. Proven how time and fuel are strictly related, the cost function related to the minimum fuel consumption is

$$J = c_w \frac{w_0}{w_f} \tag{6.47}$$

where c_w is a user-defined coefficient, w_0 and w_f are the initial and final weights respectively. Initial, transfer and final orbit are defined by equinoctial elements. They correspond for initial and transfer orbits at the initial time, for final and transfer orbits at the final time. Thus, the equality constraints can be expressed as

$$\boldsymbol{\phi} = \begin{Bmatrix} p(t_f) - p_f \\ f(t_f) - f_f \\ g(t_f) - g_f \\ h(t_f) - h_f \\ k(t_f) - k_f \end{Bmatrix} = \mathbf{0} \tag{6.48}$$

The subscript f indicates the final expected value at the end of the manoeuvre while (t_f) indicates the actual value. To have a dimensionless form, equality constraints can be divided for their initial value. A technique to augment the velocity of convergence consists in squaring those constraints, multiplying for a coefficient to reduce them at the same order of magnitude. The final cost function is then expressed as

$$J = c_w \frac{w_0}{w_f} + c_p \left[\frac{p(t_f) - p_f}{p_i} \right]^2 + c_f \left[\frac{f(t_f) - f_f}{f_i} \right]^2 + c_g \left[\frac{g(t_f) - g_f}{g_i} \right]^2 + c_h \left[\frac{h(t_f) - h_f}{h_i} \right]^2 + c_k \left[\frac{k(t_f) - k_f}{k_i} \right]^2 \quad 6.49$$

6.2 Attitude reorientation optimisation model

The fundamental requirement of an on-board attitude optimisation software is its capacity to calculate the optimal trajectory in a reasonable timeframe. A PS method is sensitive to the initial condition: the more the initial guesses are far from the optimised trajectory the more the calculation time will be. It has been demonstrated that without appropriate initial conditions, it could take up to 1400 s (~ 23 min) to calculate the optimal solution [34], an unacceptable time for autonomous satellites. Using the PSO it is possible to reduce the computational time without providing any initial condition. The basic idea provided in ref. [40] consists in a parametrization of the attitude trajectory using B-splines, an optimisation to meet constraints and then through a proceed of inverse dynamics the calculation of angular velocities and control torques. The approach used in this thesis follows the one used in [40] but using Bézier curves instead of B-splines for their relative ease to compute. Bézier curves are defined in a virtual time domain defined between 0 and 1. It will be necessary a mapping function to express quaternions in the

actual time. Constraints on control torque and angular velocities can be satisfied changing the mapping function.

6.2.1 Attitude path based on Bézier curves

In computer graphics Bézier curves are used to construct position curves. These curves are parametric curves of $n + 1$ control points, where n indicates the order of the curve, expressed as

$$\bar{b}(\tau) = \sum_{i=0}^n \beta_{i,n}(\tau) \bar{p}_i \quad (0 \leq \tau \leq 1) \quad 6.50$$

where \bar{p}_i s are the control points ($i = 0, \dots, n$), τ is the control variable of the curve varying from 0 to 1 corresponding to the initial and final point, $\beta_{i,n}$ is the Bernstein basis defined as

$$\beta_{i,n}(\tau) = \binom{n}{i} (1 - \tau)^{n-i} \tau^i \quad 6.51$$

where the term $\binom{n}{i}$ indicates the binomial coefficient defined as

$$\binom{n}{i} = \frac{n!}{i!(n-i)!} \quad 6.52$$

The attitude path will be modelled using Bézier quaternion curves, that can be seen as Bézier curves with unit quaternions as control points. In this work control points are defined using the Modified Rodrigues Parameters [41, 42].

6.2.2 Modified Rodrigues Parameters

MRP are defined in this sub-paragraph. Given a quaternion $\mathbf{q} = [q_0 \ \mathbf{q}_v]$, where q_0 is the scalar component and \mathbf{q}_v the vector component, it is possible to define

$$\mathbf{p} = \frac{\mathbf{q}_v}{1 + q_0} = \mathbf{e} \tan\left(\frac{\phi}{4}\right) \quad 6.53$$

where \mathbf{e} is the rotation axis and ϕ the rotation angle. The inverse transformation is given by

$$q_0 = \frac{1 - p^2}{1 + p^2} \quad \text{and} \quad \mathbf{q}_v = \frac{2\mathbf{p}}{1 + p^2} \quad 6.54$$

with $p^2 = \mathbf{p}^T \mathbf{p}$.

The type of manoeuvre is *rest-to-rest*: we consider the satellite with null initial and final angular velocity and accelerations. To impose this constraint, the first and second derivative of Bézier curve needs to be analysed. It is important to adopt curves with differentiability class C^4 to have smooth and continuous second derivatives, as the angular acceleration. Because of a *rest-to-rest* manoeuvre, it is necessary to set just the first and the last control point. If the angular velocity is null, then the MRP are null. We can impose this condition

$$\mathbf{p}_0 = \mathbf{p}_1 \quad \text{and} \quad \mathbf{p}_{n-1} = \mathbf{p}_n \quad 6.55$$

A Bézier curve of grade n is defined with $n+1$ control points. A fifth-order curve is defined with 6 control points: four of them are defined, two of them are used to optimise the trajectory.

$$\begin{aligned} \mathbf{p}^5(\tau) = & \mathbf{p}_0(1 - \tau)^5 + 5\mathbf{p}_1\tau(1 - \tau)^4 + 10\mathbf{p}_2\tau^2(1 - \tau)^3 + 10\mathbf{p}_3\tau^3(1 - \tau)^2 \\ & + 5\mathbf{p}_4\tau^4(1 - \tau) + \mathbf{p}_5\tau^5 \end{aligned} \quad 6.56$$

Starting from the previous equation, it is possible to calculate analytically the first and second derivative.

Imposing the previous constraints to obtain initial and final angular velocities and acceleration, for a fifth order Bézier curve all the control points are determined; in this case to optimise the trajectory a higher degree must be chosen. Let us suppose an order 6th order Bézier curve.

$$\begin{aligned} \mathbf{p}^6(\tau) = & \mathbf{p}_0(1 - \tau)^6 + 6\mathbf{p}_1\tau(1 - \tau)^5 + 15\mathbf{p}_2\tau^2(1 - \tau)^4 + 20\mathbf{p}_3\tau^3(1 - \tau)^3 \\ & + 15\mathbf{p}_4\tau^4(1 - \tau)^2 + \mathbf{p}_5\tau^5(1 - \tau) + \mathbf{p}_6\tau^6 \end{aligned} \quad 6.57$$

Imposing the first and second derivative for $\tau = 0$ and $\tau = 1$ we obtain a constraint on some control points

$$\begin{aligned} \boldsymbol{\omega}(t = 0) = 0 & & \mathbf{p}_1 = \mathbf{p}_0 \\ \boldsymbol{\omega}(t = 1) = 0 & & \mathbf{p}_5 = 6\mathbf{p}_6 \\ \dot{\boldsymbol{\omega}}(t = 0) = 0 & & \mathbf{p}_2 = \mathbf{p}_0 \\ \dot{\boldsymbol{\omega}}(t = 1) = 0 & & \mathbf{p}_4 = \mathbf{p}_6 \end{aligned} \quad 6.58$$

Considering this curve only one “free” control point is available to modify the curve. There will be two control points available for optimisation adopting a curve of seventh order

$$\begin{aligned} \mathbf{p}^7(\tau) = & \mathbf{p}_0(1 - \tau)^7 + 7\mathbf{p}_1\tau(1 - \tau)^6 + 21\mathbf{p}_2\tau^2(1 - \tau)^5 + 35\mathbf{p}_3\tau^3(1 - \tau)^4 \\ & + 35\mathbf{p}_4\tau^4(1 - \tau)^3 + \mathbf{p}_5\tau^5(1 - \tau)^2 + \mathbf{p}_6\tau^6(1 - \tau) + \mathbf{p}_7\tau^7 \end{aligned} \quad 6.59$$

And the constraints will be as follow:

$$\begin{aligned} \boldsymbol{\omega}(t = 0) = 0 & & \mathbf{p}_1 = \mathbf{p}_0 - \mathbf{p}_7 \\ \boldsymbol{\omega}(t = 1) = 0 & & \mathbf{p}_6 = \mathbf{p}_7 \\ \dot{\boldsymbol{\omega}}(t = 0) = 0 & & \mathbf{p}_2 = \mathbf{p}_0 - \frac{35}{21}\mathbf{p}_7 \\ \dot{\boldsymbol{\omega}}(t = 1) = 0 & & \mathbf{p}_5 = -14\mathbf{p}_7 \end{aligned} \quad 6.60$$

The following table summarise the previous constraints.

Curve order	$\mathbf{t} = 0$		$\mathbf{t} = 1$		
	$\boldsymbol{\omega} = 0$	$\dot{\boldsymbol{\omega}} = 0$	$\boldsymbol{\omega} = 0$	$\dot{\boldsymbol{\omega}} = 0$	Free control points
5	$\mathbf{p}_1 = \mathbf{p}_0$	$\mathbf{p}_2 = \mathbf{p}_0$	$\mathbf{p}_4 = \mathbf{p}_5$	$\mathbf{p}_3 = \mathbf{p}_5$	none
6	$\mathbf{p}_1 = \mathbf{p}_0$	$\mathbf{p}_2 = \mathbf{p}_0$	$\mathbf{p}_5 = 6\mathbf{p}_6$	$\mathbf{p}_4 = \mathbf{p}_6$	\mathbf{p}_3
7	$\mathbf{p}_1 = \mathbf{p}_0 - \mathbf{p}_7$	$\mathbf{p}_2 = \mathbf{p}_0 - \frac{35}{21}\mathbf{p}_7$	$\mathbf{p}_6 = \mathbf{p}_7$	$\mathbf{p}_5 = -14\mathbf{p}_7$	$\mathbf{p}_3, \mathbf{p}_4$

Table 11. Control points determination for constraints on angular velocity and acceleration

The rotation matrix using RPM is

$$R(\mathbf{p}) = I + \frac{4(1 - |\mathbf{p}|^2)}{(1 + |\mathbf{p}|^2)^2} [\tilde{\mathbf{p}}] + \frac{8}{(1 + |\mathbf{p}|^2)^2} [\tilde{\mathbf{p}}]^2 \quad 6.61$$

where the matrix $[\tilde{\mathbf{p}}]$ is defined as

$$[\tilde{\mathbf{p}}] = \begin{bmatrix} 0 & p_3 & -p_2 \\ -p_3 & 0 & p_1 \\ p_2 & -p_1 & 0 \end{bmatrix} \quad 6.62$$

so, a rotation can be expressed as

$$\mathbf{p}(t) = R(\mathbf{p})^T \mathbf{p}(t_0) \quad 6.63$$

The derivative of the RMP are linked to angular velocities through

$$\dot{\mathbf{p}} = \frac{1}{4} \Psi(\mathbf{p}) \boldsymbol{\omega} \quad 6.64$$

where the matrix $\Psi(\mathbf{p})$ is

$$\Psi(\mathbf{p}) = [(1 - \mathbf{p}^T \mathbf{p})I + 2[\tilde{\mathbf{p}}] + 2\mathbf{p}\mathbf{p}^T] \quad 6.65$$

For the development of inverse dynamics, angular velocity and acceleration need to be expressed in function of \mathbf{p} and $\dot{\mathbf{p}}$.

$$\boldsymbol{\omega} = 4\Psi^{-1}(\mathbf{p})\dot{\mathbf{p}} \quad 6.66$$

The inverse of Ψ is a near-orthogonal matrix because its inverse is proportional to its transpose; so, we have

$$\Psi^{-1}(\mathbf{p}) = \frac{\Psi^T(\mathbf{p})}{(1 + \mathbf{p}^T \mathbf{p})^2} \quad 6.67$$

From the previous equations an important consequence is that if the angular velocity is null, then $\dot{\mathbf{p}} = 0$. The angular acceleration is obtained by

$$\dot{\boldsymbol{\omega}} = 4(\dot{\Psi}^{-1}(\mathbf{p})\dot{\mathbf{p}} + \Psi^{-1}(\mathbf{p})\ddot{\mathbf{p}}) \quad 6.68$$

where $\dot{\Psi}$ and $\dot{\Psi}^{-1}$ are

$$\dot{\Psi}^{-1} = \frac{\dot{\Psi}^T}{(1 + \mathbf{p}^T \mathbf{p})^2} - \frac{2\Psi^T}{(1 + \mathbf{p}^T \mathbf{p})^3}(\dot{\mathbf{p}}\mathbf{p}^T + \mathbf{p}^T \dot{\mathbf{p}}) \quad 6.69$$

The advantage of these equation is the possibility to fully describe the attitude kinematics using the MRP. So, we have a mathematical formulation to express the torque as a function of the MRP.

$$\mathbf{M} = f(\mathbf{p}, \dot{\mathbf{p}}, \ddot{\mathbf{p}}) \quad 6.70$$

6.2.3 The time mapping function

A proper mapping function needs to be chosen to map the virtual domain τ to the time domain t . Different time mapping functions can be chosen, but since we need only a feasible trajectory, we choose the simplest linear mapping function

$$\frac{d\tau}{dt} = c \quad 6.71$$

where c is a constant parameter used to adjust the angular velocity along the attitude path. While the time t varies from 0 to t_f the virtual time τ varies from 0 to 1. With the time mapping it is possible to convert the attitude path $\mathbf{q}(\tau)$ in $\mathbf{q}(t)$. Adjusting the parameter c it is possible to achieve different final time for the reorientation manoeuvre.

$$\int_0^{t_f} dt = t_f = \int_0^1 \frac{1}{c} d\tau = \frac{1}{c} \quad 6.72$$

6.2.4 Inverse dynamics

To obtain the angular velocities and the control torque we apply the inverse dynamics.

Starting from the value of \mathbf{p} we have

$$\dot{\mathbf{p}} = \frac{d\mathbf{p}}{dt} = \frac{d\mathbf{p}}{d\tau} \frac{d\tau}{dt} = \frac{d\mathbf{p}}{d\tau} c \quad 6.73$$

$$\ddot{\mathbf{p}} = \frac{d^2\mathbf{p}}{dt^2} = \frac{d}{dt} \left(\frac{d\mathbf{p}}{d\tau} \right) = \frac{d^2\mathbf{p}}{d\tau^2} \frac{d\tau}{dt} + \frac{d\mathbf{p}}{d\tau} \frac{d^2\tau}{dt^2} \quad 6.74$$

If the mapping function is constant

$$\ddot{\mathbf{p}} = \frac{d^2\mathbf{p}}{dt^2} = \frac{d^2\mathbf{p}}{d\tau^2} \frac{d\tau}{dt} = \frac{d^2\mathbf{p}}{d\tau^2} c \quad 6.75$$

6.2.5 Disturbing torques

Two main disturbing torques are analysed in the attitude reorientation manoeuvre. Effects due to the solar radiation pressure are included, discerning a case in umbra and the case in which the satellite is in the sunlight; the other disturbing torque is due to the effects of atmospheric drag during the manoeuvre.

6.2.5.1 Solar radiation pressure disturbing torque

As in the previous case a cone for attitude forbidden zone can be defined. In this case the main complexity is to determine the direction of the Sun along the orbit motion. Using a Sun almanac [43] it is possible to determine penumbra and umbra shadow regions using low precision formula to determine Sun coordinates in equatorial rectangular coordinates.

The definition of the shadow region can be accomplished using the hypothesis that celestial bodies are perfectly round [33]: that assumption allows to define two conical shadow regions.

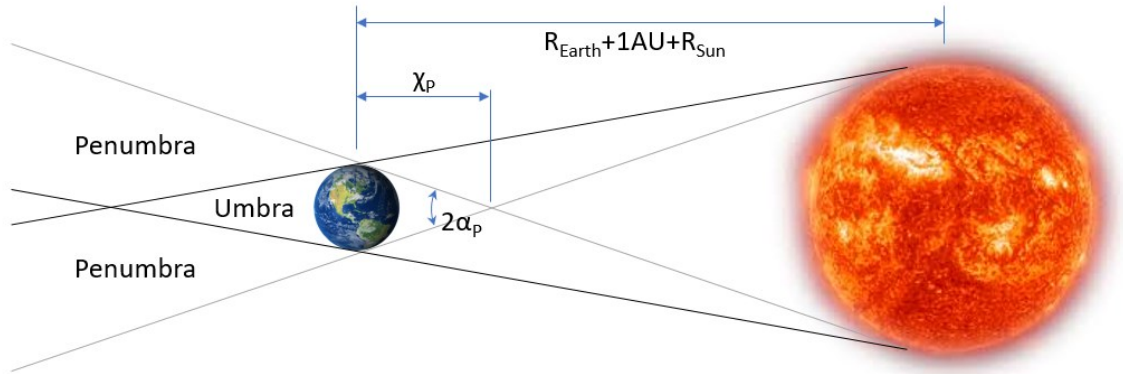


Figure 35. Umbra and penumbra region

Let us define $d_P = R_{Earth} + 1AU + R_{Sun}$. The distance χ_P is

$$\chi_P = \frac{R_E d_P}{R_E + R_S} \quad 6.76$$

and the angle α_P

$$\alpha_P \approx \arcsin\left(\frac{R_E}{\chi_P}\right) \quad 6.77$$

In this study the spacecraft position vector is considered in ECI system. The solar unit vector is

$$\hat{\mathbf{s}} = \frac{\mathbf{s}}{|\mathbf{s}|}$$

It is used to compute the projection of the spacecraft along $\hat{\mathbf{s}}$, defined

$$\mathbf{r}_p = (\mathbf{r} \cdot \hat{\mathbf{s}})\hat{\mathbf{s}} \quad 6.78$$

The distance between the axis of the penumbra cone and the spacecraft is defined by the difference of vectors

$$\boldsymbol{\delta} = \mathbf{r} - \mathbf{r}_p \quad 6.79$$

and the distance between the centre of the penumbra cone axis and the penumbra termination point at the projected spacecraft location is

$$k_p = (\chi_p + |\mathbf{r}_p|) \tan \alpha_p \quad 6.80$$

Two cases are now possible:

1. Shadow termination points are possible if $(\mathbf{r} \cdot \hat{\mathbf{s}}) < 0$. If $|\boldsymbol{\delta}| > k_p$ the spacecraft is still in sunlight
2. If $|\boldsymbol{\delta}| = k_p$ there are penumbra termination points and the spacecraft is in the penumbra cone if $|\boldsymbol{\delta}| < k_p$

In the case of umbra cone it is possible to proceed in analogous way of the penumbra cone.

$$\sin \sigma = \frac{R_{Sun}}{d_p + \chi_U} \quad 6.81$$

$$\chi_U \tan \sigma \approx R_{Earth} \quad 6.82$$

Where χ_U is the distance from the centre of the Earth and the apex of the shadow cone. Solving numerically these equations together we find $\sigma = 0.26412^\circ$ and $\chi_U = 1.3836 \cdot 10^6$ km.

In a similar way for penumbra cone we can define the entry and exit in the umbra cone. Let us define, as in the previous case for umbra cone, the parameter

$$k_U = (\chi_U + |\mathbf{r}_P|) \tan \sigma \quad 6.83$$

Two cases are now possible:

1. Umbra termination points are possible if $(\mathbf{r} \cdot \hat{\mathbf{s}}) < 0$. If $|\delta| > k_U$ the spacecraft is still in penumbra or sunlight
2. If $|\delta| = k_U$ there are umbra termination points and the spacecraft is in the umbra cone if $|\delta| < k_U$

Because of the short duration in the penumbra zone, we will consider the umbra zone starting from the penumbra cone, assuming solar rays are not present in the penumbra zone.

Disturbance effects due to solar radiation pressure could be neglected in a first approximation for orbit perturbation, however, it can have an important impact on attitude reorientation. The mean value for solar radiation pressure has been quantified as

$$p_{\odot} = 9.08 \cdot 10^{-6} \text{ N}$$

The disturbance torque can be estimated as

$$M_{srp}^x = p_{\odot} S \cos \eta d_z \quad 6.84$$

$$M_{srp}^y = p_{\odot} S \cos \eta d_x \quad 6.85$$

$$M_{srp}^z = p_{\odot} S \cos \eta d_y \quad 6.86$$

where η is the angle between the normal vector to the solar panel and the vector in the direction of the Sun and $\mathbf{d}^T = [d_x \quad d_y \quad d_z]$ is the vector defining

the position of the solar panel centre of mass with respect to the satellite centre of mass.

6.2.5.2 Atmospheric drag disturbing torque

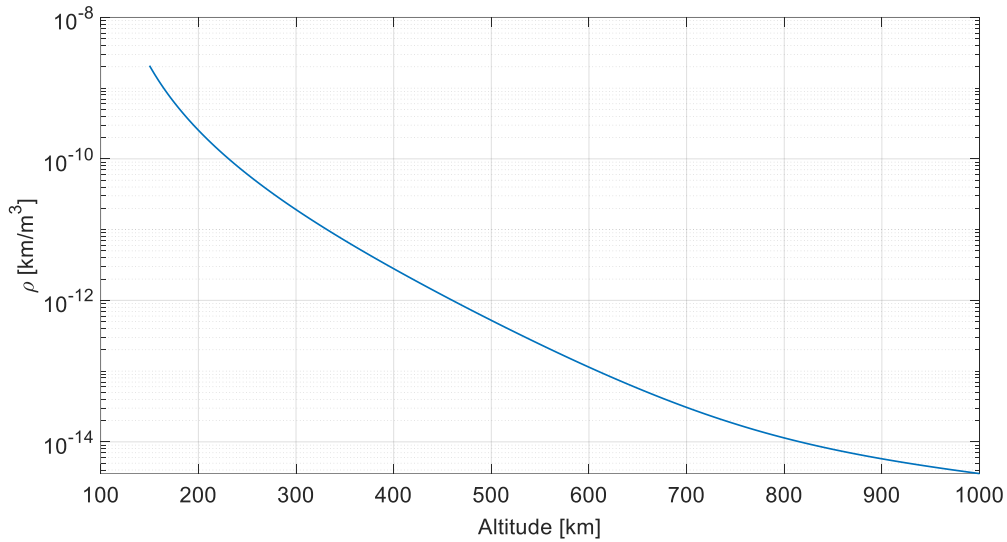


Figure 36. Atmospheric density model

Atmospheric drag gives a contribution to disturbance torques during a reorientation manoeuvre. Its effects are perceptible at low altitudes where it is denser. A model for atmosphere density is reported in ref. [44].

We can express the drag as

$$D_{drag} = \frac{1}{2} \rho S c_d V^2 \quad 6.87$$

where ρ is the atmospheric density [kg/m³], S is the surface [m²] considered for the drag (only the solar panel surface is taken into account), c_d is the drag coefficient (assumed to be 2.2), V is the velocity [m/s] of the spacecraft with respect to the atmosphere (atmosphere assumed to be firm, this is the velocity of the satellite). For the attitude, the RSW frame is used as fixed frame. In

this frame and under the previous assumption the velocity vector is quasi-coincident with the \hat{s} axis and there is a component along \hat{r} due to the flight path angle φ :

$$V_r = V \sin \varphi$$

$$V_s = V \cos \varphi$$

$$V_w = 0$$

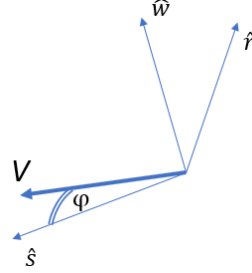


Figure 37. Velocity vector and flight path angle

We can calculate the disturbance torque due to this drag as

$$M_{drag}^x = \frac{1}{2} \rho S \cos(\vartheta) c_d V^2 d_z \quad 6.88$$

$$M_{drag}^y = \frac{1}{2} \rho S \cos(\vartheta) c_d V^2 d_x \quad 6.89$$

$$M_{drag}^z = \frac{1}{2} \rho S \cos(\vartheta) c_d V^2 d_y \quad 6.90$$

where ϑ is the angle between the velocity vector and the normal vector to the surface of the solar panel, d_x , d_y , d_z are the distance of centre of mass of the solar panel with respect to the centre of mass of the entire satellite.

6.2.6 Attitude reorientation geometrical constraints

For attitude reorientation two geometrical constraints are imposed, defined as *keep-out* cones, at which the IR-camera must not point. A criterion to impose this condition [35] is illustrated below.

Let us suppose that in its motion along the orbit the fixed frame is RSW, where \mathbf{r} is the versor in the radial direction between Earth and satellite, \mathbf{s} is the normal versor to the orbital plane and $\mathbf{w} = \mathbf{s} \otimes \mathbf{r}$.

Here it is defined the attitude forbidden zone as the set of attitudes which the spacecraft is required to avoid during the reorientation manoeuvre.

In this particular case, it is not allowed to point towards bright objects. In the following figure, there is an example of the forbidden zone towards the Earth. In the figure it is denoted O the centre of mass of the spacecraft, $-\mathbf{r}$ is the vector opposite to the radial versor and pointing from the spacecraft to the Earth, \mathbf{x} is the boresight vector of the instrument expressed in the body frame, θ is the actual angle between $-\mathbf{r}$ and \mathbf{x} and θ_F is the cone angle which defines the forbidden zone.

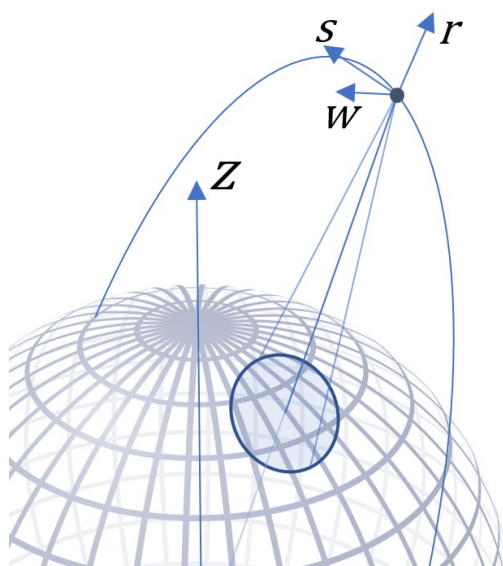


Figure 38. RSW frame

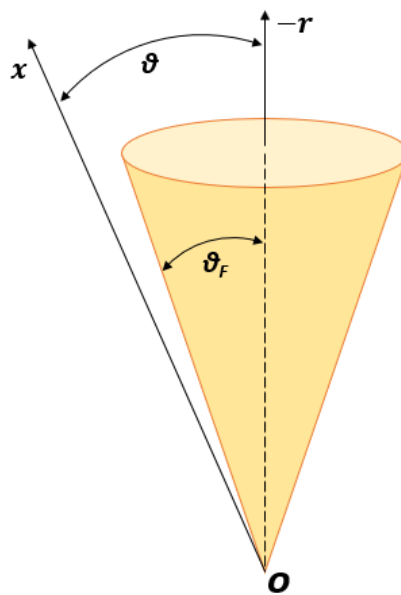


Figure 39. Attitude forbidden zone

The requirement that the boresight vector stays outside the forbidden cone can be expressed as

$$-\mathbf{r}^T \mathbf{x}' - \cos(\theta_F) < 0 \quad 6.91$$

where \mathbf{x}' is the vector of the bright object expressed in the inertial frame and can be calculated as

$$\begin{bmatrix} 0 \\ \mathbf{x}' \end{bmatrix} = \mathbf{q} \otimes \begin{bmatrix} 0 \\ \mathbf{x} \end{bmatrix} \otimes \mathbf{q}^*$$

with \mathbf{q} the quaternion expressing the attitude with respect to the inertial frame and \mathbf{q}^* the conjugate quaternion. The requirement of the attitude forbidden zone can be rewritten as

$$\mathbf{q}^T M_F \mathbf{q} < 0$$

where M_F is

$$M_F = \begin{bmatrix} d & b^T \\ b & A \end{bmatrix} \quad 6.92$$

With

$$\begin{aligned} d &= -\mathbf{r}^T \mathbf{x}' - \cos(\theta_F), \quad b = \mathbf{x}' \times (-\mathbf{r}), \\ A &= -\mathbf{r} \mathbf{x}'^T + \mathbf{x}' (-\mathbf{r})^T - (-\mathbf{r}^T \mathbf{x}' + \cos(\theta_F)) I_{3 \times 3} \end{aligned} \quad 6.93$$

$I_{3 \times 3}$ identity matrix.

In a similar way an attitude mandatory zone can be defined used the following equation

$$\mathbf{q}^T M_M \mathbf{q} > 0 \quad 6.94$$

With the matrix M_M expressing the mandatory zone. M_M has the same form of M_F and θ_F is replaced by θ_M . It is useful to define a mandatory zone in the optimisation to model the error tolerances given by the instruments.

6.2.7 Cost function definition for attitude reorientation manoeuvre

In the same fashion of trajectory optimisation, also for attitude the main purpose is to obtain the shortest manoeuvre in time. Compared to the

previous case, the cost function will be defined considering inequality constraints. Reaction wheels mounted on the satellite can provide a maximum torque. This maximum torque represents a constraint expressible using inequalities. An approach to insert these inequalities in the cost function consists on the introduction of a penalty function [40] depending on the type of constraint. It can be summarised as

$$G_i = c_i \sum_{j=0}^n v_i(t_j) \quad 6.95$$

where c_i are constants defined by the user. For path constraint

$$v_i(t_j) = \begin{cases} 0 & \text{if } \mathbf{q}^T(t_j)M_F\mathbf{q}(t_j) < 0 \\ 1 & \text{otherwise} \end{cases} \quad 6.96$$

This condition represents the inequalities for the keep-out cone for bright objects. For control constraint

$$v_i(t_j) = \begin{cases} 0 & \text{if } |\mathbf{M}_i(t_j)| < \mathbf{M}_{max} \\ 1 & \text{otherwise} \end{cases} \quad 6.97$$

This constraint allows not to exceed the maximum torque. The cost function for the attitude manoeuvre is then

$$J = c_t t_f + \sum_{i=1}^{N_{ineq}} G_i \quad 6.98$$

In the end the inequalities are imposed by the keep-out cones and the maximum torque.

$$\mathbf{q}^T(t_j)M_F\mathbf{q}(t_j) < 0 \quad 6.99$$

$$|\mathbf{M}_i(t_j)| < \mathbf{M}_{max} \quad 6.100$$

6.3 Collision avoidance analysis

The development of the space industry has raised new challenges for space missions in the latest years. Nowadays one of the main concerns for satellites in LEO orbits is avoiding collisions, especially with debris. It has been counted by European Space Agency (ESA) the presence of 34000 objects larger than 10 cm, 900000 objects between 1 and 10 cm, 128 million objects between 1 mm to 1 cm, for a total mass of 84000 tons of orbiting objects in LEO [45]. About 24% of those objects are satellites, about 18% are rocket parts. The presence of these bodies threatens the possibility to continue a space mission, the reason why is essential avoiding collisions. Moreover, when a collision occurs new debris are generated.

In this chapter, a method for debris collision avoidance is shown, according to the presented mission.

6.3.1 Methods and models adopted for collision avoidance

Dealing with non-Gaussian distributions is open research in the space field. To implement a proper manoeuvre, the covariance needs to represent the real uncertainty. Up to date, all the processes to calculate the uncertainty assume that the uncertainty is Gaussian. A method to determine when the uncertainty become non-Gaussian is the Cramer-Von Mises metric (CMV) [46, 47]. This method uses the Mahalanobis distance and is statistically rigorous. The Mahalanobis distance (MD) is defined as

$$MD = (\mathbf{x} - \mathbf{x}_{truth})^T P^{-1} (\mathbf{x} - \mathbf{x}_{truth}) \quad 6.101$$

where \mathbf{x} is the state and P the covariance matrix. The Mahalanobis distance gives a probability that the uncertainty is Gaussian.

In this chapter, the uncertainty is propagated using a linearized method. We will consider the satellite as the primary object (p), the debris as the secondary object (s). The linearized model [47] stands under the following assumptions:

- Gaussian probability distribution function can express the uncertainty
- A linearized model can approximate the dynamics of neighbouring trajectories with respect to a nominal trajectory
- The uncertainty in velocity is negligible
- The uncertainty in position of the objects is constant during the encounter
- The relative motion can be considered rectilinear for a short encounter

The last two assumptions are valid if the duration of the approach is short (< 500 s) or if the relative velocity is high (> 10 m/s).

Debris, which are the secondary bodies, could be generally tracked from space-based platforms or ground-based radars. Radar tracking error model is developed using an appropriate frame.

The radar accuracy is affected by different error source: Signal-to-Noise ratio, noise sources in the final stages of the radar receiver, bias errors due to the radar calibration, interference sources. We characterise the radar accuracy with the standard deviation of the Gaussian distribution. This is an appropriate approach for several cases of interests.

Radar performances are measured through the Signal to Noise Ratio (SNR), ratio between the signal power to noise power at the output of the radar receiver

$$SNR = \frac{P_r}{P_n} = \frac{P_p G_t \sigma A_r \tau}{(4\pi)^2 R^4 k F T_0 L} \quad 6.102$$

where the parameters defining the SNR are

P_p transmitted power [W]

G_t radar transmit antenna gain

σ target radar cross section (RCS) [m²]

A_r effective aperture area of the radar receiving antenna [m²]

τ radar pulse duration [s]

F noise figure of the receiver subsystem

T_0 standard temperature [290 K]

L system losses

k Boltzmann constant [1.38064852 · 10⁻²³ m² kg s⁻² K⁻¹]

Target information is measured in spherical coordinates by radars, in terms of range, elevation and azimuth ($r_{RDR}, \eta_{RDR}, \varepsilon_{RDR}$). Each measurement is source of uncertainty.

$$\sigma_{r_{RDR}}^2 = \sigma_{RN}^2 + \sigma_{RF}^2 + \sigma_{RB}^2 \quad 6.103$$

where σ_{RN} is a SNR range dependent error, which can be calculated as

$$\sigma_{RN} = \frac{c}{2B\sqrt{2SNR}} \quad 6.104$$

where B is the waveform bandwidth, c the speed of light.

σ_{RF} is an error due to the noise in the latter stage of the radar receiver, σ_{RB} is a bias error due to radar calibration and measurement process. We assume the a zero-mean condition, so σ_{RF} and σ_{RB} , respectively a random error with fixed standard deviation and a range bias error, are zero.

It is possible to express errors for angular measurements as

$$\begin{aligned}\sigma_{\epsilon_{RDR}}^2 &= \sigma_{AN_\epsilon}^2 + \sigma_{AF_\epsilon}^2 + \sigma_{AB_\epsilon}^2 \\ \sigma_{\eta_{RDR}}^2 &= \sigma_{AN_\eta}^2 + \sigma_{AF_\eta}^2 + \sigma_{AB_\eta}^2\end{aligned}\tag{6.105}$$

where, as the range error, σ_{AN} is a SNR dependent error

$$\sigma_{AN} = \frac{\vartheta}{k_m \sqrt{2SNR}}\tag{6.106}$$

with ϑ is the radar beamwidth in the angular coordinates and k_m is the monopulse pattern difference slope. We assume null angular bias and random measurement error for range and angular errors under the zero-mean condition hypothesis. The radar is positioned in the South-East-Zenith (SEZ) frame. This is defined for a given latitude and longitude and rotates with the site. The $\hat{\mathbf{S}}$ axis points to the south from the site, the $\hat{\mathbf{E}}$ axis to the east, the $\hat{\mathbf{Z}}$ axis to the zenith from the location. From ECI frame it is defined as

$$\begin{aligned}\hat{\mathbf{Z}} &= \frac{\bar{\mathbf{r}}_{SITE}}{|\bar{\mathbf{r}}_{SITE}|} \\ \hat{\mathbf{E}} &= \hat{\mathbf{K}} \times \hat{\mathbf{Z}} \\ \hat{\mathbf{S}} &= \hat{\mathbf{E}} \times \hat{\mathbf{Z}}\end{aligned}\tag{6.107}$$

The transfer matrix between SEZ and ECI frame is

$$\begin{aligned}M_{SEZ \rightarrow ECI} &= [\hat{\mathbf{S}} \quad \hat{\mathbf{E}} \quad \hat{\mathbf{Z}}] \\ M_{ECI \rightarrow SEZ} &= [\hat{\mathbf{S}} \quad \hat{\mathbf{E}} \quad \hat{\mathbf{Z}}]^T\end{aligned}\tag{6.108}$$

To propagate the uncertainty an appropriate reference system needs to be used. In this case we adopt the Earth-Centred-Inertial (ECI) frame. The tracking covariance matrix is expressed in the spherical coordinate frame of the radar. To transform in ECI coordinates, first a transformation from spherical to cartesian coordinates is required, then to the ECI frame. This

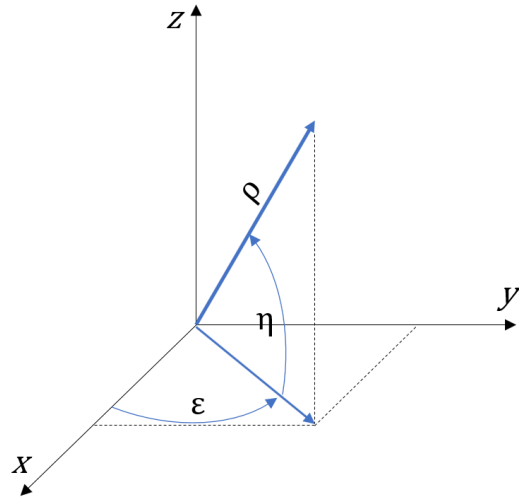


Figure 41. Frame for spherical coordinates

transformation is nonlinear. To linearize the process the Jacobian matrix (D) must be calculated to transform from spherical to cartesian coordinates, according to the frame in the figure.

$$D = \begin{bmatrix} -\cos \varepsilon_{TRK} \cos \eta_{TRK} & r_{TRK} \cos \varepsilon_{TRK} \sin \eta_{TRK} & r_{TRK} \sin \varepsilon_{TRK} \cos \eta_{TRK} \\ \cos \varepsilon_{TRK} \sin \eta_{TRK} & r_{TRK} \cos \varepsilon_{TRK} \cos \eta_{TRK} & -r_{TRK} \sin \varepsilon_{TRK} \sin \eta_{TRK} \\ \sin \eta_{TRK} & 0 & r_{TRK} \cos \varepsilon_{TRK} \end{bmatrix} \quad 6.111$$

Then, the transformation from the spherical coordinate system to the cartesian ECI frame is given by

$$Q_{TRK,ECI}^{RDR} = (M_{SEZ \rightarrow ECI} \cdot D) \cdot Q_{TRK,SPH}^{RDR} \cdot (M_{SEZ \rightarrow ECI} \cdot D)^T \quad 6.112$$

The covariance matrix has now non-null off-diagonal elements: a geometrical interpretation is that now the ellipsoid considers variances about the principal axes and the rotation.

$$Q_{TRK,ECI}^{RDR} = \begin{bmatrix} \sigma_{xTRK}^2 & \sigma_{xyTRK} & \sigma_{xzTRK} \\ & \sigma_{yTRK}^2 & \sigma_{yzTRK} \\ sym & & \sigma_{zTRK}^2 \end{bmatrix} \quad 6.113$$

To propagate the uncertainty from the time of tracking to the time of the foreseen collision we will use the Markley's method [48]. Two states are used, t_{k-1} and t_k , to calculate the state transition matrix. Earth's flattening effect is the most important in this process. In general, a deviation from a position is described by

$$\begin{Bmatrix} \delta \mathbf{r} \\ \delta \mathbf{v} \end{Bmatrix} = \mathbf{\Phi}(t, t_0) \begin{Bmatrix} \delta \mathbf{r}_0 \\ \delta \mathbf{v}_0 \end{Bmatrix} \quad 6.114$$

where $\mathbf{\Phi}$ is the state transition matrix given by

$$\mathbf{\Phi} = \begin{bmatrix} \mathbf{\Phi}_{11} & \mathbf{\Phi}_{12} \\ \mathbf{\Phi}_{21} & \mathbf{\Phi}_{22} \end{bmatrix} \quad 6.115$$

The differential equation is calculated by

$$\frac{\partial}{\partial t} \mathbf{\Phi}(t, t_0) = \mathbf{A}_1(t) \mathbf{\Phi}(t, t_0) = \begin{bmatrix} \mathbf{0} & \mathbf{I} \\ \mathbf{G}(t) & \mathbf{0} \end{bmatrix} \mathbf{\Phi}(t, t_0) \quad 6.116$$

where $\mathbf{\Phi}(t_0, t_0) = \mathbf{I}$ is the initial condition, $\mathbf{r} = \{x \ y \ z\}^T$ and $\mathbf{v} = \{\dot{x} \ \dot{y} \ \dot{z}\}^T$ are the cartesian states at time t , \mathbf{r}_0 and \mathbf{v}_0 are the states at the initial time, $\mathbf{0}$ is the 3x3 matrix of zeros, \mathbf{I} is the 3x3 identity matrix, $\mathbf{G}(t) = \partial \mathbf{a}(\mathbf{r}, t) / \partial \mathbf{r}$ is the gradient matrix and $\mathbf{a}(\mathbf{r}, t)$ the satellite accelerations. The simplified state transition matrix is

$$\mathbf{\Phi}(t, t_0) \approx \begin{bmatrix} \mathbf{\Phi}_{rr} & \mathbf{\Phi}_{rv} \\ \mathbf{\Phi}_{vr} & \mathbf{\Phi}_{vv} \end{bmatrix} \quad 6.117$$

with

$$\begin{aligned}
\Phi_{rr} &= I + (2\mathbf{G}_0 + \mathbf{G}) \frac{(\Delta t)^2}{6} \\
\Phi_{rv} &= I\Delta t + (\mathbf{G}_0 + \mathbf{G}) \frac{(\Delta t)^3}{12} \\
\Phi_{vr} &= (\mathbf{G}_0 + \mathbf{G}) \frac{\Delta t}{2} \\
\Phi_{vv} &= I + (\mathbf{G}_0 + 2\mathbf{G}) \frac{(\Delta t)^2}{6}
\end{aligned} \tag{6.118}$$

where $\Delta t = t - t_0$ and $\mathbf{G}_0 = \mathbf{G}(t_0)$. The \mathbf{G} gradient matrix considers only central and J_2 forces, and it is given by

$$\mathbf{G}(t) = \frac{\partial \mathbf{a}(\mathbf{r}, t)}{\partial \mathbf{r}} = \begin{bmatrix} \frac{\partial a_x}{\partial x} & \frac{\partial a_x}{\partial y} & \frac{\partial a_x}{\partial z} \\ \frac{\partial a_y}{\partial x} & \frac{\partial a_y}{\partial y} & \frac{\partial a_y}{\partial z} \\ \frac{\partial a_z}{\partial x} & \frac{\partial a_z}{\partial y} & \frac{\partial a_z}{\partial z} \end{bmatrix} \tag{6.119}$$

The accelerations considered are from central forces and J_2

$$\begin{aligned}
a_x &= -\frac{\mu x}{r^3} \left[1 + \frac{3J_2 R_e^2}{2r^2} \left(1 - \frac{5z^2}{r^2} \right) \right] \\
a_z &= -\frac{\mu z}{r^3} \left[1 + \frac{3J_2 R_e^2}{2r^2} \left(3 - \frac{5z^2}{r^2} \right) \right]
\end{aligned} \tag{6.120}$$

The partial derivatives are

$$\frac{\partial a_x}{\partial x} = \frac{\mu}{r^5} \left[3x^2 - r^2 - \frac{3}{2} J_2 R_e^2 + \frac{15}{2} \frac{J_2 R_e^2}{r^2} (x^2 + z^2) - \frac{105}{2} \frac{J_2 R_e^2}{r^4} x^2 z^2 \right] \tag{6.121}$$

$$\frac{\partial a_x}{\partial y} = \frac{3\mu xy}{r^5} \left[1 + \frac{5}{2} \frac{J_2 R_e^2}{r^2} - \frac{35}{2} \frac{J_2 R_e^2}{r^4} z^2 \right] \tag{6.122}$$

$$\frac{\partial a_x}{\partial z} = \frac{3\mu xy}{r^5} \left[1 + \frac{15}{2} \frac{J_2 R_e^2}{r^2} - \frac{35}{2} \frac{J_2 R_e^2}{r^4} z^2 \right] \tag{6.123}$$

$$\frac{\partial a_y}{\partial x} = \frac{\partial a_x}{\partial y} \quad 6.124$$

$$\frac{\partial a_y}{\partial y} = \frac{y}{x} \frac{\partial a_x}{\partial y} + \frac{a_x}{x} \quad 6.125$$

$$\frac{\partial a_y}{\partial z} = \frac{y}{x} \frac{\partial a_x}{\partial z} \quad 6.126$$

$$\frac{\partial a_z}{\partial x} = \frac{\partial a_x}{\partial z} \quad 6.127$$

$$\frac{\partial a_z}{\partial y} = \frac{\partial a_y}{\partial z} \quad 6.128$$

$$\frac{\partial a_z}{\partial z} = \frac{\mu}{r^5} \left[-r^2 + 3 \left(\frac{3}{2} J_2 R_e^2 + 15 \frac{J_2 R_e^2}{r^2} z^2 - \frac{35}{2} \frac{J_2 R_e^2}{r^4} z^4 \right) \right] \quad 6.129$$

Once covariance matrixes are computed, they are propagated up to the time of closest approach. Under the hypothesis that covariance matrixes are uncorrelated, it is possible to sum them in the same frame obtaining

$$C = C_p + C_s$$

The general method to compute the collision probability projects a 3-dimensional matrix PDF into a 2-dimensional matrix, under the assumptions before cited. The matrix is projected onto the encounter frame. Different authors define the encounter frame in various ways [49, 50]. We define the encounter frame at the time of closest approach as follow. We define the relative velocity \mathbf{v}_r and distance \mathbf{r}_r with respect to the debris

$$\mathbf{v}_r = \mathbf{v}_s - \mathbf{v}_d \quad 6.130$$

$$\mathbf{r}_r = \mathbf{r}_s - \mathbf{r}_d$$

Subscripts s and d refer to the satellite and debris respectively. The encounter frame is defined by the following unit vectors.

$$\hat{e}_x = \frac{\mathbf{v}_r}{|\mathbf{v}_r|} \quad \hat{e}_y = \frac{\mathbf{v}_s \times \mathbf{v}_d}{|\mathbf{v}_s \times \mathbf{v}_d|} \quad \hat{e}_z = \hat{e}_x \times \hat{e}_y \quad 6.131$$

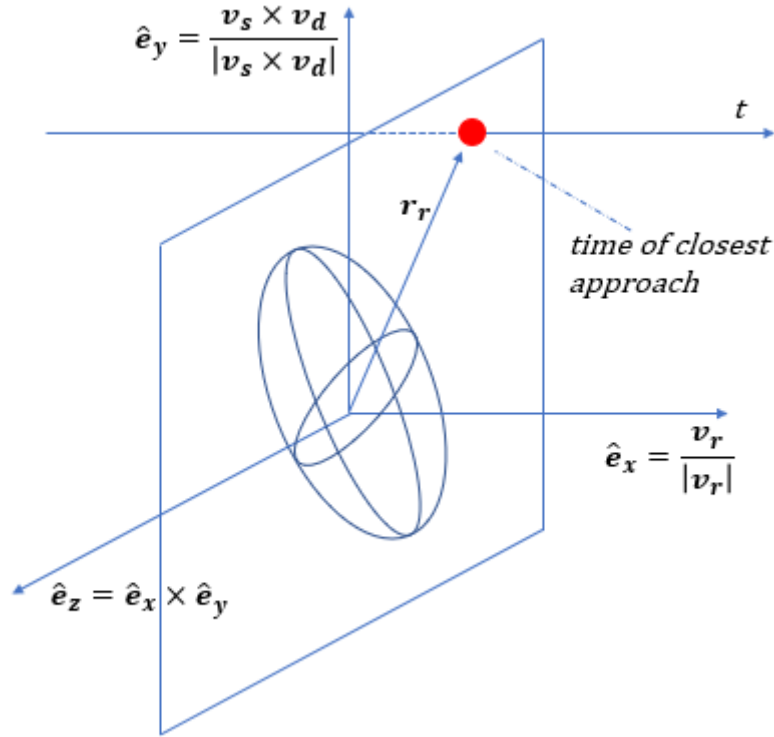


Figure 42. Encounter frame at the time of closest approach

The plane defined by versors \hat{e}_y and \hat{e}_z is the conjunction plane. The matrix to change the coordinates to the encounter frame is

$$M_{ECI \rightarrow ENC} = [\hat{e}_x \quad \hat{e}_y \quad \hat{e}_z]^T \quad 6.132$$

Thus, the cumulative covariance matrix is transferred into the encounter frame

$$C_{ENC} = M_{ECI \rightarrow ENC} C M_{ECI \rightarrow ENC}^T \quad 6.133$$

The probability of collision will be computed along the vector \mathbf{r}_r .

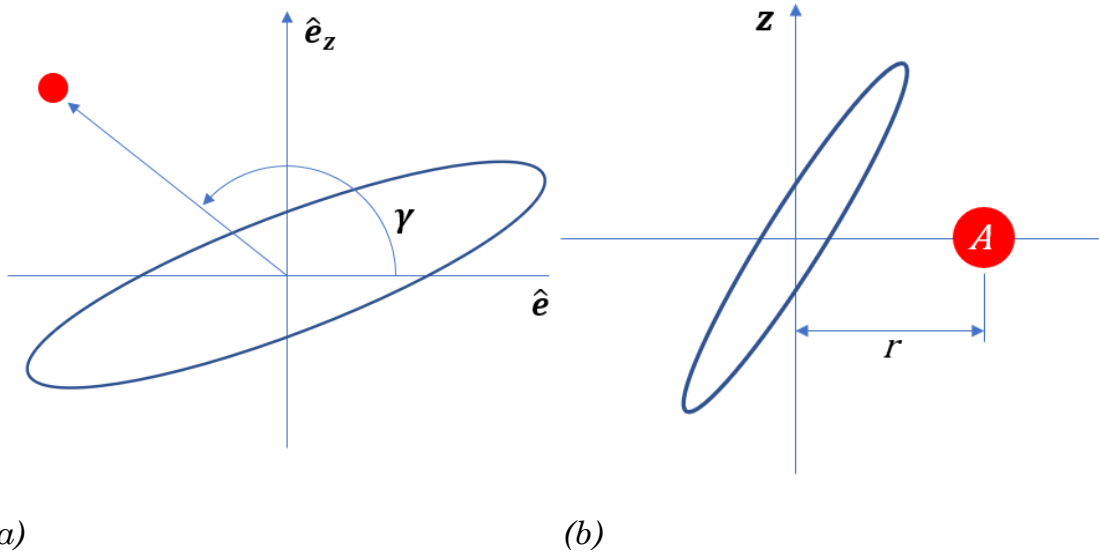


Figure 43. Encounter plane rotation (a) and Frame for the probability of collision calculation (b)

The conjunction plane is the y - z plane. Rotating the cumulative covariance matrix into the encounter frame, is it possible to express the bivariate Gaussian pdf as

$$f(y, z) = \frac{1}{2\pi\sigma_y\sigma_z\sqrt{1-\rho_{yz}^2}} e^{-\frac{\left(\frac{y}{\sigma_y}\right)^2 - 2\rho_{yz}\left(\frac{y}{\sigma_y}\right)\left(\frac{z}{\sigma_z}\right) + \left(\frac{z}{\sigma_z}\right)^2}{2(1-\rho_{yz}^2)}} \quad 6.134$$

The probability of collision is

$$P = \int_A f(y, z) dA \quad 6.135$$

For simplicity, a rotation is made to define the y -axis along the \mathbf{r}_{ds} vector. The area A is a circle of radius $r_A = r_s + r_d$, primary plus secondary body, called hard body radius. Since the satellite attitude is unknown, we represent the satellite as a sphere having the diameter of its maximum length. If the debris has not a spherical size, as it is in a real case, the same considerations can be done.

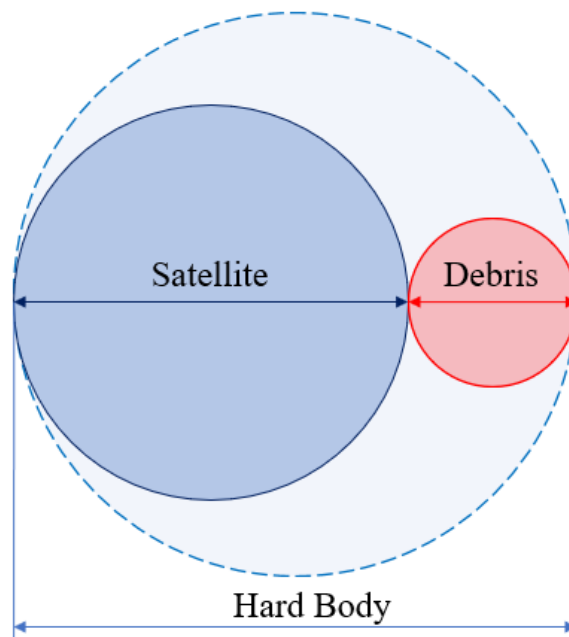


Figure 44. Hard Body definition

The circle of integration is positioned in $(y_e, 0)$ where y_e is the distance from the origin, and thus from the nominal position of the satellite.

7

Optimisation results

In this section results for trajectory and attitude optimisation are presented. In the last part of this chapter results for collision avoidance will be discussed. Simulations have been run with a processor Intel(R) Core(TM) i7-3537U, RAM 10 GB. For these analyses 20 particles have been used and both for trajectory and attitude optimisation the following data in the table have been used.

Orbital data	
a	600 km
e	0
i	97.4°
ω	0°
Ω	0°

Table 12. Simulation orbital data

7.1 Probability of collision analysis

The aim of this study is to map the probability of collision between the spacecraft and a debris when these two are driven away each other. The purpose is to find the minimum distance to have an acceptable probability of collision and then implementing a proper manoeuvre. For the spacecraft, initial data for simulation are resumed below.

Spacecraft initial position				
a	e	i	ω	Ω
6978 km	0	97.4°	0°	0°
Navigation error				
Radial (R) σ_R				13.81 m
In-Track (S) σ_S				4.15 m
Cross-Track (W) σ_W				3 m

Table 13. Spacecraft initial data and navigation error

Radar data through which initial covariance matrix for debris is calculated are show in the following table.

Radar Tracking Angle (SEZ)	
$\epsilon = -45 \text{ deg}$	$\eta = 81 \text{ deg}$
Ground-Based Radar Fixed Parameters	
Frequency	442 MHz
Peak transmit power	32 MW
Beamwidth	1.3°
Aperture dimension	58 m
Noise figure	4.5 dB
Radar pulse duration	1 μs
Transmit antenna gain	48 dBi
Radar system losses	15 dB

Table 14. Radar data

At the time of closest approach, under the hypothesis that these matrixes are uncorrelated, it is possible to sum them obtaining the cumulative covariance matrix (Figure 45).

The encounter frame is defined by the axes

$$\{X \ Y \ Z\} = \begin{pmatrix} 0 & -1 & 0 \\ -0.847 & 0 & -0.531 \\ 0.531 & 0 & -0.847 \end{pmatrix}$$

The conjunction plane is the YZ plane. The Hard Body has got a radius of 85 centimetres, considering debris of 10 centimetres radius.

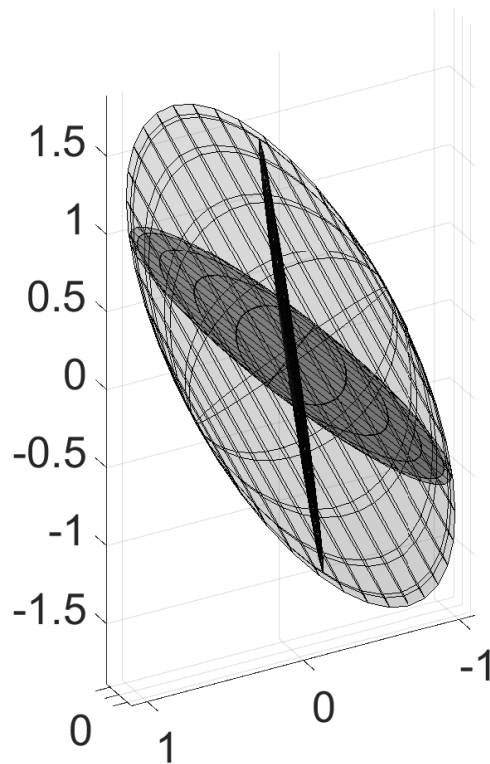


Figure 45. Covariance matrixes. The outer ellipsoid is the cumulative covariance matrix. Scale graph

Assuming that the covariance matrixes are uncorrelated it is possible to sum them. What is obtained is an ellipsoid sum of the two covariance matrixes showed in the previous graph. An acceptable risk of collision [51] can be assumed when the probability of collision is 10^{-5} . In this case, a manoeuvre is

needed to avoid a collision. The satellite could be moved in a higher orbit, raising it at least of 1.68 km about.

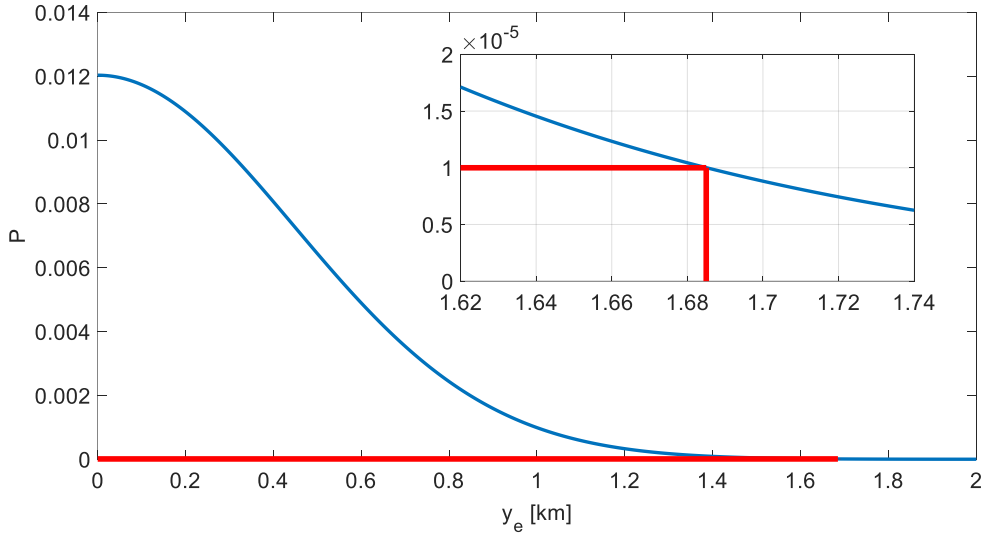


Figure 46. Probability of collision in the conjunction plane

To avoid the tracked debris it is necessary a manoeuvre to outstrip the two orbits. In a more realistic scenario, satellite and debris orbit do not intersect each other but will be situated at a certain distance, thus the manoeuvre will increase their distance of

$$\Delta r = y^* - y_e$$

where y^* is the distance having an acceptable probability, y_e the initial distance.

7.2 Trajectory optimisation

The trajectory is optimised considering a Hall-thrust effect propulsor, orbital perturbation disregarding atmospheric drag which is neglectable at 600 km of altitude. Data used for this optimisation are summarised below.

	Initial state	Case 1	Case 2
a	600 km	601.68 km	610 km
e	0	0	0
i	97.4°	97.4°	97.4°
ω	0°	0°	0°
Ω	0°	0°	0°

Table 15. Trajectory optimisation simulation data

The electric propulsor can provide 13 mN thrust with 1390 s of specific impulse.

7.2.1 Case 1 analysis

In this case a low-thrust manoeuvre is optimised to raise the orbit. The purpose is to maintain a quasi-circular orbit, increasing the altitude of 1 km. Optimisation results show that the duration of this manoeuvre is 45.92 min, requiring a computational time of 72.75 s to calculate the optimal solution. Optimised coefficients are shown in the table below. From eq. (6.45, 6.46), thrust is expressed in spherical coordinates in RSW frame through azimuth and elevation angles, α and β , as

$$\alpha = a_0 + \sum_{i=1}^6 a_i \left(\frac{t}{t_f}\right)^i \quad \beta = b_0 + \sum_{i=1}^6 b_i \left(\frac{t}{t_f}\right)^i$$

Components in RSW frame are in the vector

$$\begin{bmatrix} \mathbf{u}_R \\ \mathbf{u}_S \\ \mathbf{u}_W \end{bmatrix} = \begin{bmatrix} \sin \alpha \cos \beta \\ \cos \alpha \cos \beta \\ \sin \beta \end{bmatrix}$$

Polynomial coefficients deriving from the optimisation are listed below.

a		b	
a₀	0.3756	b₀	-0.8205
a₁	0.9976	b₁	-0.6503
a₂	0.9951	b₂	-0.5606
a₃	0.9969	b₃	-1.0000
a₄	-0.9969	b₄	-0.9917
a₅	-0.7569	b₅	-0.9999
a₆	-0.7845	b₆	-0.1777

Table 16. Case 1. Polynomial coefficients for the control law

The control time history is shown in the following graph.

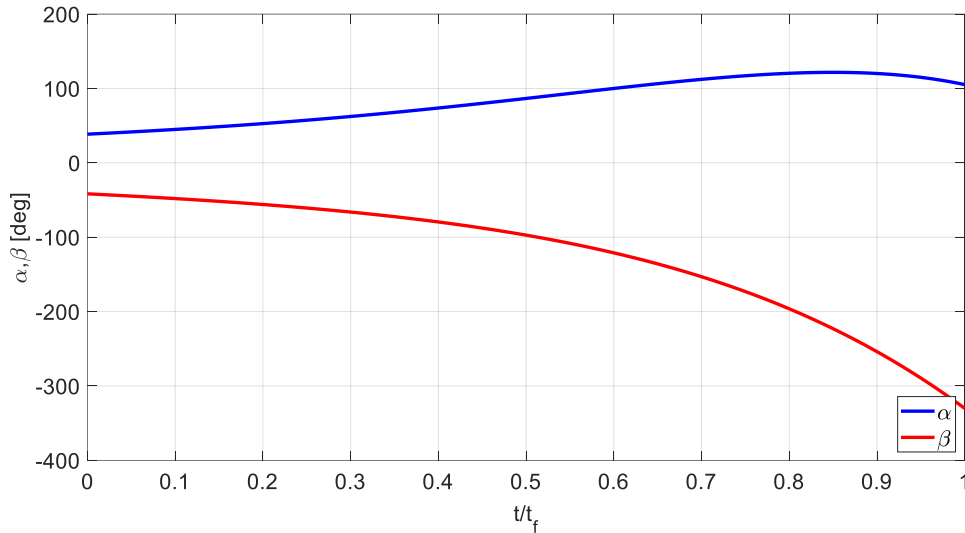


Figure 47. Control time history for case 1

In a real scale it would be impossible to visualise the transfer orbit: it is necessary to scale the graph to visualise this feasible solution. The transfer orbit can be visualized plotting the orbit radius during the manoeuvre.

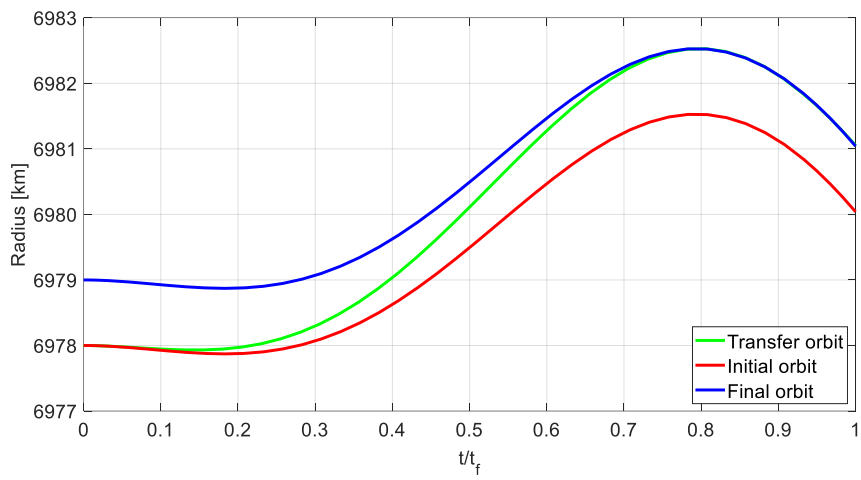


Figure 48. Transfer orbit radius during the manoeuvre for final case

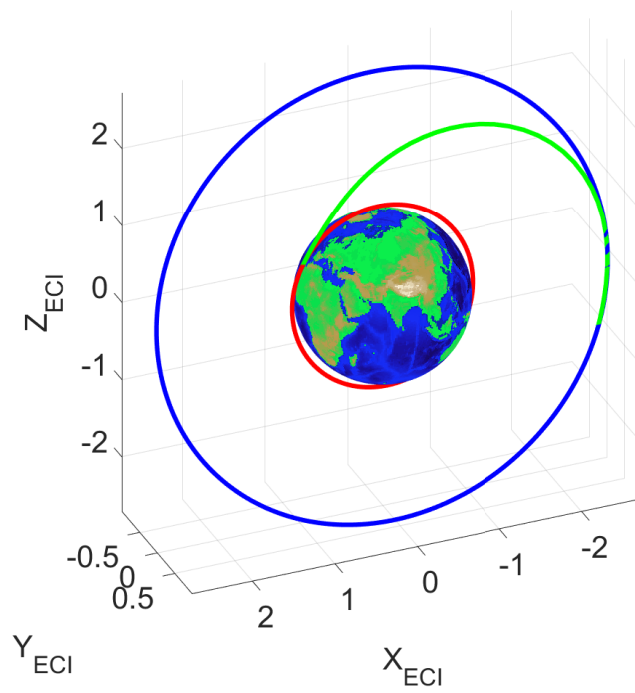


Figure 49. Case 1 transfer orbit (scale graph)

7.2.2 Case 2 analysis

In this second case, as the previous one, a low-thrust manoeuvre is considered. The altitude is now raised of 60 km and the inclination is changed of 5 deg to show the capability to change the inclination. The duration of this second manoeuvre is 124.94 min (2.08 h), requiring a computational time of 36.68 s to calculate the optimal solution. Polynomial coefficients are shown in the following table.

a		b	
a₀	0.1362	b₀	0.2584
a₁	-0.8317	b₁	-0.6276
a₂	0.9733	b₂	0.4673
a₃	0.0525	b₃	-1.000
a₄	1.000	b₄	-0.3082
a₅	-0.7559	b₅	-0.6576
a₆	0.9706	b₆	-0.9765

Table 17. Case 2. Polynomial coefficients for the control law

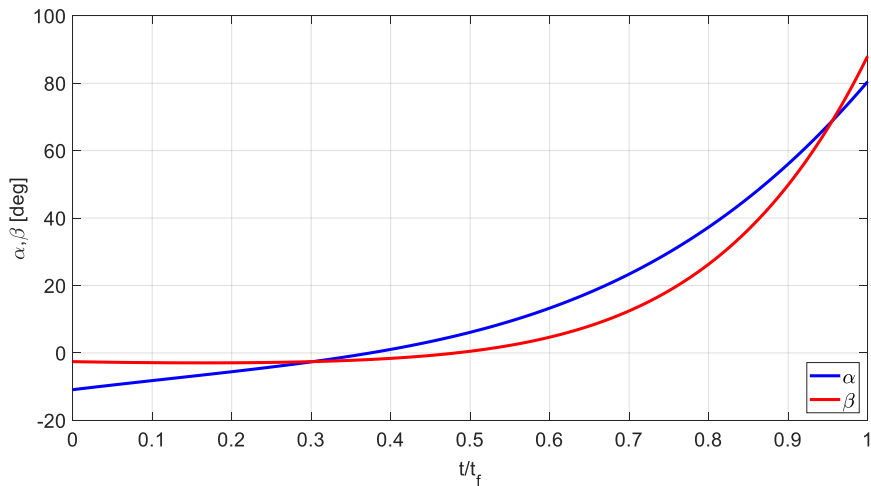


Figure 50. Control time history for case 2

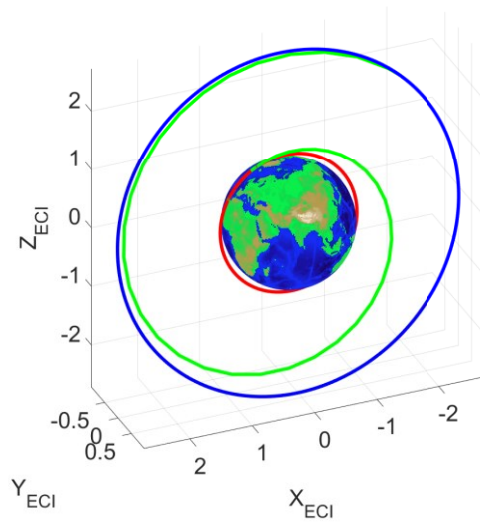


Figure 51. Case 2 transfer orbit (scale graph)

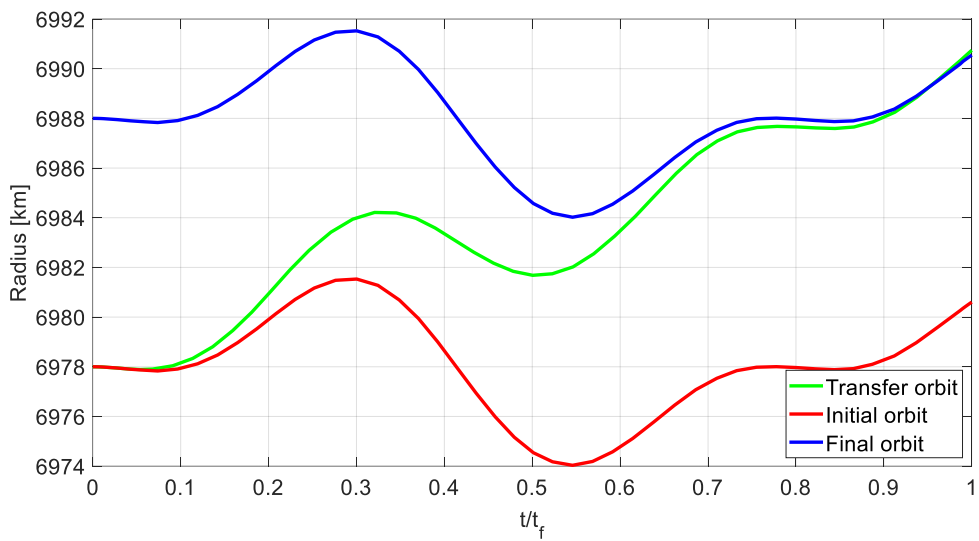


Figure 52. Transfer orbit radius during the manoeuvre for case 2

As a result, the control time history in the previous figure is generated. Similarly done case 1, the transfer orbit is shown in the previous graphs.

7.3 Attitude reorientation optimisation

Since the position of the Sun is an important factor in reorientation because it is mandatory avoiding pointing toward it with the IR-camera, a precise day must be considered. This analysis is conducted at Julian day 58889.5. We consider the same orbit and orbital parameters used in the trajectory optimisation before, employing the RSW frame for calculation and optimisation. The initial attitude is defined by the unit quaternion $q_0 = [1 \ 0 \ 0 \ 0]$ and the final attitude is the quaternion

$$q_f = [0.5592 \ 0 \ -0.5699 \ -0.6021]$$

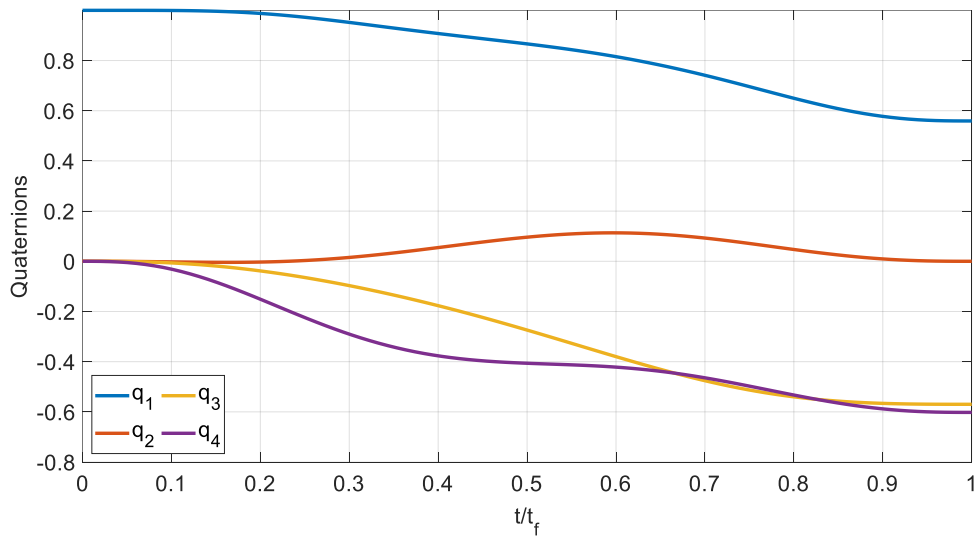


Figure 53. Quaternion time history

Reaction wheels mounted on-board can provide a maximum torque of 7 mNm, a parameter used in the cost function to limit the torque along the three axes. The time needed to accomplish the reorientation manoeuvre is 15.52 min, while its time of calculation is 82.38 s.

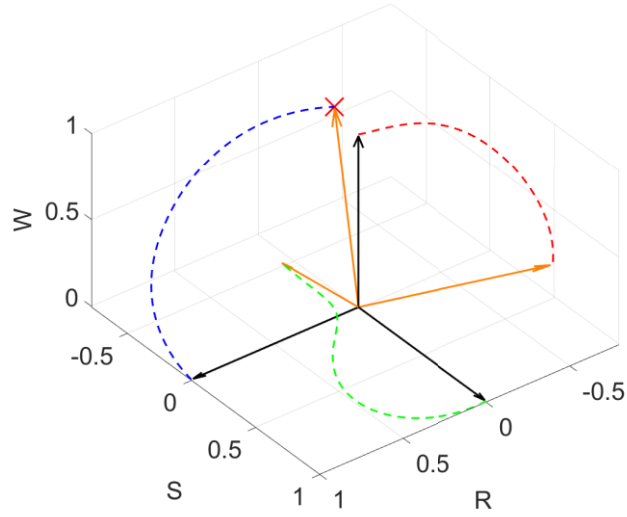


Figure 54. Manoeuvre in RSW

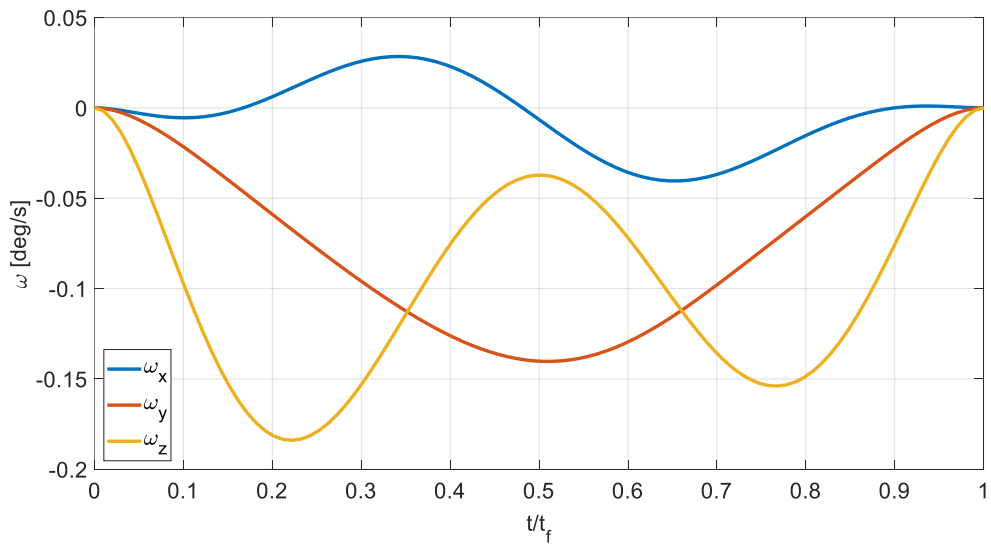


Figure 55. Angular velocity time history

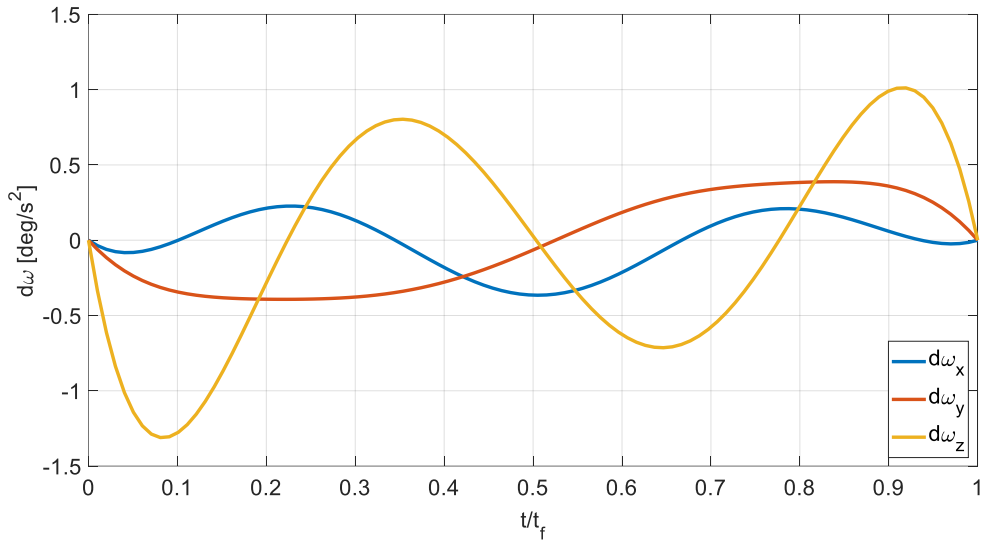


Figure 56. Angular accelerations time histories

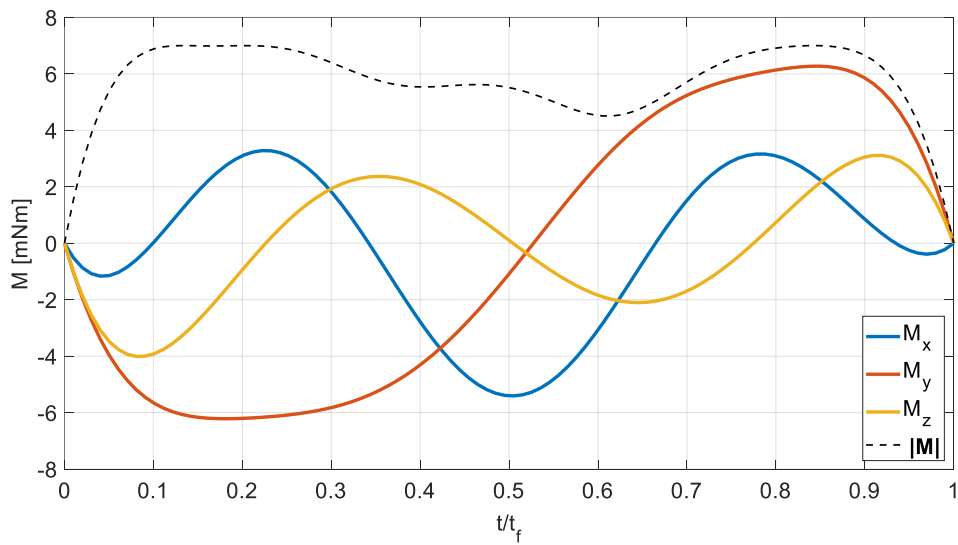


Figure 57. Torque time history

As previously described in section 6.2.7, the cost function for attitude reorientation manoeuvre is delineated as (eq. 6.98)

$$J = c_t t_f + \sum_{i=1}^{N_{ineq}} G_i$$

Where in G_i the inequality to define the keep-out cones is enclosed. We defined the function F in eq. 6.99. If $F(t) < 0$ the boresight vector is outside the keep-out cone and the constraint is satisfied. There exist two $F(t)$ functions, defined for the Sun and Earth. Specifically, they are defined as

$$F_{\odot}(t) = \mathbf{q}(t)^T M_F(t) \mathbf{q}(t) \qquad F_{\oplus}(t) = \mathbf{q}(t)^T M_F \mathbf{q}(t)$$

Because of the orbital movement of the satellite, the Sun vector in RSW is no longer the same, generating a time-variant matrix $M_F(t)$. Instead, since the direction of the Earth keep-out cone is the vector $-\hat{\mathbf{r}}$ in RSW frame, it is constant along the orbit. The results for these F functions are shown in the following graph.

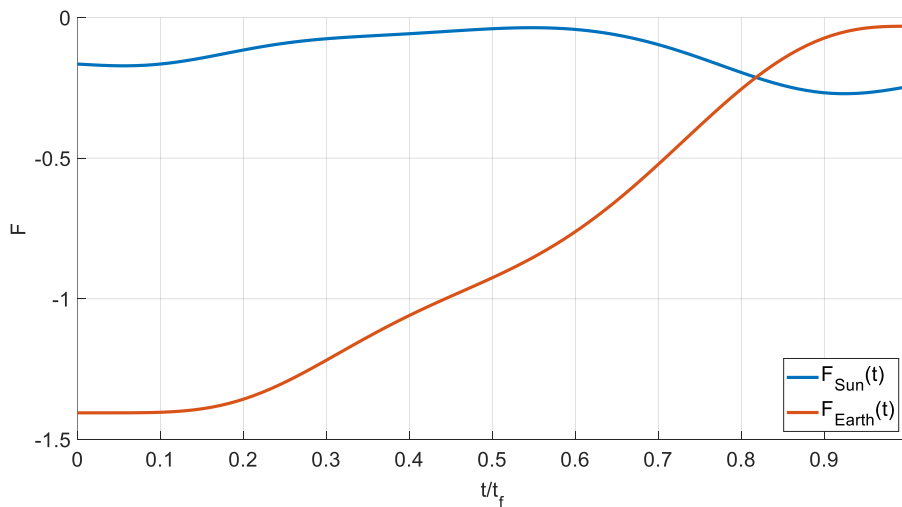


Figure 58. Keep-out functions

Their value is always negative showing that the constraint is satisfied.

8

Conclusion

The purpose of this thesis is to suggest a feasible autonomous algorithm for a SmartSat, in view of next developments for autonomous satellites. The satellite concept has been presented, with its initial aim. This optimisation method could generally be used for any LEO small satellite. The possibility to design constrained manoeuvre using Particle Swarm Optimisation technique was demonstrated. Guidance and attitude were studied separately, using a polynomial parametrisation for control laws. The proposed methods for optimisation satisfy the boundary conditions and constraints. Low calculation times are the outcome for trajectory optimisation, allowing the implementation of real-time onboard applications. Attitude reorientation manoeuvres fully satisfied all constraints with low computation time. Collision avoidance analysis has delineated the minimum distance needed to avoid the impact, under the condition of acceptable uncertainty at sensor level to guarantee the initial gaussianity. However, metaheuristic methods could provide suboptimal solutions and because their probabilistic nature could produce a different solution in different runs. Optimality of the control law depends on the kind shape function used in the parametrization: it is necessary choosing appropriate shape functions for the desired optimisation. Weigh coefficients play an important role in the cost function: they are needed to be accurately chosen to achieve a correct result.

The existence of different optimisation techniques allows implementing several algorithms aimed to have an intelligent satellite, in which onboard calculations are possible. However, not every optimisation technique could be promptly accepted. The first criterion of evaluation is the computational time as discussed pseudo-spectral methods seem not to be the right candidate to implement a real-time optimisation. Because of its a priori not predictable time needed to implement the feasible solution and moreover the possibility not to express an initial guess, it does not show as a possible choice to implement this kind of task. Particle Swarm Optimisation instead claims the capability to globally search the feasible solution in the solution space needing not any initial condition. Furthermore, its algorithm is transparent, simple to implement, with few algorithmic parameters compared to other evolutionary algorithms. Notwithstanding it has some difficulties to implement equality constraints. In this work, they have been included in the cost function through a penalty method, scaled by a user-defined coefficient. These weighting factors are the main concern applying PSO, raising the new problem not to have a badly conditioned algorithm [52]. Though this study cost function coefficients have been experimented until acceptable results and good levels of convergence. The methodology used in this investigation can be summarised as follows:

1. Definition of the system equations of motion
2. Definition of the path and constraints to obtain a feasible solution, definition of the cost function and penalty functions
3. Scaling of constraints expressed in the cost function in order not to create a huge disparity amongst them
4. Solution checking. If the optimiser prematurely converges, constraint coefficients may be changed

The proposed methodology offers the possibility to use a polynomial parametrisation for continuous control: this is successful if used for small problems while it could bring more issues for complex problems, due to the number of parameters. PSO requires a good level of intuition to weigh cost function constraint coefficients. This is nowadays an unsolved problem but based on the user's experience.

On these conclusions future researches could focus on:

- Exploring changing polynomial degree and number of polynomials to characterise the control function. Investigate their computational time and the possibility of a real-time implementation
- Finding a technique to weigh coefficient in every scenario
- Integrate the algorithm for the optimal manoeuvre in a control algorithm, capable to maintain the pointing with the required accuracy
- How thrust influences the calculated probability of collision.
- A better parametrization of control law for trajectory optimisation to reduce the cost function, considering the initial and final attitude
- Integration of the optimisation algorithm and fine pointing control system to maintain the pointing on the observed area and the implementation of an optimised observation plan
- On-board debris detection to autonomously detect space objects and implement collision avoidance manoeuvres reducing communications with the ground station

This list is not exhaustive but is a first direction for future investigation.

References

- [1] R. R. Bate, D. D. Muller, and J. E. White, *Fundamentals of astrodynamics*. 1971.
- [2] "History of modern astronomy."
http://spider.seds.org/spider/ScholarX/hist_mod.html (accessed.
- [3] "A brief story of space exploration." <https://aerospace.org/article/brief-history-space-exploration> (accessed.
- [4] E. Chaisson and S. McMillan, *Astronomy Today*, 7th Edition ed. 2011.
- [5] NASA. "Gamma rays."
<https://web.archive.org/web/20080229022427/http://science.hq.nasa.gov/kids/imagers/ems/gamma.html> (accessed.
- [6] P. Y. Bély and B. S. May, "The pointing stability of the Hubble Space Telescope and proposed concepts for the pointing control of the next generation space telescope," 1992.
- [7] "Hubble Space Telescope." <https://hubblesite.org> (accessed.
- [8] R. Wittlesley, "The hubble Space Telescope Fine Guidance System operating in the Coarse Track Pointing Control Mode."
- [9] G. S. Nurre, S. J. Anhouse, and S. N. Gullapalli, *Hubble Space Telescope Fine Guidance Sensor Control System* (SPIE 1989 Technical Symposium on Aerospace Sensing). SPIE, 1989.
- [10] M. J. Rieke, D. M. Kelly, and S. D. Horner, *Overview of James Webb Space Telescope and NIRCams Role* (Optics and Photonics 2005). SPIE, 2005.
- [11] NASA. "James Webb Space Telescope."
<https://jwst.nasa.gov/content/science/index.html> (accessed.
- [12] R. Sterritt and M. Hinchey, *Engineering ultimate self-protection in autonomous agents for space exploration missions*. 2005, pp. 506-511.
- [13] E. Vassev and M. Hinchey, *Autonomy requirements engineering for space missions*. Springer, 2014.
- [14] F. Lorenzo, "Artificial Intelligence for Small Satellites Mission Autonomy," PhD, Politecnico di Torino, Politecnico di Torino, 2017.
- [15] R. L. White, M. B. Adams, E. G. Geisler, and F. D. Grant, "Attitude and Orbit Estimation Using Stars and Landmarks," *IEEE Transactions on Aerospace and Electronic Systems*, vol. AES-11, no. 2, pp. 195-203, 1975, doi: 10.1109/TAES.1975.308058.
- [16] M. Straub and J. Christian, *Autonomous Optical Navigation for Earth-Observing Satellites using Coastline Matching*. 2015.

- [17] S. S. Board and E. and National Academies of Sciences, and Medicine, "Achieving Science with CubeSats: Thinking Inside the Box," *National Academies Press*, 2016.
- [18] D. Girimonte and D. Izzo, "Artificial Intelligence for Space Applications," in *Intelligent Computing Everywhere*, A. J. Schuster Ed. London: Springer London, 2007, pp. 235-253.
- [19] S. L. e. al., *Essentials of Metaheuristics*, Second ed. 2015.
- [20] J. Figueira, S. Greco, and M. Ehrgott, *Multiple Criteria Decision Analysis: state of the art surveys*. Springer, 2005.
- [21] P. S. Oliveto, J. He, and X. Yao, "Time Complexity of Evolutionary Algorithms for Combinatorial Optimization: A Decade of Results," *Int. J. Autom. Comput.*, vol. 4, no. 3, pp. 281–293, 2007.
- [22] R. Sandau, "Status and trends of small satellite missions for Earth observation," *Acta Astronautica*, vol. 66, no. 1, pp. 1-12, 2010/01/01/ 2010, doi: <https://doi.org/10.1016/j.actaastro.2009.06.008>.
- [23] NASA. (2014) Small Spacecraft Technology State of the Art. 1-197.
- [24] J. R. Wertz, D. F. Everett, and J. J. Puschell, *Space mission engineering : the new SMAD*. Hawthorne, CA: Microcosm Press : Sold and distributed worldwide by Microcosm Astronautics Books (in English), 2011.
- [25] A. Poghosyan and A. Golkar, "CubeSat evolution: Analyzing CubeSat capabilities for conducting science missions," *Progress in Aerospace Sciences*, vol. 88, pp. 59-83, 2017/01/01/ 2017, doi: <https://doi.org/10.1016/j.paerosci.2016.11.002>.
- [26] A. Freimann, A. Kleinschrodt, M. Schmidt, and K. Schilling, "Advanced Autonomy for Low Cost Ground Stations," *IFAC Proceedings Volumes*, vol. 46, no. 19, pp. 388-392, 2013/01/01/ 2013, doi: <https://doi.org/10.3182/20130902-5-DE-2040.00054>.
- [27] A. V. Rao *et al.*, "Algorithm 902: GPOPS, A MATLAB software for solving multiple-phase optimal control problems using the gauss pseudospectral method," *ACM Trans. Math. Softw.*, vol. 37, no. 2, pp. 1-39, 2010, doi: 10.1145/1731022.1731032.
- [28] J. T. Betts, *Practical methods for optimal control and estimation using nonlinear programming, 2nd ed*, 2nd ed ed. S.l.]: S.l. : Society for Industrial and Applied Mathematics, 2010.
- [29] K. Chircop, A. Gardi, D. Zammit-Mangion, and R. Sabatini, "A New Computational Technique for the Generation of Optimised Aircraft Trajectories," *Nonlinear Engineering*, vol. 6, 04/01 2017, doi: 10.1515/nleng-2016-0049.
- [30] M. A. Patterson and A. V. Rao, *GPOPS-II: A MATLAB Software for Solving Multiple-Phase Optimal Control Problems Using hp-Adaptive*

- Gaussian Quadrature Collocation Methods and Sparse Nonlinear Programming* (no. 1). Association for Computing Machinery, 2014, p. Article 1.
- [31] A. Salupere, "The Pseudospectral Method and Discrete Spectral Analysis," Springer Berlin Heidelberg, 2009, pp. 301-333.
- [32] K. F. Graham and A. V. Rao, "Minimum-Time Trajectory Optimization of Multiple Revolution Low-Thrust Earth-Orbit Transfers," *Journal of Spacecraft and Rockets*, vol. 52, no. 3, pp. 711-727, 2015, doi: 10.2514/1.A33187.
- [33] K. Graham and A. Rao, "Minimum-Time Trajectory Optimization of Low-Thrust Earth-Orbit Transfers with Eclipsing," *Journal of Spacecraft and Rockets*, vol. 53, pp. 1-15, 02/22 2016, doi: 10.2514/1.A33416.
- [34] G. A. Boyarko, M. Romano, and O. A. Yakimenko, "Time-optimal reorientation of a spacecraft using a direct optimization method based on inverse dynamics," *2010 IEEE Aerospace Conference*, pp. 1-13.
- [35] J. Yang and E. Stoll, *Time-optimal Spacecraft Reorientation with Attitude Constraints Based on A Two-stage Strategy*. 2018.
- [36] J. Alfredo G. Zurita, "Minimum-fuel trajectory design in multiple dynamical environments utilizing direct transcription methods and particle swarm optimization," *Astronautical Engineering*, Air Force Institute of Technology, 2016.
- [37] J. Kennedy and R. Eberhart, "Particle swarm optimization," in *Proceedings of ICNN'95 - International Conference on Neural Networks*, 27 Nov.-1 Dec. 1995 1995, vol. 4, pp. 1942-1948 vol.4, doi: 10.1109/ICNN.1995.488968.
- [38] G. Hintz, "Survey of Orbit Element Sets," *Journal of Guidance Control and Dynamics - J GUID CONTROL DYNAM*, vol. 31, pp. 785-790, 05/01 2008, doi: 10.2514/1.32237.
- [39] J. A. Kéchichian, *Applied Nonsingular Astrodynamics*. 2018.
- [40] D. Spiller, F. Curti, and L. Ansalone, *Inverse dynamics particle swarm optimization for spacecraft minimum-time maneuvers with constraints*. 2015.
- [41] M. D. Shuster, "A survey of attitude representation," presented at the Conference proceedings, 1993.
- [42] A. Bani Younes, J. Turner, D. Mortari, and J. Junkins, *A Survey of Attitude Error Representations*. 2012.
- [43] U.S. Naval Observatory and H. M. N. A. Office, *Astronomical phenomena for the year 2019*. Washington: U.S. Government Publishing Office, 2016.

- [44] R. A. Braeunig. "Atmospheric models." <http://www.braeunig.us/space/atmmodel.htm> (accessed.
- [45] "Distribution of space debris around Earth." ESA. https://www.esa.int/Safety_Security/Space_Debris (accessed.
- [46] K. T. Alfriend and I. Park, "When does the uncertainty becomes non-gaussian?," presented at the Advanced Maui Optical and Space Surveillance Technologies Conference (AMOS), 2016.
- [47] S. Hilton, F. Cairola, A. Gardi, R. Sabatini, N. Pongsakornsathien, and N. Ezer, "Uncertainty Quantification for Space Situational Awareness and Traffic Management," *Sensors*, vol. 19, p. 4361, 10/09 2019, doi: 10.3390/s19204361.
- [48] A. P. Chiaradia, H. Kuga, and A. Prado, "Comparison between Two Methods to Calculate the Transition Matrix of Orbit Motion," *Mathematical Problems in Engineering*, vol. 2012, 01/01 2012, doi: 10.1155/2012/768973.
- [49] F. K. Chan, *Probability of collision*. Aerospace Press, 2008, p. 365.
- [50] M. R. Akella and K. T. Alfriend, "Probability of Collision Between Space Objects," *Journal of Guidance, Control, and Dynamics*, vol. 23, no. 5, pp. 769-772, 2000, doi: 10.2514/2.4611.
- [51] H. Klinkrad, J. R. Alarcon, and N. Sanchez, "Collision Avoidance for Operational ESA Satellites," in *4th European Conference on Space Debris*, August 01, 2005 2005, vol. 587, p. 509. [Online]. Available: <https://ui.adsabs.harvard.edu/abs/2005ESASP.587..509K>. [Online]. Available: <https://ui.adsabs.harvard.edu/abs/2005ESASP.587..509K>
- [52] B. Conway, B. A. Conway, Ed. *Spacecraft Trajectory Optimization* (Cambridge Aerospace Series). Cambridge: Cambridge University Press, 2010.